PREDICTION OF WAVE PROPAGATION IN SOILS USING SEMI-ANALYTIC METHOD

Master Thesis

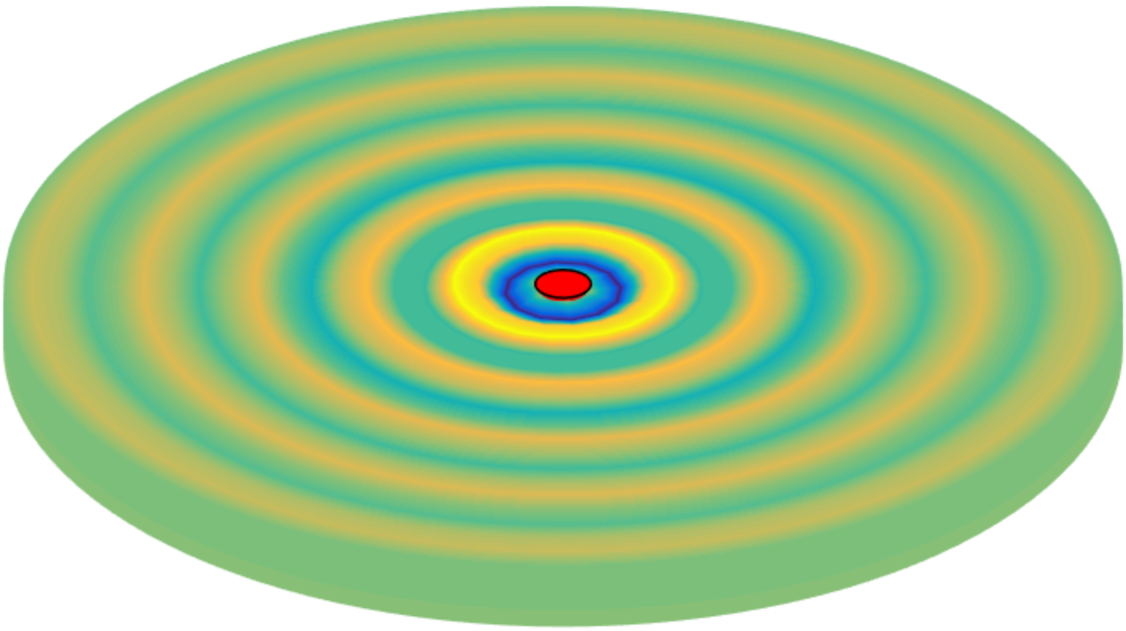

Structural and Civil Engineering *Aalborg University*

10^{th} *semester*

AALBORG UNIVERSITY
STUDENT REPORT

School of Engineering and Science
Study Board of Civil Engineering
Thomas Mans vej, 9220 Aalborg Ø
http://www.ses.aau.dk

Title:

Prediction of wave propagation in soils using semi-analytic method

Theme:

Master's Thesis

Project period:

February 23rd 2017 - Jun 16th 2017

Participants:

Forid Gobuzi
Lander Iglesias Bengoa
Erik Vaňo

Supervisor:

Lars Vabbersgaard Andersen

Co-supervisor:

Paulius Bucinskas

Total pages: 125
Report pages: 98
Appendix pages: 16
Completed 16-06-2017

Synopsis:

Ground-borne noise induced by trains and construction works has become day by day a constant issue to the tranquility of urban areas. Population increase and city developments mean that more areas will be subjected to uncomfortable noises and the need for tranquility is ever more necessary. So far these induced vibrations have been hard and expensive to predict, thus less time consuming and more accurate computational models are required. This is also the focus of this master's thesis where a semi-analytical model developed by several researchers will be evaluated. The semi-analytic model is used to predict the propagation of waves in a media due to vibrations from external source and the impact they have on the surrounding area. A thorough investigation of the model is performed by taking into account the influence of the soil properties in the dynamic amplification.
This master's thesis also includes an experimental part, where geophones are used to measure the vibrations from trains at a location specified by COWI. The data obtained from the measurements is used to find the properties of the soil and further validate the semi-analytic method.
To conclude, a comparison between the measured vibrations and the ones simulated from the model are analysed and compared in order to obtain a closer fit as possible.

Preface

This document icludes the master's thesis composed by a group of 10^{th} semester students at Aalborg University as part of the master programme in Structural and Civil engineering. The theme of the project is *Prediction of wave propagation in soils using semi-analytic method*.

Prerequisites for reading the report is basic knowledge regarding the scientific method, soil mechanics, wave dynamics and statistics.

The project group would like to show gratitude to the supervisor of the project, associate professor Lars Vabbersgaard Andersen and co-supervisor Paulius Bucinskas.

The cover photo shows an illustration of the semi-analytic model used in the thesis for prediction and assessment of the wave propagation in soil media.

Reading guide

Through the report, source references in the form of the Harvard method are applied. These are all listed in the back of the report. References are made for sources with either "[Surname/organisation, Year]" or "Surname/organisation [Year]" and, when relevant, specific pages, tables or figures may be stated. Websites are specified by author, title, URL and date. Books are specified by author, title, publisher and edition, where available. Papers are furthermore specified with journal, conference papers with time and venue, when available.

The project is provided with the digital file, Enclosure, where all codes, data files and videos used in the project are located.

Figures and tables in the report are numbered according to the respective chapter. In this way the first figure in chapter 3 has number 3.1, the second number 3.2 and so on. Explanatory text is found near the given figures and tables.

Forid Gobuzi	Lander Iglesias Bengoa	Erik Vaňo

Abstracto

El presente documento muestra el trabajo fin de master realizado durante el cuarto semestre de master en ingeniería civil en la universidad de Aalborg en colabración con la empresa constructora COWI. Este projecto trata con la predicción de propagación de ondas a través del metodo semianalytico desarrollado en la misma universidad.

Hoy en dia las vibraciones en medios urbanos dabidas a fuentes externas como autobuses, trenes o metros asi como obras se ha empezado a convertir en un problema para la salud de los ciudadanos. Las vibraciones producidas por estas fuentes pueden causar malestar y estrés. Por esta razón el control y medida continua de vibraciones asi como la distacia de edificios residenciales es un tema que en la actulidad va tomando más peso.

El objetivo principal de este projecto es el de analizar y provar el programa computacional para simulación de ondas en un medio. Gracias a este programa se pueden simular ondas y modelar suelos de diferentes características. Este programa, por tanto, puede permitir la simulación de ondas y vibración de tal forma que se puede medir su impaccto en el espacio. Este modelo esta basado en las teorias elastodinamicas de propagación de ondas.

El programa es testado en base a los conceptos teoricos de propagacion de ondas en suelos y adicionalmente, se han ejecutado varios test in situ para medición de ondas probocadas por trenes. El mismo suelo donde se midió ha sido simulado y las respuesta del modelo y medidas comparadas.

Table of contents

1 | Introduction

Cities development in the last decades has carried construction of new undergrounds, railways, roads and a lot of associated construction works to urban areas. All this, along with vehicle traffic has made the urban tranquility an important issue to the authorities since all the vibrations generated in this activities lead to considerable noise pollution that can cause stress and unwellness for people.

For this reason, the prediction of wave propagation in soils has become an important issue in nowadays engineering problems. Moreover new regulations regarding human comfort and environmental impact are implemented by the authorities. Therefore, there is a necessity of understanding and controlling these man-made vibrations.

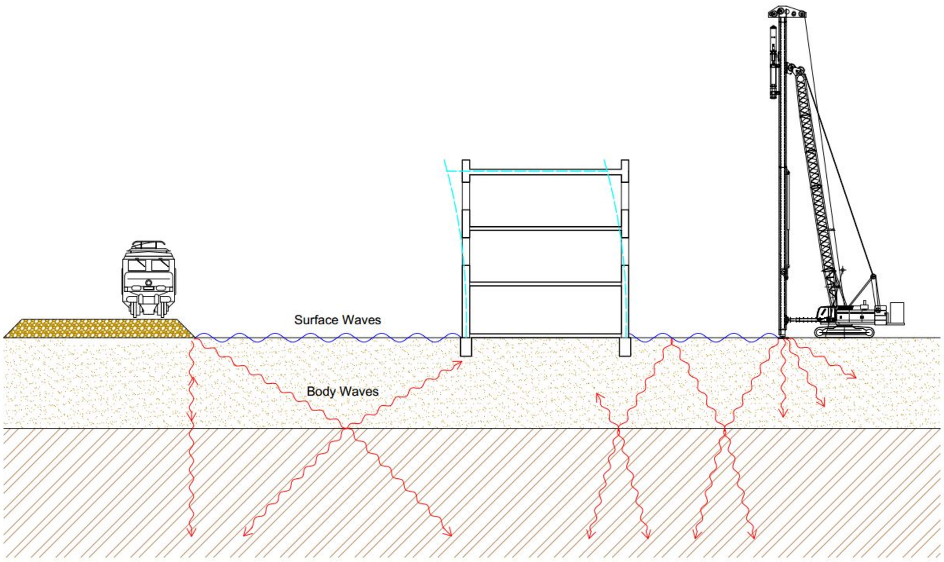

Fig. 1.1: Wave spreading induced by traffic and construction works provided with a resonance of a building (dwg blocks by [Cadforum, 2008]).

1.1 Statement of intent

This project will focus mainly on ground-borne noise resulting from trains, which have a dominant frequency range of about 16 Hz to 100 Hz [Zapfe et al., 2009], which is in the range of human perception of whole body vibrations ($1-80$Hz), [ISO, 1997]. Also frequencies lower than 16 Hz can result in structure-borne vibrations, causing the building to vibrate at lower eigenfrequencies which can further be perceived by humans and therefore leading to greater discomfort. These ground-borne vibrations, are transmitted to the buildings through the soil, see illustration in Figure 1.1, hence a thorough investigation of waves propagation in soils will lead to better understanding of the causes and consequences of these effects.

Different frequencies will generate waves with different wavelengths but their propagation will greatly depend on the type of soil they are travelling in to. Normally waves tend to attenuate when travelling in the soil, but the type of soil will determine how fast the energy of these waves will be lost. Therefore in order to examine the behaviour of these waves, first the influence of the material properties of the soil has to be analysed.

Nowadays, there are two main manners to assess wave propagation in soils. First way, used from early days, is to measure the vibrations in-situ or experimentally by use of geophones or accelerometers. This is still the most precise method as it is provided only with physical and measurement uncertainties. On the other hand, it is very time consuming and expensive way of wave assessment. The second manner is related to the application of complex computational models. As the new technologies arises and the computational power increases these models are becoming efficient tools in geotechnical engineering. The computational models are fast and also precise, but on the other hand there are additional model and also statistical uncertainties for input data. They also do not require expensive apparatus and technical staff what usually are an extra and high cost. Hence, the introduction of a new computational model with acceptable accuracy on simulating ground-borne vibrations will be inside the scope of this project.

1.2 Project description

A semi-analytical model was developed by several researchers from Aalborg University, Aarhus University, Denmark, Lund University, Sweden and COWI A/S and is further improved, in the context of Urban Tranquillity project, by associate professor Lars Andersen and PhD fellow Paulius Bucinskas in order to estimate the vibrations induced from ground-borne sources. The aim of this thesis, will be to validate and calibrate the computational model based on field data measured from train induced noises. This method involves a semi-analytical solution for a horizontally stratified medium, which in comparison to the finite element method is much more time efficient.

First, a detailed description of the basic theory of elastodynamics is presented, according to Andersen [2006], Kramer [1996] and Semblat and Pecker [2009]. Here, the reader will be introduced to the properties and behaviour of wave propagation into the soil, including the main types of waves and their movement in a half-space or a stratified media. Since most soil material have complex behaviour and different properties, for the sake of simplification the soil will be assumed to be isotropic and homogeneous with linear material properties and (visco)elastic behaviour, even though in nature most materials show some degree of non-linear elasto-plastic response, inhomogeneity and anisotropy [Andersen, 2006].

In the following two chapters a sensitivity analysis of soil parameters will be performed by making use of the model. Not all soil parameters will induce the same change in the response, therefore a separation of the most influential parameters will be conducted and analysed further. A thorough investigation and interpretation of the soil properties in the semi-analytical model will lead the path for the final stages of the project where a better understanding of the model and soil properties is required.

The project includes also an experimental part. During this phase, geophones will be used to measure the vibrations induced from a train at different distances from the source. Ellidshøj, Svenstrup J in Denmark is chosen as the location where the experiment will be conducted based on agreement with COWI, who is the provider of the equipments. Information about the tests that will be carried out and the use of the equipment will be described during this part.

In the final part of the project a simulation of the actual site has to be established in the model. The measured data is used for the calibration and estimation of the soil stratigraphy and soil properties. However, there are uncertainties related to the properties of soil, since no triaxial test will be performed during this project therefore a close and accurate estimation of some the properties has to be assumed. Furthermore, in order to represent reality the best possible, the force generated by the train has to be replicated in the model and the formulation for this is discussed here.
To conclude, the results obtained from the experiment and the ones obtained from the semi-analytical model will be compared to each other in order to find as close fit as possible between the two.

2 | Theory of waves in viscoelastic soil

As nowadays man-made vibrations are more and more affecting urban areas the understanding of waves propagating through soil medium is of vital interest. This chapter explains the basic theory behind this phenomena. Governing equations for elastic soils and three main types of waves are introduced.

2.1 Governing equation of motion for three-dimensional waves

As the project is dealing with a real case problem, the propagation of three-dimensional (3D) waves in a volume has to be assumed. Therefore the governing equations defining the motion of three dimensional waves are introduced. In this case the soil is assumed to be elastic. If an infinitesimal cube, see Figure 2.1, is taken from the soil where the waves propagate and all internal and external forces are considered, then the equilibrium has to be fulfilled.

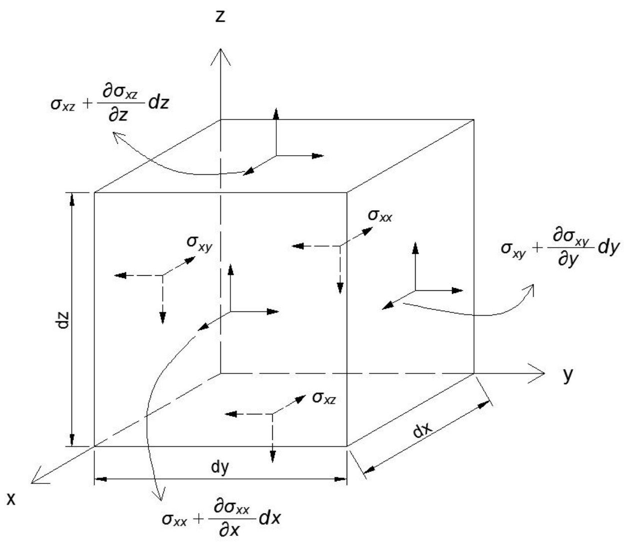

Fig. 2.1: Stress on an infinitesimal cube

The principle of equilibrium rests in the balancing of all external and internal forces acting on the cube. Each face of the cube has three stress components, each of them correspond to a direction. As the equilibrium has to be fulfilled, then the equation of motion is written in the form of Equation 2.1 in case of x direction.

$$
\begin{aligned}
\rho\, dx\, dy\, dz \frac{\partial^2 u}{\partial t^2} \quad = \quad & \left(\sigma_{xx} + \frac{\partial \sigma_{xx}}{\partial x} dx\right) dy\, dz - \sigma_{xx}\, dy\, dz \; + \\
& \left(\sigma_{xy} + \frac{\partial \sigma_{xy}}{\partial y} dy\right) dx\, dz - \sigma_{xy}\, dx\, dz \; + \\
& \left(\sigma_{xz} + \frac{\partial \sigma_{xz}}{\partial z} dz\right) dx\, dy - \sigma_{xz}\, dx\, dy
\end{aligned}
\tag{2.1}
$$

where

ρ	Material density $[kg/m^3]$
u	Displacement in x direction $[m]$
t	Time $[s]$
σ	Stress component $[N/m^2]$

This can be further reduced to Equation 2.2. The same formulation is also applied for y and z directions in Equations 2.3 and 2.4, where v and w are the displacements in these directions.

$$\rho \frac{\partial^2 u}{\partial t^2} = \frac{\partial \sigma_{xx}}{\partial x} + \frac{\partial \sigma_{xy}}{\partial y} + \frac{\partial \sigma_{xz}}{\partial z} \tag{2.2}$$

$$\rho \frac{\partial^2 v}{\partial t^2} = \frac{\partial \sigma_{yx}}{\partial x} + \frac{\partial \sigma_{yy}}{\partial y} + \frac{\partial \sigma_{yz}}{\partial z} \tag{2.3}$$

$$\rho \frac{\partial^2 w}{\partial t^2} = \frac{\partial \sigma_{zx}}{\partial x} + \frac{\partial \sigma_{zy}}{\partial y} + \frac{\partial \sigma_{zz}}{\partial z} \tag{2.4}$$

These equations are the so-called *Three dimensional equations of motion* that defines the wave propagation in a volume. It can also be written in index notation, see Equation 2.5, which is also called *Couchy equation*. This expression is dependent of the stress but more conveniently it is put in terms of displacements.

$$\frac{\partial \sigma_{ij}}{\partial x_j} = \rho \frac{\partial^2 u_i}{\partial t^2} \tag{2.5}$$

Assuming that the material behaves linearly elastic and only small deformations are considered, the stress-strain relation can be expressed by the *Hooke's law*. Equation 2.6 gives the expression in index notation.

$$\sigma_{ij} = E_{ijkl}\varepsilon_{kl} \tag{2.6}$$

where

E_{ijkl}	Elastic tensor $[N/m^2]$
ε_{kl}	Infinitesimal strain tensor [-]

Elastic tensor E_{ijkl} is composed of 81 components, where only 27 are independent, because both stress and strain tensors are symmetric. Therefore it is also subject of symmetry: $E_{ijkl} = E_{jikl} = E_{ijlk} = E_{klij}$.

Then, it is considered that the material is homogeneous, this means that the density and the elasticity tensor are both independent of position x. Moreover, the isotropic condition is also assumed which allows to write $Hook's\ law$ dependent on $Lame\ constants$ λ and μ as Equation 2.7 shows.

$$\sigma_{ij} = \lambda \Delta \delta_{ij} + 2\mu \varepsilon_{ij} \tag{2.7}$$

where Δ is the dilation, δ_{ij} is *Kronecker delta* and λ and μ are the Lamé constants which define the soil properties and are related to the Young's modulus, E, and Poisson's ratio, ν, see Equation 2.8. It should be noted that actually Lamé constant μ defines the shear modulus, G.

$$\lambda = \frac{\nu E}{(1+\nu)(1-2\nu)}, \qquad \mu = \frac{E}{2(1+\nu)} = G \tag{2.8}$$

The geometrical condition gives the relation between the strains and the displacements as Equation 2.9 shows. This formulation is provided by Kramer [1996].

$$\begin{cases} \varepsilon_{xx} = \dfrac{du}{dx} & \varepsilon_{yy} = \dfrac{dv}{dy} & \varepsilon_{zz} = \dfrac{dw}{dz} \\ \varepsilon_{yz} = \dfrac{dv}{dx} + \dfrac{du}{dy} & \varepsilon_{xy} = \dfrac{dw}{dy} + \dfrac{dv}{dz} & \varepsilon_{zx} = \dfrac{du}{dz} + \dfrac{dw}{dx} \end{cases} \tag{2.9}$$

Finally, Equation 2.2 can be reduced to Equation 2.10, *Navier's equation*, assuming that the material is linear elastic, homogeneous and isotropic. This expression will be applied further in the project and also in the computational model for describing the waves motion in three dimensions.

$$(\lambda + \mu)\frac{\partial^2 u_j}{\partial x_i \partial x_j} + \mu \frac{\partial^2 u_i}{\partial x_j \partial x_j} = \rho \frac{\partial^2 u_i}{\partial t^2} \tag{2.10}$$

2.2 Body waves

In an infinite elastic medium two main three dimensional waves propagate, these are dilatation and rotational waves also known as P- and S-waves. As they are three dimensional they are commonly known as body waves.

P-waves: Are primary waves which induce volumetric but not shear deformations in the medium they are propagating through. The particle motion corresponds to a compression-dilatation and they propagate with a phase velocity c_P. The illustration of deformations produced by these waves can be seen in Figure 2.2

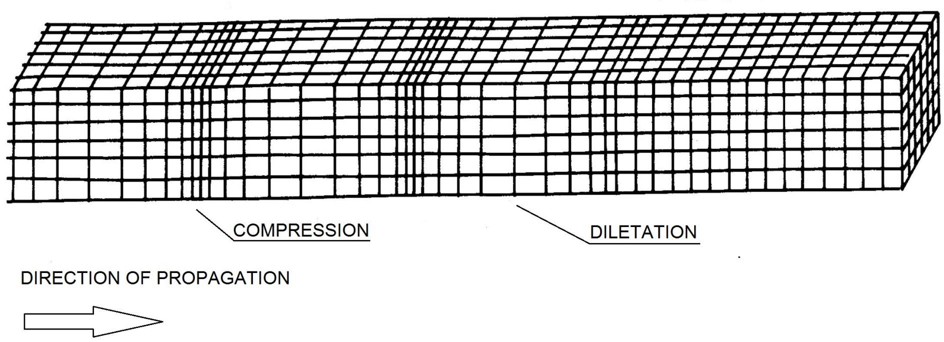

Fig. 2.2: Deformations produced by P-waves.

In order to get the wave equation for P-waves, the Navier's equation must be differentiated with respect to all directions and combined together. Then the following equation is reached:

$$\rho \frac{\partial^2 \varepsilon}{\partial t^2} = (\lambda + \mu)\nabla^2 \varepsilon + \mu \nabla^2 \varepsilon \tag{2.11}$$

where ∇^2 is the *Laplacian operator* and ε in this case represents volumetric strain. Then by knowing the following expression and rearranging following equation is obtained:

$$\frac{\partial^2 \Delta}{\partial x_i \partial x_i} = \frac{1}{c_p^2} \frac{\partial^2 \Delta}{\partial t^2} \tag{2.12}$$

What leads to the definition of the phase velocity for P-waves as Equation 2.13 shows. It can be seen that the P-wave phase velocity depends exclusively on the soil parameters G,ν and ρ. As the Poisson's ratio approaches a value of 0.5, meaning the body becomes incompressible, the velocity of the wave goes towards infinity. It should be noted that for isotropic elastic medium the phase velocity is spherically symmetric.

$$c_P = \sqrt{\frac{\lambda + 2\mu}{\rho}} = \sqrt{\frac{G(2-2\nu)}{\rho(1-2\nu)}} \tag{2.13}$$

S-waves : Are the secondary waves which take into account shear and rotation and are generally slower than P-waves. The nature of these waves is a shear movement of the particles with no volume change in the body, see Figure 2.3. This type of wave can be decomposed into a vertical component and a horizontal component depending on the particles displacement.

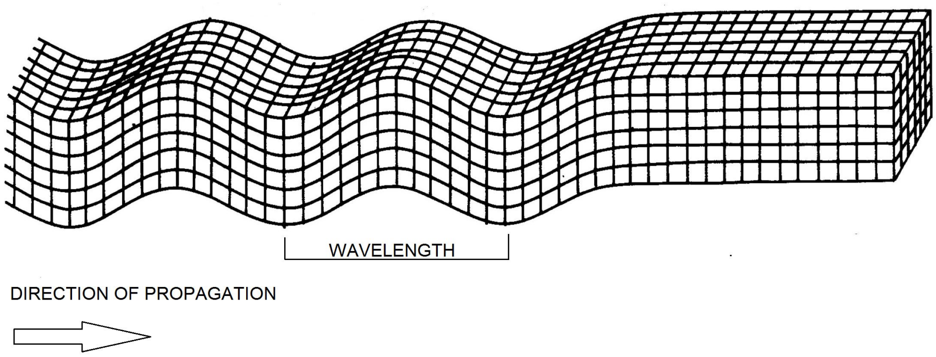

Fig. 2.3: Deformations produced by S-waves(vertical component).

In order to obtain the solution of these secondary waves, the rotation of the equation 2.11 is obtained. This is written as it follows:

$$(\lambda+\mu)\varepsilon_{ijk}\frac{\partial^3 u_l}{\partial x_l \partial x_k \partial x_j}+\mu\varepsilon_{ijk}\frac{\partial^3 u_k}{\partial x_l \partial x_l \partial x_j}=\rho\varepsilon_{ijk}\frac{\partial^3 u_k}{\partial t^2 \partial x_j} \tag{2.14}$$

where ε_{ijk} is a permutation symbol and can be 1, -1 or 0 depending on subsequence.

The first term of this equation can be deleted as the rotation of a divergence of a vector field is zero. Then the following expression can be reached and consequently the phase velocity for the secondary wave is obtained.

$$\frac{\partial^2 w_i}{\partial x_j \partial x_j}=\frac{1}{c_S^2}\frac{\partial^2 w_i}{\partial t^2} \qquad c_S=\sqrt{\frac{\mu}{\rho}} \tag{2.15}$$

where w_j is the rotation of the displacement field.

Notice that the particle motion of the S-waves is in a perpendicular plane to the wave propagation. Two types of S-waves are established, that is SH-waves, which are polarised perpendicularly to propagation direction in the horizontal plane and SV-waves in the vertical plane. Both components have the same phase velocity.

Finally some typical values for the P and S waves for different kind of soils are depicted below. See table 2.1. [Semblat and Pecker, 2009].

Tab. 2.1: Typical values for S- and P-waves velocities for different types of soil

Material	c_P [m/s]	c_P [m/s]
Clay	100-200	1500
Silt	100-200	1500
Dry Sand	200-400	400-800
Saturated Sand	200-400	1500-1700
Rock	>800	>2000

2.3 The Rayleigh waves

The model used in this project corresponds to a bounded space, that means that the influence of the surface on the wave propagation must be considered. For this reason, Rayleigh waves are introduced. The influence of having an interface or a surface will lead to some mixing of the body waves that can propagate along the surface of a half-space and their impact on the medium can be seen in Figure 2.4. These waves were first described by Rayleigh.

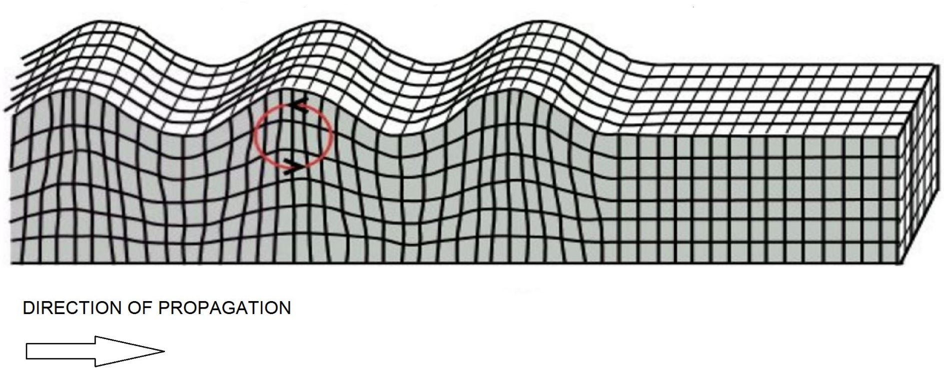

Fig. 2.4: Deformations produced by Rayleigh waves.

A semi-infinite space is considered in a linear elastic isotropic homogeneous material where a plane wave is propagating. Then, $z-axes$ is taken positive in the downwards direction and variation in y direction is not considered. The particle motion can be described by the P- and S-waves equations by potential functions, φ and ψ as follows:

$$c_p^2\nabla^2\varphi = \frac{\partial^2\varphi}{\partial t^2} \qquad c_s^2\nabla^2\psi = \frac{\partial^2\psi}{\partial t^2} \tag{2.16}$$

The solution for this wave equation, considering propagation of the waves only in $x-direction$, can be written as :

$$\varphi(x,z,t) = \Phi(x_3)e^{ik_p(sin\theta_p x - c_p t)} \qquad \psi(x,z,t) = \Psi(z)e^{ik_S(sin\theta_S x - c_S t)} \tag{2.17}$$

where

Φ and Ψ	Amplitude functions
k_P and k_S	Wave-numbers for P- and S-waves
θ_P and θ_S	Incident angle for P- and S-waves

Here Φ and Ψ describe the motion of particles with depth, since Rayleigh waves are surface waves, the particle amplitudes decreases with the depth.

Then the reduced waves-numbers can be introduced:

$$\gamma_P^2 = k_R^2(1-\frac{c_R^2}{c_P^2}) \qquad \gamma_S^2 = k_R^2(1-\frac{c_R^2}{c_S^2}) \tag{2.18}$$

These values must be positive, which means that the phase velocity of the Rayleigh wave is smaller than the phase velocity of P- and also smaller than S-wave.

The solution for this equation can be given by:

$$\Phi(z) = A_P e^{-\gamma_p z} + B_P e^{\gamma_p z} \qquad \Psi(z) = A_S e^{-\gamma_s z} + B_S e^{\gamma_s z} \tag{2.19}$$

where A and B are also amplitude functions which exponentially decrease and increase with depth variation. Some other term that does not follow the pattern, like increase with the larger depth, are deleted. Then the final expression for the potential fields can be written as it follows:

$$\varphi(z) = A_P e^{-\gamma_p z} + B_P e^{\gamma_p z} \qquad \psi(z) = A_S e^{-\gamma_s z} + B_S e^{\gamma_s z} \tag{2.20}$$

2.3.1 Rayleigh wave velocity

The Rayleigh wave frequency relation is obtained by applying the boundary conditions at the free surface. The expression is given by Andersen [2006] and it is written as follows:

$$(\gamma_S^2 + k_R^2)^2 - 4\gamma_P \gamma_S k_R^2 = 0 \tag{2.21}$$

By inserting 2.18 in this equation it is possible to obtain the so-called *Rayleigh equation*.

$$\left(2 - \frac{c_R^2}{c_S^2}\right)^2 = 4\left(1 - \frac{c_R^2}{c_P^2}\right)^{\frac{1}{2}} \left(1 - \frac{c_R^2}{c_S^2}\right)^{\frac{1}{2}} \tag{2.22}$$

The solution for this equation where $\frac{c_R}{c_S} = 0$ has no physical sense since this would mean that the Rayleigh wave is not propagating. Then the *Rayleigh equation* can be also written as follows:

$$\left(\frac{c_R}{c_S}\right)^6 - 8\left(\frac{c_R}{c_P}\right)^4 + (24 - 16\alpha^{-2})\left(\frac{c_R}{c_S}\right)^2 - 16(1 - \alpha^{-2}) = 0 \tag{2.23}$$

where $\alpha = \frac{c_P}{c_S}$. From this equation the Rayleigh wave velocity c_R can be calculated depending on the soil parameters just like P-wave velocity, c_P, and S-wave velocity, c_S. In Example A is shown the dependency of the phase velocities, for each wave type, for the variation of Poisson's ratio. The Rayleigh wave speed varies approximately between $0.85 - 0.95 c_S$ depending on ν.

Example A

A half space is considered for given soil properties. Then the P-waves, S-waves and Rayleigh waves are propagating with velocities c_P, c_S and c_R respectively.

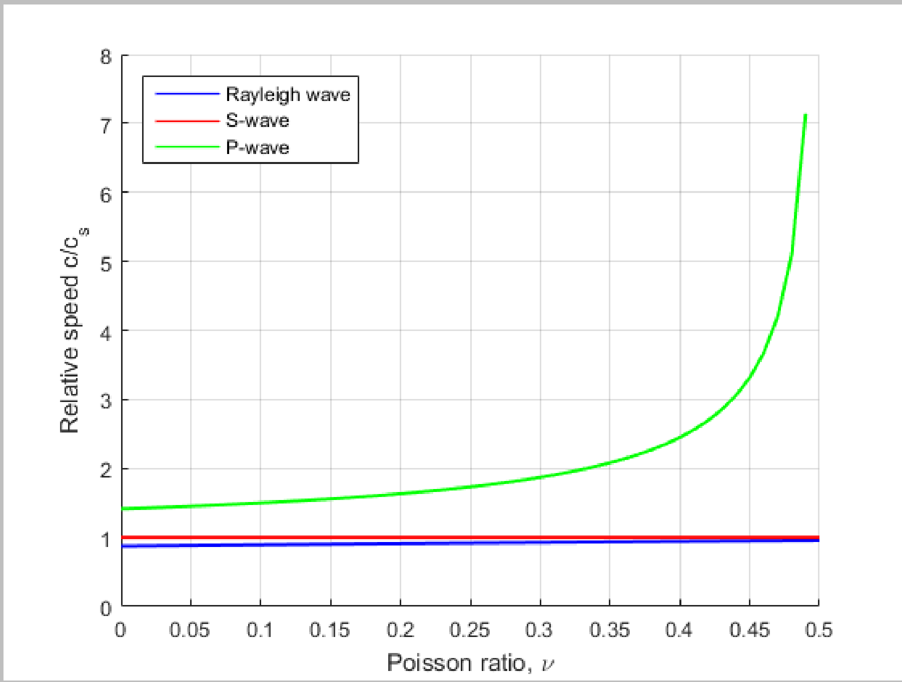

Fig. 2.5: Relative phase velocity

Figure 2.5 shows the phase velocities of the body waves and the Rayleigh waves normalized regarding S-wave phase velocity in the vertical axes against Poisson's ratio, ν, in the horizontal axes. As expected, the Rayleigh wave is the smallest one but it reaches values close to the S-wave velocity when very incomprehensible soils. On the other hand, P-wave phase velocity is the highest of the three and it increases considerably when Poisson's ratio reaches high values. Then it can be concluded that P-waves phase velocity gets affected with the degree of saturation of the soil, while the S-wave is independent of ν and therefore has constant velocity. This occurs due to the fact that a fluid cannot transmit shear waves.

2.3.2 Particle motion for Rayleigh wave

Rayleigh wave can be understood as superposition of two waves, one longitudinal and one transversal. Both are propagating with the same speed but with the difference of their energy dissipation due to the depth. Therefore their resulting horizontal and vertical components of displacement field are 90° out of phase from each other, where the vertical component is of higher magnitude to the horizontal one. As the result the particle motion creates elliptical shape. The direction of the motion is retrograde on the surface but at approximate depth of 0.15 - 0.20 of the wavelength the direction is reversed, see Figure 2.6.

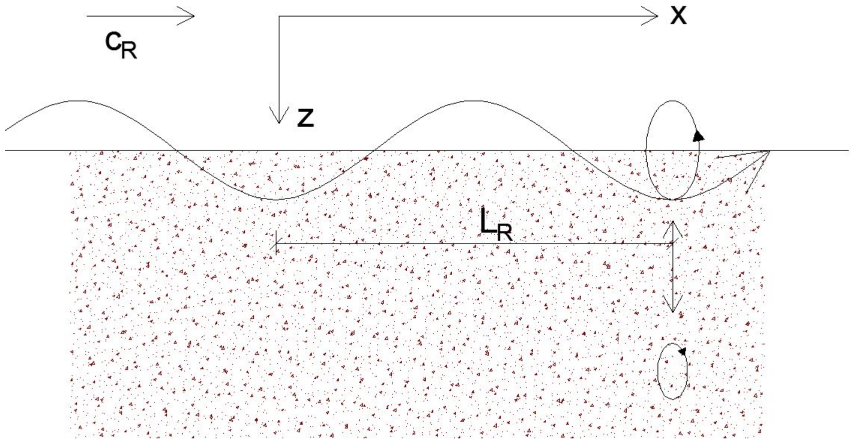

Fig. 2.6: Particle motion for a Rayleigh wave.

Another important characteristic of the Rayleigh wave is that the amplitude of particle motion rapidly decreases with increasing depth. This can be seen in Figure 2.7 where the horizontal and vertical components of the displacement amplitudes are plotted against depth with various Poisson's ratios.

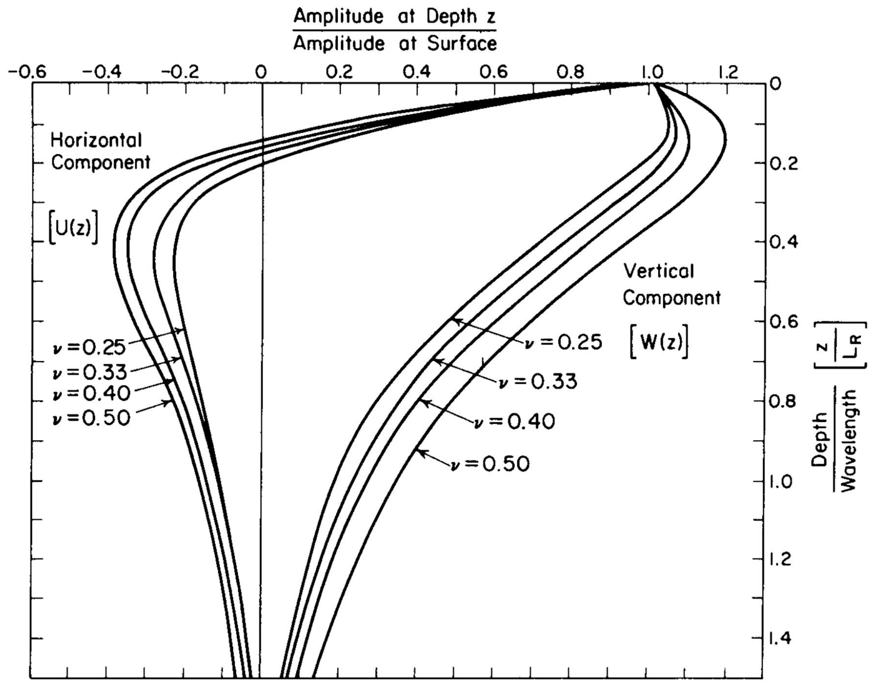

Fig. 2.7: Amplitude ratio over dimensionless depth horizontal and vertical component of Rayleigh wave in homogeneous half-space [Kramer, 1996].

It should be noted that the maximum amplitude of the vertical component is not located on the surface as one would expect but at same depth where the particle motion changes direction. Moreover at the depth of two wavelengths the amplitude decreases about 99 % of the original value. Therefore if for example the top soil layer is of depth larger than two wavelengths the bottom soil is almost not affected by this wave.

2.4 Reflection and transmission of waves in a layered body

2.4.1 One-dimensional case

When a layered body is considered instead of a homogeneous half-space, propagation of body waves will be affected from the boundaries. Hence, when an incoming P- or S-wave hits these boundaries or interfaces, part of the waves will be reflected and transmitted. The incoming wave that will be travelling towards the interface is also known as the incident wave, and the nature of its reflection will be strongly dependent on the boundary conditions. For one-dimensional waves propagation, the wave equation is:

$$\frac{\partial^2 u}{\partial x^2} + \frac{\rho b}{c^2} = \frac{1}{c^2}\frac{\partial^2 u}{\partial t^2} \tag{2.24}$$

where $b = b(x,t)$ are the body forces applied in the direction of particle motion per unit length. The total displacement field after the waves hit the boundary (i.e. at $x = 0$) will consist of the incident wave propagating in the positive x-direction and the reflected wave propagating in the negative x-direction. The total displacement field can then be obtained as follows, by assuming no change in amplitude or shape of the wave:

$$u(x,t) = U^i f(ct + x) + U^r f(ct - x) \tag{2.25}$$

where

U^i	Amplitude of the incoming wave
U^r	Amplitude of the reflected wave
f	Function related to shape and wave propagation

As mentioned before, the displacement field will be influenced from the boundary conditions, which can be described as:

- Dirichlet condition, where $u(0,t) = 0$
- Neumann condition, where $-\frac{\partial u}{\partial x} = 0$

The Dirichlet condition, also known as the natural boundary condition, corresponds to the case of a fixed boundary, i.e. soil is completely fixed at the interface and no displacement can occur. While the Neumann condition or the mechanical boundary condition corresponds to the case of a free boundary, i.e. a free surface with no traction applied. In both cases full reflection of the incident wave will occur, with same amplitude but a difference in phase shifts.

So far only the reflection of the waves at the boundary is considered, but that is not always the case, as when a wave hits an interface, part of the energy is also transmitted from one material to the other. In order to demonstrate how the waves behave when encountering an interface in the one-dimensional case, lets consider a rod subjected to a traction that generates waves in the positive x-direction, as shown in Figure 2.8.

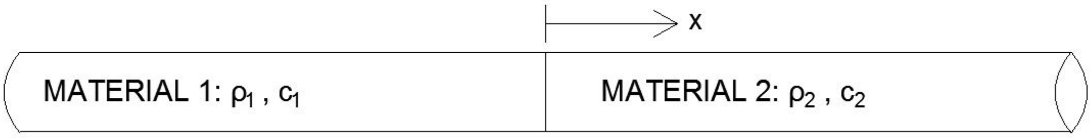

Fig. 2.8: Rod made up of two different materials.

The rod consists of two materials with different properties, separated at the interface $x = 0$. Part of the rod defined by $x \leq 0$ has material parameters ρ and c_1, while the material that occupies the space of $x > 0$ is defined by ρ_2 and c_2. Parameters ρ_1 and ρ_2 correspond to the mass densities of the material, while c_1 and c_2 are the phase velocities of the wave propagation.

When the incident wave, travelling in material 1, hits the interface, part of the energy of the wave will be transmitted to material 2, while the remaining part will be reflected. The incoming and the transmitted waves, will both travel in the positive x-direction, while the reflected wave moves in the negative x-direction, as illustrated in Figure 2.9.

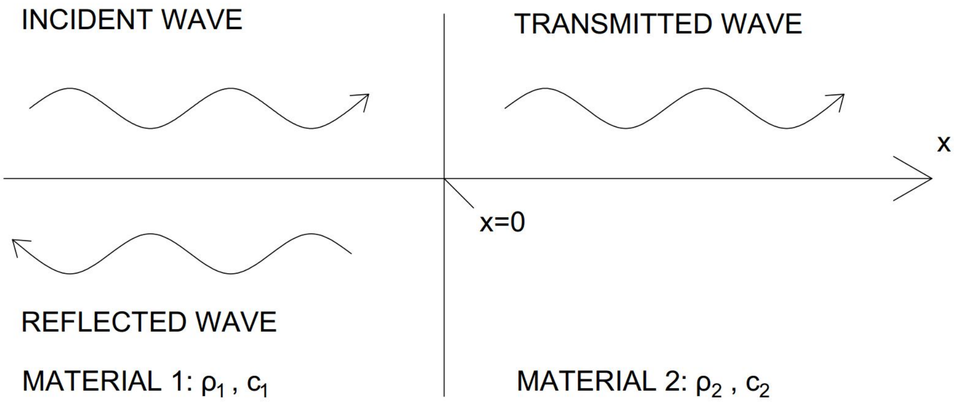

Fig. 2.9: Reflection and transmission of one-dimensional wave at an interface.

In that case, the total displacement field can the be described as:

$$u(x,t) = \begin{cases} u^i(t+x) + u^r(t-x) & \text{for} \quad x \leq 0 \\ u^t(x,t) & \text{for} \quad x > 0 \end{cases}$$

where the subscripts i, r and t correspond to the incoming, reflected and transmitted waves, respectively. Furthermore, the displacement fields for each travelling wave are found from the following equations:

$$u^i(x,t) = U^i f(c_1 t - x), \quad u^r(x,t) = U^r f(c_1 t + x), \quad u^t(x,t) = U^t f(c_2 t - x) \tag{2.26}$$

Since the incident and reflected waves both travel in material one, while the trasmitted wave travel in material 2, the displacement amplitudes of the waves, A, in the rod are related as follows:

$$A_i + A_r = A_t \tag{2.27}$$

An important quantity considered here is the *mechanical impedance* which is a fundamental property in the dynamics of material. This property is closely related to the material properties and will act as a basis in determining the amount of reflection and trasmittion at an interface. The mechanical impedance for both material will be:

$$z_1 = \rho_1 c_1 \qquad \text{and} \qquad z_2 = \rho_2 c_2 \tag{2.28}$$

and is related to the traction and displacement field based on the following equation:

$$p(t) = zv(t) \qquad \text{where} \qquad v(t) = \frac{\partial u}{\partial t} \tag{2.29}$$

The mechanical impedance varies for different materials, due to the relation with the density of the material and the wave velocity. And since the phase velocity of the waves depends greatly on the *Lame constants*, which are fundamental properties of the material, Equation 2.8, then the impedances can change drastically depending on the type of material. This variation in between impedances will lead to a considerable change in the amount of reflection and transmission at an interface, and a way to describe this effect is by the use of the *impedance mismatch*. This mismatch is found from the ratio between the mechanical impedance of the two materials, given as:

$$\alpha_z = \frac{z_2}{z_1} = \frac{\rho_2 c_2}{\rho_1 c_1} \tag{2.30}$$

The impedance mismatch has a high importance when determining the nature of the reflection and transmission at interfaces as it is closely related to the reflection and the transmission coefficients through the following equations:

$$C_r = \frac{A_r}{A_i} = \frac{1-\alpha_z}{1+\alpha_z} \qquad \text{and} \qquad C_t = \frac{A_t}{A_i} = \frac{2}{1+\alpha_z} \tag{2.31}$$

where C_r and C_t are the reflection and transmission coefficients, respectively.

Furthermore, the impedance mismatch can also be used to describe the reflection and transmission of the wave in terms of energy. Based on the fact that the power generated by the incoming wave should be equal to the power consumed by the transmitted and reflected waves, the following relation can be derived:

$$E_t = \frac{4\alpha_z}{(1+\alpha_z)^2} \qquad \text{and} \qquad E_r = 1 - E_t \tag{2.32}$$

where E_t is the energy-transmission coefficient, and E_r is the energy-reflection coefficient. So based on the impedance mismatch, an indication of the different types of behaviour can be described. These behaviours are demonstrated in the following example in the case of one-dimensional wave propagation.

Example B

In this example it will be shown how the velocity and energy coefficient vary as a function of the impedance mismatch and what that represents in terms of amount of reflection and transmission. This variation is illustrated in Figure 2.10.

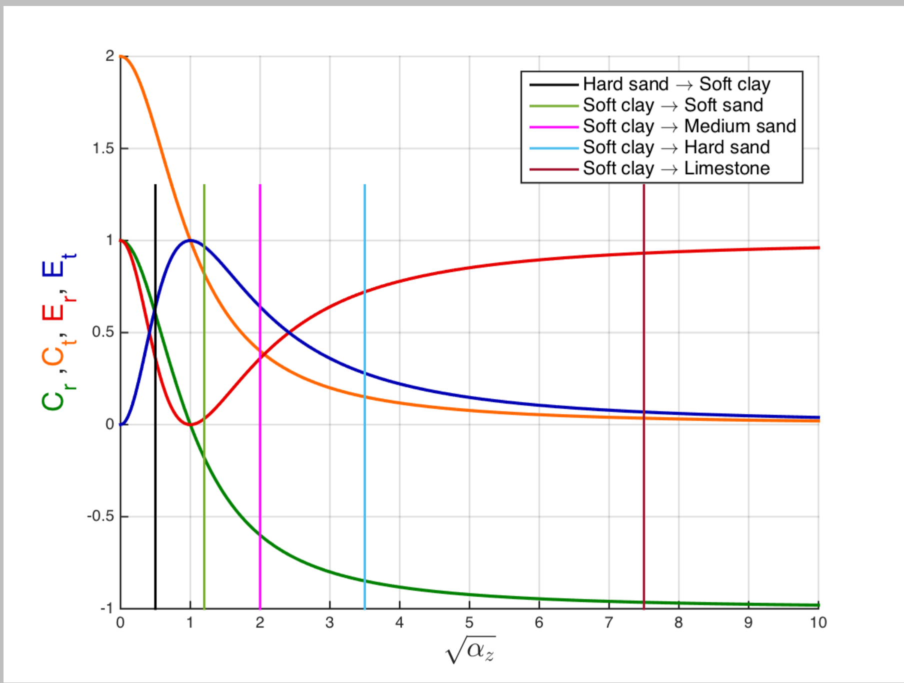

Fig. 2.10: Velocity and energy coefficients for reflection and transmission as functions of the impedance mismatch.

One can notice that when the impedance mismatch is equal to 1 then the energy transmission coefficient will also be one i.e. maximum, meaning that the whole energy of the incident wave will be transmitted and the amplitude of the transmitted wave will be the same as the incident wave, therefore there will be no reflection $E_r = 0$. This can indicate the case where soft clay overlays another layer of soft clay, and the media will act as a half-space where the boundary will not have any influence.

Furthermore, in the case that the impedance ratio is less than 1, it indicates that the wave is approaching a softer material. For example if a wave travels from a stiff material, like hard sand, to a material like soft clay, the phase velocity will be higher in the stiffer material which will further result in a larger impedance leading to a small impedance mismatch. When the impedance mismatch is 0, it will correspond to the situation situation of a free boundary i.e. an interface between a dense material and a very light and flexible material, satisfying the Neumann boundary condition. This implies that no transmission will take place and the incident wave will be fully reflected.

On the other hand, if the impedance ratio is bigger than 1 and it is headed towards infinity, the energy transmission coefficient will approach 0 while the energy reflection coefficient will approach 1. This case will correspond to a fixed boundary where mainly reflection will take place. It can be described as the case where the incident wave is approaching a stiffer material. This will be the opposite case of the above mentioned example, where the travelling wave will pass soft from clay to limestone leading to a smaller impedance in the softer material in comparison to the stiffer material.

2.4.2 Two or three-dimensional case

In addition to the one-dimensional case described above, the incident waves can travel towards the interface or the boundary with an inclined angle. The orientation of the inclined body wave has a strong influence on the energy of the wave that is reflected or transmitted. This relation can be based on Snell who showed that:

$$\frac{\sin\theta}{c} = \text{constant} \tag{2.33}$$

where,

θ	Angle of the wave to the interface
c	Velocity of the body wave

The relationship in Equation 2.33 holds for both reflected and transmitted waves and it shows that the travelling wave will be refracted on the other side of the interface when the wave propagation velocities are different. In other words part of the energy of the incident wave will propagate into the adjacent layer. Although this will not be the case when $\theta = 0$.

In order to demonstrate how the reflection and transmission take place between P-waves and S-waves, two half-spaces of different elastic materials in contact with each other are considered in the $x_1 - x_3$ plane. They are separated by an interface situated at $x_3 = 0$, where the bottom part of the half-space, defined by $x_3 > 0$, has material properties G, ν, ρ, c_S, c_P, σ_{ij}, ψ_i, φ and u_i, while the material properties for the uppermost half-space $x_3 < 0$ are given by $\bar{G}$, $\bar{\nu}$, $\bar{c}_S$, $\bar{c}_P$, $\bar{\sigma}_{ij}$, $\bar{\psi}_i$, $\bar{\varphi}_i$ and $\bar{u}_i$. They are subjected to an incoming plane harmonic wave travelling towards the interface with an angle, as shown in Figure 2.11.

The distribution of the energy of these waves is determined based on the requirements of equilibrium and compatibility and theory of elasticity as described in the previous section. Although in this case, the reflection and transmition of the body waves is studied from the concept of *Helmholtz* decomposition, which makes use of the *Helmholtz potentials* to describe the displacement field. The displacement field then becomes:

$$u_i(\mathrm{x},t) = \frac{\partial\varphi(\mathrm{x},t)}{\partial x_i} + \varepsilon_{ijk}\frac{\partial\psi_k(\mathrm{x},t)}{\partial x_j} \tag{2.34}$$

where the scalar field $\partial\varphi(\mathrm{x},t)$ and the vector field $\partial\psi_k(\mathrm{x},t)$ are the referred to as the *Helmholtz potentials*, with the first one being rotation free while the other is divergence free. By inserting the decomposed displacement field into the homogeneous Navier equations, four equations are obtained:

$$\frac{\partial^2\varphi}{\partial x_j\partial x_j} = \frac{1}{c_P^2}\frac{\partial^2\varphi}{\partial t^2}, \qquad \frac{\partial^2\psi_i}{\partial x_j\partial x_j} = \frac{1}{c_S^2}\frac{\partial^2\psi_i}{\partial t^2} \tag{2.35}$$

For plane harmonic P- and SV- waves, the variation of the displacement field with time implies a wave field as:

$$u_i(\mathrm{x},t) = U_i(\mathrm{x},\omega)e^{\mathrm{i}\omega t} \tag{2.36}$$

where,

$U_i(\mathrm{x},\omega)$	Amplitude function
ω	Angular frequency

Furthermore, the spatial variation is described in terms of the wavenumber, by taking into account also the direction of wave propagation, r_i, which is defined as:

$$k_i = r_i \frac{\omega}{c} \tag{2.37}$$

By using the above definitions, the displacement field for harmonic plane waves becomes:

$$u_i(\mathrm{x}, t) = A_i e^{\mathrm{i}(k_j x_j - \omega t)} \tag{2.38}$$

Here, A_i is the amplitude of the wave, which can be used to describe the amplitude of the incoming wave and also the amplitude of the reflected and transmitted waves.

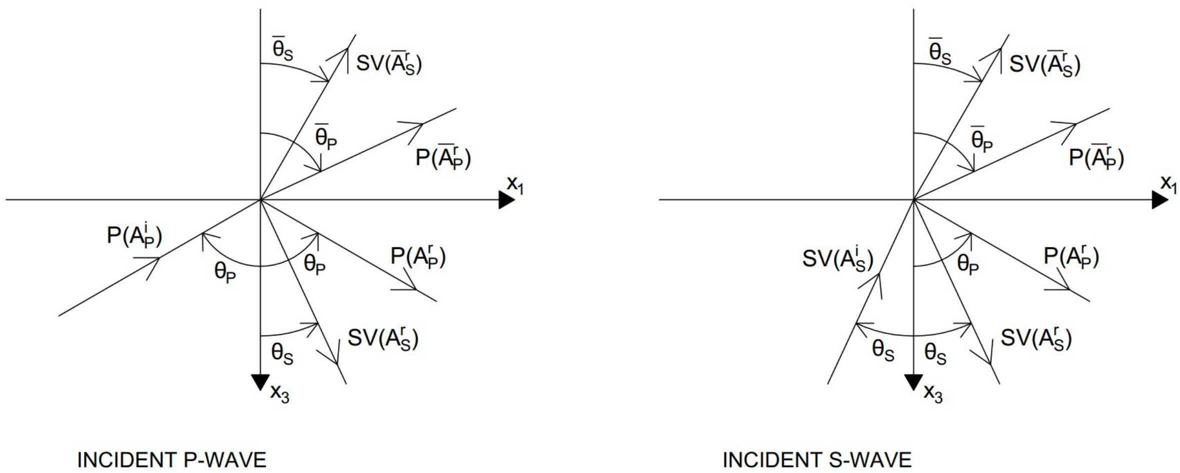

Fig. 2.11: Reflection and refraction of body waves at an interface.

By referring to Figure 2.11 one can see that when an incoming P-wave travelling in the direction r_P and angle θ_P hits the interface, it will produce both reflected and transmitted P- and SV-waves. If a boundary is considered at $x_3 = 0$ direction instead of an interface, only reflection will take place. This will also be equivalent to the case if a very stiff material in the uppermost half-space overlays a very soft one leading to full reflection due to the high impedance mismatch as explained in the previous section.

In both cases, the behaviour of the incident wave after reflection will be defined in the same way, since the incident and the reflected wave travel in the same material. The only difference is that when a boundary is placed at $x_3 = 0$ there will be no wave transmission. Since incident and reflected waves travel through the same material, the angle of incidence will be the same as the angle of reflection for both P- and S-waves [Kramer, 1996]. These angles can be calculated from the following equation, which corresponds to *Snell's law* for elastic waves :

$$\frac{k_S}{k_P} = \frac{\sin\theta_P}{\sin\theta_S} = \alpha, \qquad \alpha^2 = \frac{2-2\nu}{1-2\nu} = \frac{c_P^2}{c_S^2} \tag{2.39}$$

Furthermore, the relative amplitudes of the reflected P- and S-waves, or the reflection coefficient can be found as follows:

$$\frac{A_P^r}{A_P^i} = \frac{\sin 2\theta_P \sin 2\theta_S - \alpha^2 \cos^2 2\theta_S}{\sin 2\theta_P \sin 2\theta_S + \alpha^2 \cos^2 2\theta_S}, \qquad \frac{A_S^r}{A_P^i} = \frac{2 \sin 2\theta_P \cos 2\theta_S}{\sin 2\theta_P \sin 2\theta_S + \alpha^2 \cos^2 2\theta_S} \tag{2.40}$$

Subscript r stands for reflected. In the case of incoming SV-waves, it will generate reflected SV-waves and possibly P-waves propagating in the medium from which the incident wave is originated and refracted SV-waves and P-waves crossing the interface and propagating in the second medium, [Semblat and Pecker, 2009]. The amplitudes of the reflected waves can be computed in the same as for the P-waves, and the equations are as follows:

$$\frac{A_S^r}{A_S^i} = \frac{\sin 2\theta_P \sin 2\theta_S - \alpha^2 \cos^2 2\theta_S}{\sin 2\theta_P \sin 2\theta_S + \alpha^2 \cos^2 2\theta_S}, \qquad \frac{A_P^r}{A_S^i} = \frac{-2\alpha^2 \sin 2\theta_S \cos 2\theta_S}{\sin 2\theta_P \sin 2\theta_S + \alpha^2 \cos^2 2\theta_S} \tag{2.41}$$

By inspection of Snell's law for elastic waves, Equation 2.39, a critical angle exists, $\theta_c = \theta_S$ for which the P-wave propagates parallel with the boundary. Therefore it can be said that in this case the wave is trapped at the boundary. If the incident wave will approach the free boundary at an angle $\theta_S > \theta_c$, only an SV-wave will be reflected.

On the other hand, the refraction of the waves that occur in the upper half-space $x_3 < 0$ is described from the angle $\bar{\theta}$ and the amplitude $\bar{A}_i$. The angle of refraction is related to the angle of incidence by the ratio of the wave velocities of the materials on each side of the interface. In this case the solution to Equation 2.35 for the two half-spaces for both reflected and refracted waves takes the form of:

$$\begin{aligned}
\varphi(\mathrm{x},t) &= A_P^i e^{\mathrm{i}(k_{Pj}^i x_j - \omega t)} + A_P^r e^{\mathrm{i}(k_{Pj}^r x_j - \omega t)} \\
\psi_2(\mathrm{x},t) &= A_S^i e^{\mathrm{i}(k_{Sj}^i x_j - \omega t)} + A_S^r e^{\mathrm{i}(k_{Sj}^r x_j - \omega t)} \\
\bar{\varphi}(\mathrm{x},t) &= \bar{A}_P^r e^{\mathrm{i}(\bar{k}_{Pj}^r x_j - \omega t)} \\
\bar{\psi}_2(\mathrm{x},t) &= \bar{A}_S^r e^{\mathrm{i}(\bar{k}_{Sj}^r x_j - \omega t)}
\end{aligned} \tag{2.42}$$

Based on the above solutions for the lower and upper half-space, the following conditions are obtained for the refracted waves:

$$\frac{\sin\theta_P}{\sin\bar{\theta}_P} = \frac{c_P}{\bar{c}_P}, \qquad \frac{\sin\theta_S}{\sin\bar{\theta}_S} = \frac{c_S}{\bar{c}_S}, \qquad \frac{\sin\theta_P}{\sin\bar{\theta}_S} = \frac{c_P}{\bar{c}_S}, \qquad \frac{\sin\theta_S}{\sin\bar{\theta}_P} = \frac{c_S}{\bar{c}_P}, \tag{2.43}$$

Same as for the case of SV-waves at a free surface, it is noted that waves may also be trapped in the interface. This will depend on the material properties of the two layers and on the nature and angle of incidence of the travelling waves. In contrast to the free boundary, here both reflected and refracted P-waves and possibly also the refracted SV-wave can be trapped.

If incoming SH-waves are considered, the situation is much simpler as only one reflected and refracted wave is present. This wave is described in the same way as previously and therefore Snell's law is used again to define the angle of propagation as:

$$\frac{\sin\theta_S}{\sin\bar{\theta}_S} = \frac{c_S}{\bar{c}_S} \tag{2.44}$$

The amplitude and angle of the refracted waves greatly depends on the material properties of the layer the incident wave is travelling into. Since the phase velocity of the wave decreases with decreasing the stiffness of the material the amplitude and the angle of the propagating wave will also change. For example, if we consider a realistic case where we have a layered media with stiffness increasing over depth, and an incident wave travelling towards the surface, the angle of the refracted waves will approach vertical direction as it goes through the layers and towards the surface.

2.5 Dispersion and dissipation

In this section the phenomena of dispersion and material and geometrical dissipation is explained. Both are related to change of wave properties as they are passing through the media.

2.5.1 Dispersion

Dispersion occurs when waves propagate at different wave speeds with respect to different frequencies or wavenumbers. It means that the propagation velocity is not only dependent on material properties. This causes the incident waves, represented as a short pulse, to spread out and change their shape, as they travel further from source throughout the time, as shown in Figure 2.12.

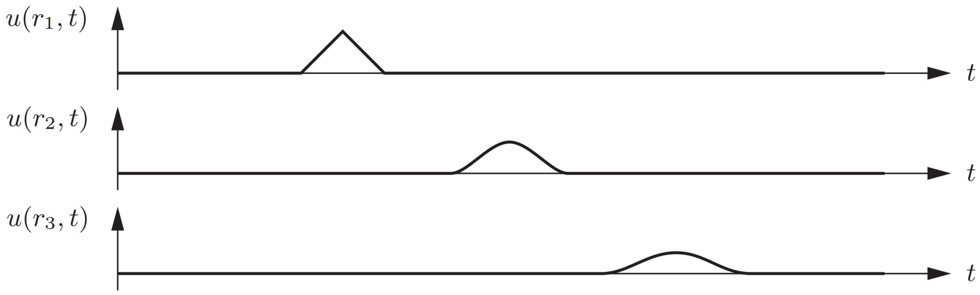

Fig. 2.12: Dispersion of pulse propagating along the bar at three different times [Andersen, 2006].

The principle of dispersion is that whereas the wave fronts propagate with the phase velocity presented by Equation 2.45 the energy propagation is on the other hand driven by group velocity which is defined in Equation 2.46. Each individual wave travels with velocity $c(k)$ which is faster than the group velocity $c_g(k)$ [Andersen, 2006].

$$c(k) = \frac{\omega}{k} \tag{2.45}$$

$$c_g(k) = \frac{\partial \omega}{\partial k} \tag{2.46}$$

Waves can be either dispersive or non-dispersive, which is based on whether their phase velocities are dependent on the frequency. In the case of non-dispersive waves the wave fronts propagate at the same velocity as energy, $c_g = c$. The three wave types, S-wave, P-wave and Rayleigh wave, described in sections above are considered as non-dispersive waves. This is due to the stated equations 2.13, 2.15 and 2.22 where the phase velocities of these waves are only functions of material properties as stiffness represented by Lamé constants, μ and λ, and mass density, ρ. It can be seen that these quantities are independent on the wavenumber and frequency.

This statement is valid in case of homogeneous media without any layers. In reality soil medium is stratified with different properties of each layer. This leads to situation when Rayleigh waves become dispersive. In low frequencies the Rayleigh wavelenghts are extremely large and therefore affect deeper areas of soil stratum. For example in Figure 2.13 one can see the behaviour of Rayleigh wave at low and high frequencies. In case where the top soil is softer than the bottom one, the velocity of low frequency waves is higher as the top soil layer is neglected and the velocity of the wave is based on the bottommost half-space soil parameters. This phenomena is further explained in Section 4.4.

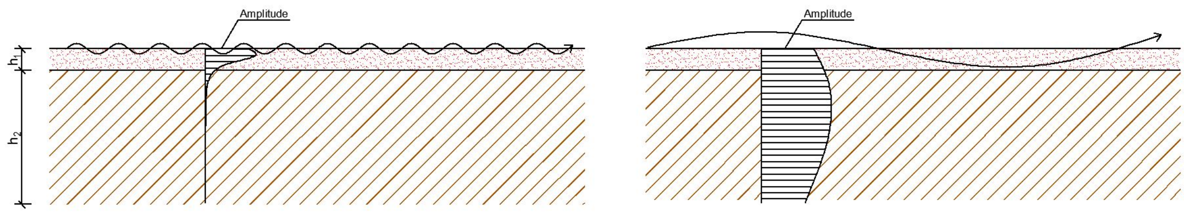

Fig. 2.13: Left: Rayleigh wave at high frequency. Right: The low frequency Rayleigh wave with large wavelength.

2.5.2 Dissipation

Dissipation is a phenomenon when the waves attenuate with distance and time. This attenuation is attributed to two sources. First is the geometry of the wave propagation problem, which is the primary and main cause of dissipation in most wave propagation problems. Secondly is the material dissipation due to the change of mechanical energy to heat, for which its influence highly increases as the waves propagate further from the vibration source.

Geometrical dissipation

Also known as geometrical damping, is a consequence of spreading out of mechanical energy over the volume. The reduction of energy over the distance causes decay of the amplitude of the stress wave. The degree of geometrical damping is highly dependent on the geometry of wavefronts, in other words in how many directions can the wave spread.

In case of P-wave and S-wave which are 3-dimensional waves they spread in three directions which creates spherical wavefronts. As the conservation of energy has to be abided, the energy per unit volume spreads at $1/r^2$ and the displacement amplitudes decrease at rate of $1/r$, where r is the distance from the source.

Surface waves, such as Rayleigh wave can propagate only in two directions and spread in cylindrical wavefronts. The dissipation of energy over distance is proportional to $1/r$ and therefore the displacement amplitude decrease by $\sqrt{1/r}$.

1-dimensional waves are not affected by geometrical damping as they propagate only in one directions and no energy spreading occurs. In order to demonstrate how the geometrical damping affects the different wave propagations over distance the following example is considered.

Example C

Here, the effect of the geometrical damping on the Rayleigh wave, and P- and S- wave is discussed. The dissipation of the energy of the waves as they travel in distance is shown in Figure 2.14.

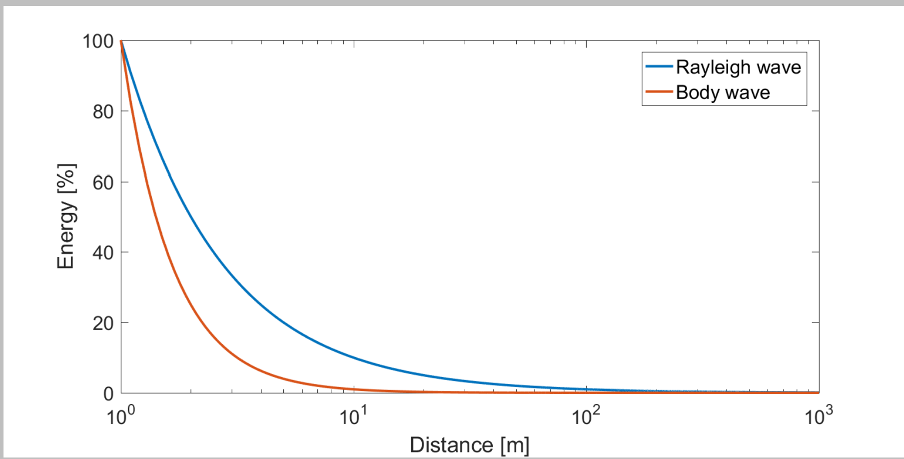

Fig. 2.14: Geometrical dissipation of energy for surface and body wave.

One can notice that the body waves dissipate their energy much faster than the Rayleigh wave as they move further. For instance, for the Rayleigh wave 10 % of the incident energy reaches the distance of 10 m, whereas only 1% of the body waves energy is present at the same point. This shows what was mentioned in the theory that the 2D waves i.e. Rayeligh waves, only travel in two directions and the dissipation of its energy happens at a ratio of $1/r$ in comparison to the 3-dimensional spread of the body waves. Also, the effect of the geometrical damping for all waves is highest at lower distances, where is it seen that the majority of the wave energy is lost until a distance of around 100 m. Therefore, the difference in geometrical attenuation is the reason why at a large distance from the point of load application the surface effects form the major part of the propagating disturbance, [Achenbach, 1973].

Material dissipation

The material damping is based on the conversion of mechanical energy to thermal energy. It is related to several mechanisms like friction between particles, molecular collisions or irreversible intercrystal heat flux [Andersen, 2006].

There are several models describing the material dissipation with respect to their frequency dependency. The mechanisms can be for example linear viscous damping, where there is linear relation between particle movement and damping forces, which is presented mainly in fluids. On the other hand damping can be completely independent on the frequency which is called hysteretic damping. For most soils there is intermediate frequency damping which means that the damping is not linearly proportional to frequency. The model used in this project takes into account the combination of these two types of material damping.

2.6 Summary

The basic theory for waves propagating in a viscoelatic media for the case of homogeneous and isotropic materials has been explained in this chapter. The main outcomes of the chapter are summerized below.

- **Body waves** are the only waves which can propagate through an elastic homogeneous medium. Their phase velocity is dependent on the stiffness and density of the material they travel through. There are two types of these waves:
  - **P-waves** are irrotational or compression waves which induce volumetric strain. The direction of particle motion is parallel to the direction which wave travels. The phase velocity is c_P.
  - **S-waves** are secondary waves which induce shear strains. The particle motion is perpendicular to wave direction. Phase velocity, c_S is smaller than c_P as soils are stiffer in volumetric compression than in shear and therefore P-waves travel faster. S-waves can be decomposed to **SH-** and **SV-waves**. SH-wave represents particle motion parallel to the surface or layer. SV-wave is vertical component taking into account vertical particle motion.

- **Rayleigh waves** are surface waves (motions occur only in a thin zone near the surface) producing both horizontal and vertical particle motion which follow retrograde elliptical pattern [Kramer, 1996]. Phase velocity is slightly lower than phase velocity of S-waves, $c_R \approx 0.9 c_S$. Their depth is highly dependent on the frequency of wave. For low frequencies particle motion occurs in higher depths than for high frequencies.

- As the body wave approach boundary between two layers with two different material properties the wave energy is partly **reflected**, and mostly **transmitted**. When a P-wave hits the interface, part of its energy is reflected as new P-wave and SV-wave and also refracted as a P and SV-wave.

- The wave behaviour of the incident wave after encountering a boundary is dependent on the **impedance mismatch** which is the ratio between **mechanical impedances** of two materials on both sides of the boundary. If the mismatch is equal to 1, then the wave is fully transmitted and on the other hand as it approaches 0 or infinity, the wave is fully reflected.

- S-wave, P-wave and Rayleigh wave are all non-dispersive waves. **Dispersion** of waves occur when the phase velocity of wave is directly dependent on the frequency.

- As waves travel through the media they are affected by the **material** and **geometrical dissipation** or damping, which means their amplitude is decreasing. Material damping is caused by the interaction between the wave and soil media where the wave energy is converted to heat. Geometrical damping is result of the spreading of energy over the larger volume as it travels away from source.

3 Evaluation of semi-analytic model for half-space

This chapter concerns an analysis of the computational model created in FORTRAN and further assimilated for use through MATLAB for simulating wave propagation in soil medium. The main idea is to test the model and compare the data to the theoretic concepts.

3.1 Soil modeling

The computational model simulates the soil by a discretization of the space by three degree of freedom points defining a half space. The model applies two different type of points. First, *discretization points* that define the space and second *observation points* that has been used in order to extract the response at a given location x, y and z in the space. In this chapter three observation points have been placed on the surface at 10 m, 25 m and 50 m away from the source where the waves are generated for a foundation radius $R = 1$ m. This allows a better study of the waves propagating in the space. Figure 3.1 gives an illustration of discretizied space and the *observation points*. There, the grey points are the *discretization points* defining the space and the three red points placed in line are the *observation points*. In the center of the space the green points define the foundation which is the source for waves generation.

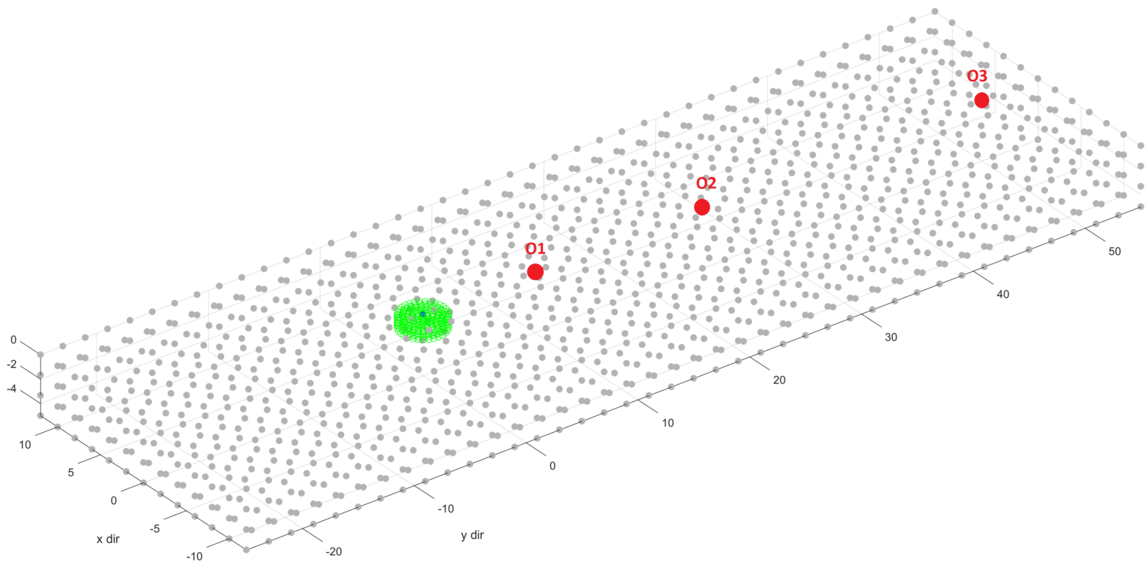

Fig. 3.1: Discretization of the space

Regarding the waves generation at the source, two different ways can be applied in the model. First, by applying a load at a rigid body of six degrees of freedom, three displacements and three rotations, this is called *Rigid Foundation*. Second, by applying the load on a $Flexible\ Foundation$. These two different ways of waves simulation will give different responses from the computational model. This analysis is developed in more detail in Section 3.6.

In order to introduce the $Flexible\ Foundation$ and $Rigid\ Foundation$, different profiles have been defined

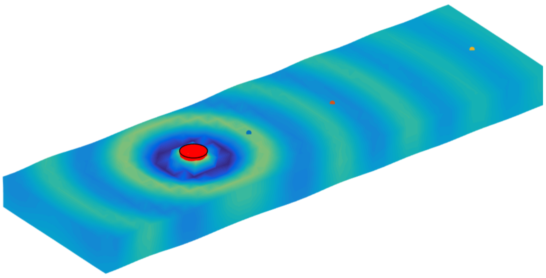

Fig. 3.2: Load applied at rigid foundation

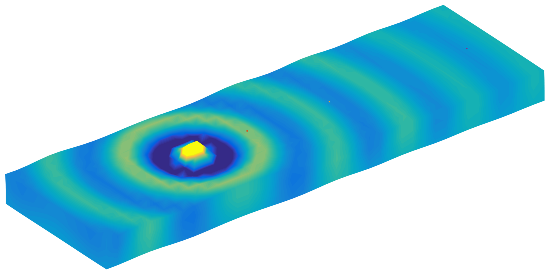

Fig. 3.3: Load applied at flexible foundation

in the model. These profiles describe the properties of the foundations such as geometry properties and application radius. In this chapter, a unitary load in the vertical direction has been applied. Figures 3.2 and 3.3 give an illustration of both, load applied on $Rigid\ Foundation$ and load applied on $Flexible\ Foundation$.

3.2 Formulation for Soil modeling

In reality the soil medium is usually irregular, anisotropic and non-homogeneous. There have to be assumed several simplification in order to be able to make a numerical model, save computational power and also still be able to solve the problem in a reasonable inaccurities. The Finite element method can be applied for modeling a layered half-space and get a precise solution for the wave prorogation in three dimensions. Nevertheless, this requires discretization of every point in a large volume and this leads to big and slow computational calculations since the global equations must be solve for every point defined in the model.

The simplifications considered in this model are that the soil is to be defined as linear viscoelastic, homogeneous and isotropic. Additionally the layers are to be modelled perfect flat and horizontal. An important consideration that will make the model faster is the transformation of the formulation in wavenumber-frequency domain since here the Green's function can be solved analytically and it reduces the computational time considerably. Then an inverse Fast Fourier Transformation (FFT) can be done to go back to space-time domain [Andersen and Clausen, 2008].

3.2.1 Formulation for modeling a layered half space

The description and principles of developed model is based on works Andersen [2006], Andersen and Clausen [2008] and Andersen and Clausen [2011] and are introduced in this section.

Considering a coordinate system given by the variables x, y and z, where x and xy define the horizontal plane and z changes with the depth and is taken positive downwards, See Figure 3.4. The displacements, u_i, and the traction, p_i, on the surface can be expressed in the space-time domain, see Equations 3.1.

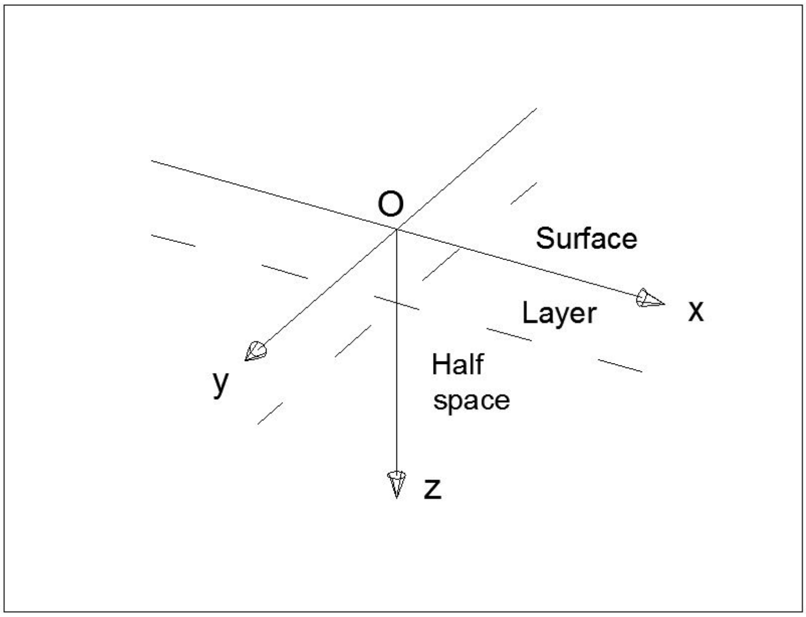

Fig. 3.4: Coordinate system for layered soil

$$\begin{cases} u_i(x,y,t) = u_i(x,y,0,t) \\ p_i(x,y,t) = p_i(x,y,0,t) \end{cases} \tag{3.1}$$

The displacements and the traction are related by the Green's function. This relation is between displacements in the direction i at the surface observation point $(x_1,\ y_1,\ 0)$ and time t and the load applied on the surface in the direction j at source $(x_2,\ y_2,\ 0)$ and time τ is given by $g_{ij} = g_{ij}(x_1 - x_2, y_1 - y_2, t - \tau)$.

Then the total displacements at the observation point can be expressed in space-time domain as it follows.

$$u_i^{10}(x_1,y_1,t) = \int_{-\infty}^{t}\int_{-\infty}^{\infty}\int_{-\infty}^{\infty} g_{ij}(x_1 - x_2, y_1 - y_2, t - \tau) p_j^{10}(x_2, y_2, \tau) dx_2 dy_2 d\tau \tag{3.2}$$

This expression describes the displacements at the surface due to a load applied at (x_2, y_2). Nevertheless, no analytic solution is possible for the layered soil in space-time domain. For this reason a conversion to wavenumber-frequency domain is needed.

It is assumed liner response from the stratum. Then the Fourier transformation of the displacements is carried out, first for the time domain to the frequency domain and then from space domain to wavelength domain. Then the following expression shows the displacements in frequency-wavenumber domain.

$$U_i(k_x, k_y, \omega) = G_{ij}(k_x, k_y, \omega)\ P_{ij}(k_x, k_y, \omega) \tag{3.3}$$

This equation has the advantage that no convolution is necessary. It gives the relation between displacements, $U_i(k_x, k_y, \omega)$, and the traction, P_{ij}, by the Green's function $G_{ij}(k_x, k_y, \omega)$.

3.2.2 Impedance matrix for a layered soil

A stratum is considered with j as the number of the considered layer. As it has been said previously the soil is assumed linear isotropic and homogeneous. The Navier's equation defines the wave propagation for the layer j in space-time domain as it follows.

$$(\lambda^j + \mu^j)\frac{\delta \Delta^j}{\delta x_i} + \mu^j \frac{\delta^2 u_i^j}{\delta x_k \delta x_k} = \rho^j \frac{\delta^2 u_i^j}{\delta t^2} \tag{3.4}$$

Here, λ^J and μ^J are the Lame constants that defines the material properties and Δ^J is the dilatation. This equation can be also calculated in wavenumber-frequency domain by applying the Fourier transformation. Then the following expressions can be obtained.

$$\begin{cases} (\lambda^J + \mu^J) ik_1 \Delta^J + \mu^J \left(\dfrac{d^2 U_1^J}{dx_3^2} - (\alpha_s)^2) U_1^J \right) = 0 \\ (\lambda^J + \mu^J) ik_2 \Delta^J + \mu^J \left(\dfrac{d^2 U_2^J}{dx_3^2} - (\alpha_s)^2) U_2^J \right) = 0 \\ (\lambda^J + \mu^J) \dfrac{d\Delta^J}{dx_3} + \mu^J \left(\dfrac{d^2 U_3^J}{dx_3^2} - (\alpha_s)^2) U_3^J \right) = 0 \end{cases} \tag{3.5}$$

where

λ^J	complex Lame's constant at layer J
μ^J	complex Lame's constant at layer J
Δ^J	Dilatation at layer J
ρ^J	mass density for layer J

Here the complex Lame constants λ^J and μ^J are introduce. The imaginary components of these constants add the material dissipation in the system.

Then the boundary conditions of the upper bound and lower bound of the layer are applied to the equations 3.6, the upper index 0 refers to the upper bound and 1 refers to the lower bound where h is the layer height.

$$\begin{cases} U_i^{j0}(k_1, k_2, \omega) = U_i^j(k_1, k_2, 0, \omega) \\ U_i^{j1}(k_1, k_2, \omega) = U_i^j(k_1, k_2, h^j, \omega) \\ P_i^{j0}(k_1, k_2, \omega) = U_i^j(k_1, k_2, 0, \omega) \\ P_i^{j1}(k_1, k_2, \omega) = U_i^j(k_1, k_2, h^j, \omega) \end{cases} \tag{3.6}$$

This data is put together in a S^J matrix with all displacements and tractions for the layer J.

$$\mathbf{S}^J = \begin{pmatrix} \mathbf{U}^J \\ \mathbf{P}^J \end{pmatrix} = \mathbf{A}^J \mathbf{E}^J \mathbf{b}^J \tag{3.7}$$

where A^J and E^J are both same dimension matrices and b^J is the vector that carries the integration constants.

Then it is possible to get the expression of the displacements and the traction at the boundaries, top boundary $\mathbf{S}^{j1}$ and bottom layer boundary $\mathbf{S}^{j2}$. This are related by the so-called transfer matrix $\mathbf{T}$. See equation 3.8.

$$\mathbf{S}^{j1} = \mathbf{T} \cdot \mathbf{S}^{j0} \tag{3.8}$$

This formulation, given by Thomson and Haskell [1953], defines a relationship between the deformations and traction at free surface with the displacements and traction at the interface of the layer and the half-space.

Then, below the layer J a half-space is identified as $J+1$. The displacements and traction at the half space are given as it follows. The vector b^J includes all the integration constants.

$$\mathbf{S}^{J+1} = \begin{pmatrix} \mathbf{U}^{J+1} \\ \mathbf{P}^{J+1} \end{pmatrix} = \begin{pmatrix} \mathbf{A}_{12}^{J+1} \\ \mathbf{A}_{22}^{J+1} \end{pmatrix} \mathbf{E}_{22}^{J+1} \mathbf{b}^{J+1} \tag{3.9}$$

This equation allows the relation between the displacements and traction between the bottom-most layer and half space.

$$\mathbf{U}^{J+1} = \mathbf{A}_{12}^{J+1} (\mathbf{A}_{22}^{1+J})^{-1} \mathbf{P}^{J+1} \tag{3.10}$$

Now, if only the half space is presented so no layers considered, $J = 0$, then from the equation 3.10 and the equation 3.3, it can be seen the relationship given by the matrix G_h, this called the Green's function matrix for this half-space case.

$$\mathbf{U}^{10} = \mathbf{G}_h \cdot \mathbf{P}^{10} \tag{3.11}$$

where $\mathbf{G}_h = \mathbf{A}_{12}^{10} (\mathbf{A}_{22}^{10})^{-1}$

Instead, if a layer is presented, some continuity equilibrium and equation 3.3 must be applied to get the following expression that provides the relationship between displacements and traction at the layer J.

$$\mathbf{U}^{J1} = \mathbf{A}_{12}^{J+1} (\mathbf{A}_{22}^{1+J})^{-1} \mathbf{P}^{J1} \tag{3.12}$$

By applying the equation 3.8 to get the relation for the different layers displacements and traction, the following expression is obtained.

$$\mathbf{U}^{10} = \mathbf{G}_{lh} \cdot \mathbf{P}^{10} \tag{3.13}$$

where $\mathbf{G}_{lh}$ is the Green's functions matrix for a layered space case.

Consequently, the Green's functions matrix allows the calculation of the displacements by knowing the traction $\mathbf{P}^{10}$. This equation can be inverted so the traction is calculated when the displacements are known. In this case the relation is given by the inverse matrix of $\mathbf{G}$. This new matrix is called the Flexibility or the Impedance matrix $\mathbf{Z}$. The following equation shows the relationship.

$$\mathbf{P}^{10} = \mathbf{Z} \cdot \mathbf{U}^{10} \tag{3.14}$$

3.3 Verification of wave propagation in the media

So far, in Chapter 2, the basic theory about the propagation of surface and body waves in a viscoelastic media was covered, giving an insight on when and where these waves have the highest influence. Here, the dominance of the different waves generated by the semi-analytical model in different directions will be studied and illustrated, in order to have a better overview and understanding of waves propagating in a medium.

When the waves are generated from a vertical or horizontal source, P-, SV- and Rayleigh waves are expected in the longitudinal direction. Furthermore, if the source is applied in the transverse direction then only SH- waves are generated which act independently of the others. The Green's function tensor has the format:

$$\mathbf{G}(\gamma,\omega) = \begin{bmatrix} G_{xx} & 0 & 0 \\ 0 & G_{yy} & G_{yz} \\ 0 & G_{zy} & G_{zz} \end{bmatrix} \tag{3.15}$$

The zeros in Equation 3.15 indicate missing interaction between the SH- waves, and P- and SV- waves. To demonstrate this, a homogeneous half-space is considered. The influence of the waves is studied for plane α on the surface, and for plane β situated at a certain depth in the media, see Figure 3.5. For each case, the response is measure in the x, y, and z direction based on the Cartesian coordinate system as shown in Figure 3.4.

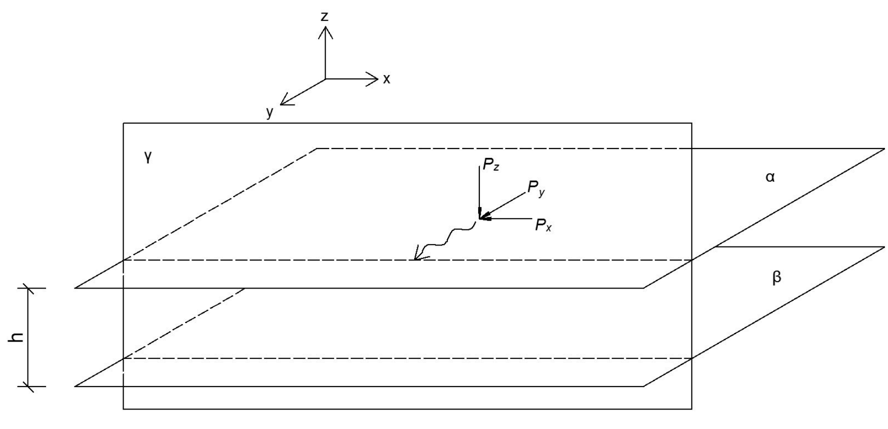

Fig. 3.5: Planes α and β through which wave propagates and plane γ as a reference observation plane.

The effect of the waves in each direction will be shown by the use of the dispersion diagrams. Even though the waves propagating into a half-space are non dispersive, they can still be detailed by the dispersion diagrams where each wave is described by a straight line since it travel ls with the same phase velocity throughout the soil and is independent of the frequency. In the first scenario, waves propagation in the transverse x-direction generated by a source applied in the same direction will be studied. This is demonstrated in Figure 3.6 for waves propagating in the surface and inside the medium, respectively.

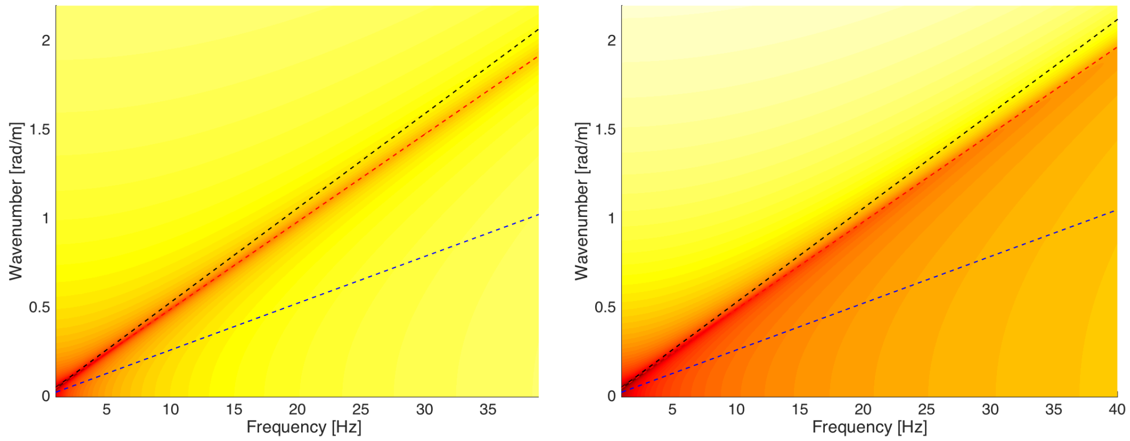

Fig. 3.6: Dispersion diagrams for half-space in x-direction. To the left: wave propagation in the surface and to the right: wave propagation inside the medium. Black lines represent Rayleigh waves, Red lines for S-waves, and Blue lines for P-waves. The dark red shades represent the response that correspond to a given combination of the frequency and wavenumber.

One can see from the figures that when the response is measured in the transverse x-direction, the dominant wave is the S- wave, more specifically SH-waves. This is shown by the dark red shade following the non-dispersive line of the S- wave. The same phenomenon is observed for both cases, in the surface and inside the media, although for the later one the influence generated from the SH-wave is much higher. These results fit well with the theory discussed, since the SH-wave is independent of the other waves.
The same methodology is applied for studying the influence of the waves in the longitudinal y-direction and vertical z direction, generated by a source applied in the y-direction, and the results can be seen in Figure 3.7.

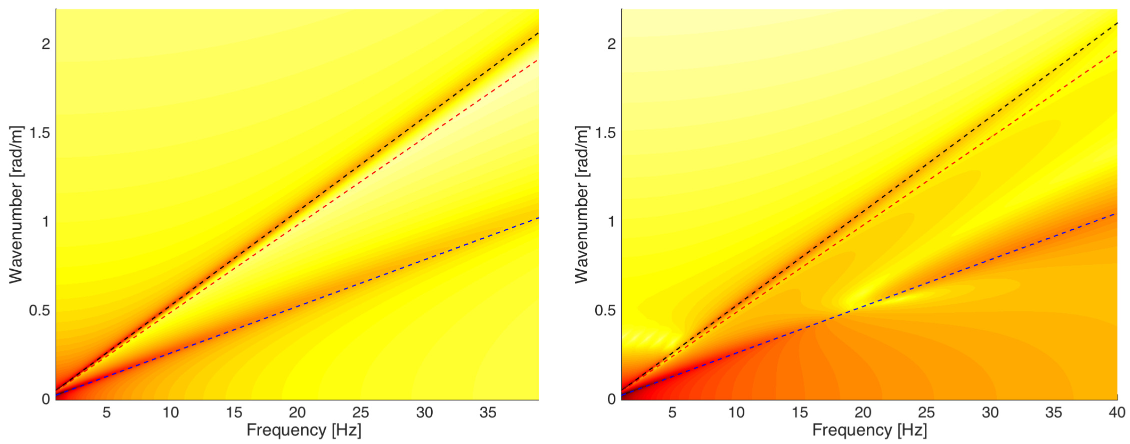

Fig. 3.7: Dispersion diagrams for half-space in y-direction. To the left: wave propagation in the surface and to the right: wave propagation inside the medium. Black lines represent Rayleigh waves, Red lines for S-waves, and Blue lines for P-waves. The dark red shades represent the response that correspond to a given combination of the frequency and wavenumber.

When the longitudinal direction is considered, there is no more effect coming from the SH- waves, and the dominant waves in this case are the P- wave and the Rayleigh wave, both in the surface and inside the medium. However, at a certain depth in the medium the effect of the P-wave increases in relation to the Rayleigh wave and that is shown by the spread of the dark red shades on the right side of Figure 3.7. At the meantime the effect of the P-waves increases in higher frequencies while the Rayleigh wave kind of dies out. There is also influence coming from the SV-waves since according to the Green's function in Equation 3.15 these waves are coupled although the influence is small.
For the last observation, the vertical z-direction is considered when a vertical source is applied, which is also the direction of reference where this project is focused on. The results are shown in Figure 3.8.

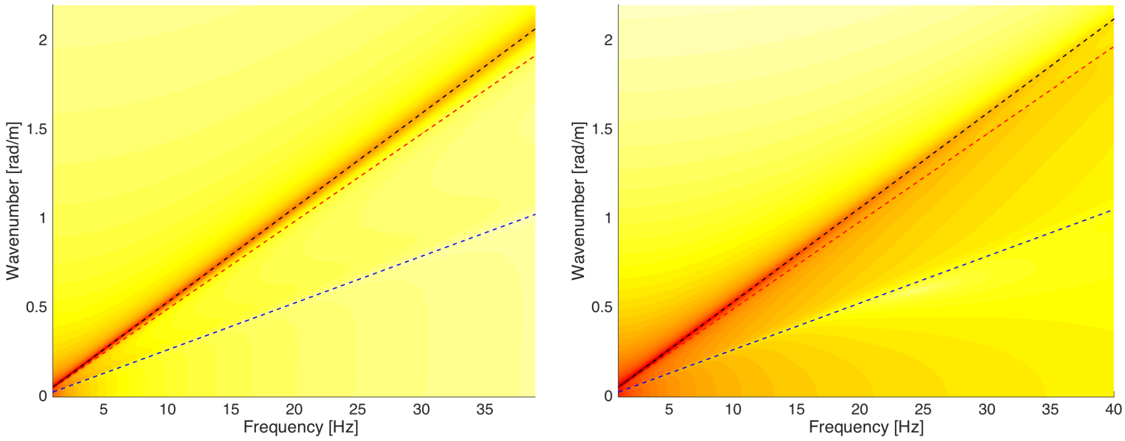

Fig. 3.8: Dispersion diagrams for half-space in z-direction. To the left: wave propagation in the surface and to the right: wave propagation inside the medium. Black lines represent Rayleigh waves, Red lines for S-waves, and Blue lines for P-waves. The dark red shades represent the response that correspond to a given combination of the frequency and wavenumber.

Here, one can see that there is only the influence of the Rayeligh wave and the wave travels with a speed which is equal to the speed of the Rayleigh wave. The same can be said for both surface and inside the medium, appart from the fact that inside the medium, at low-frequency range the effect of the Rayleigh wave seems more dominant while at high frequencies it is dissapearing slowly. This can be due to the fact that high frequency waves have shorter wavelengths therefore they may not reach a certain depth. Also in the medium there is more influence coming from the SV- waves, while the influence of the P-wave is very small. The fact that the Rayleigh wave is described as a surface wave travelling in only two directions correspond well to the results obtained from the semi-analytical model.

3.4 Soil parameter study for half space

The aim of the following section is to show the influence of the soil parameters in the response of the model. Multiple factors affect the response of the model such as the application load, the radius of the foundation and the soil parameters. The idea is to show only the influence of the soil parameters here and for that a normalization of the axes is done. Additionally, the sensitivity has been quantified by calculating the deviation of the response in terms of RMS and absolute peak ratio, APR. The *normalized response plot* has been determined first for a reference material and then this one has been applied for some different soil parameter cases. Thus, the influence in the response due to a change in a soil parameter can be evaluated.

Notice that this procedure is developed only for homogeneous half-space, see Figure 3.9. The studied soil parameters are as follows: *Poisson's ratio*, ν, and *Loss factor*, η. The response corresponds to an observation point located ten times the foundation radius, $10 \cdot R$, away from the source. This distance is chosen since it allows to measure fully developed waves but it also avoids big energy dissipation measurements which is the case for large distances. $Flexible\ foundation$ is applied in this simulation. It must be mentioned that the mass density, ρ, is not analysed in this study since it is assumed to have little influence in the response.

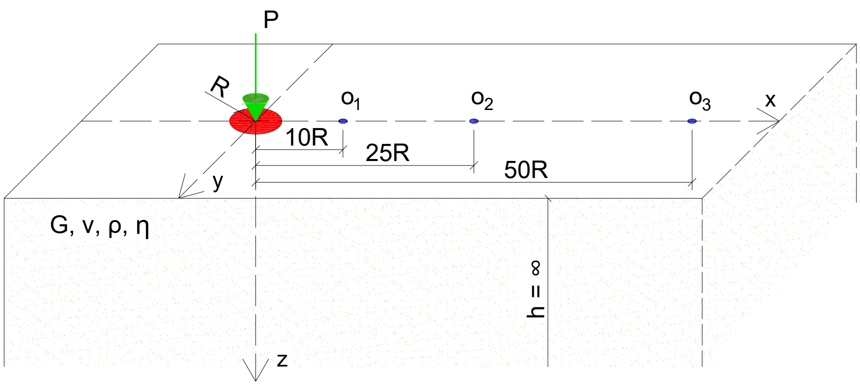

Fig. 3.9: Half space model.

This analysis is deterministic and the Table 3.1, based on Jensen et al. [2013] and Look [2014], has been used for having a precise idea of the soil parameters ranges. This table is also further used as reference in the soil parameter study for layered model.

Tab. 3.1: Soil parameter ranges.

	Shear Modulus G [MPa]	Poisson's ratio ν	Mass density ρ [kg/m^3]	Loss factor η
Clay	3-350	0.1-0.49	1600-2250	0.01-0.08
Silt	30-140	0.3-0.35	1600-2000	0.01-0.08
Saturated Sand	5-350	0.15-0.4	1700-2100	0.01-0.08
Dry Sand				0.01-0.08

3.4.1 Response normalization

The Frequency Response Function (FRF), in this case in terms of vertical displacements, is linearly dependent on several parameters like foundation radius, R, the shear modulus, G, and the applied load, P. This means that no matter how these variables are changed the function will always keep the same shape. Therefore the normalization, see Equation 3.16, can be performed where the FRF becomes independent on these variables. Moreover the frequency range is also normalized, in this case regarding the foundation's radius, R and the S- wave phase velocity, c_S. That leads to a non-dimensional frequency in the horizontal axis.

$$U_z' = \frac{U_z \cdot G \cdot R}{P} \qquad f' = \frac{f \cdot R}{c_s} \tag{3.16}$$

where

U_z'	Non-dimensional displacement
R	Foundation radius
P	Vertical load
f'	Non-dimensional frequency

A *reference normalized response plot* has been depicted for three different distances, $10 \cdot R$, $25 \cdot R$ and $50 \cdot R$. Later the first one is used for comparison, see Figure 3.10. The corresponding reference soil parameters are given in Table 3.2.

Tab. 3.2: Reference soil parameters.

Soil Parameters	Value
ν_{Ref}	0.3
η_{Ref}	0.04
ρ_{Ref}	2000 [kg/m^3]

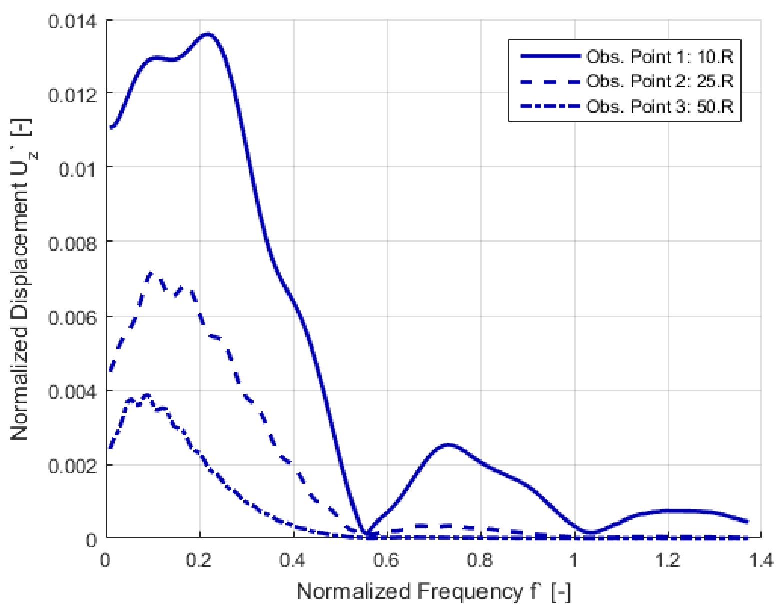

Fig. 3.10: Normalized response for reference soil parameters.

Further, when calculating the deviation of the response corresponding to a change in the soil parameters the RMS and Maximum peak ratio are obtained based on Equation 3.18 and 3.17. Then the deviation given by the RMS is normalized by the standard deviation.

$$RMS = \sqrt{\frac{\sum_{i=1}^{n}(u_1 - u_i)^2}{n}} \qquad RMS_{Normalized} = \frac{RMS}{\sigma} \cdot 100 \tag{3.17}$$

where

σ	Standard deviation
u_1	Reference Normalized response
u_i	Normalized response for case i

$$MPR = \frac{MP_i}{MP_{Ref}} \tag{3.18}$$

where

MRP	Maximum Peak Ratio
MR_i	Maximum Peak for response i
MR_{Ref}	Maximum Peak for Reference response

3.4.2 Influence of Poisson's ratio

First parameter study is performed on the variable Poisson's ratio, which can not be normalized like other parameters. It is a mechanical property of the material, but it is also highly dependent on water saturation level of the soil. For example in case of saturated clay, the Poisson's ratio reaches values close to 0.5 and in dry conditions it might significantly decrease.

In Figure 3.11 three cases with different Poisson's ratios are plotted to assess their influence on the frequency response function and are compared with the reference model.

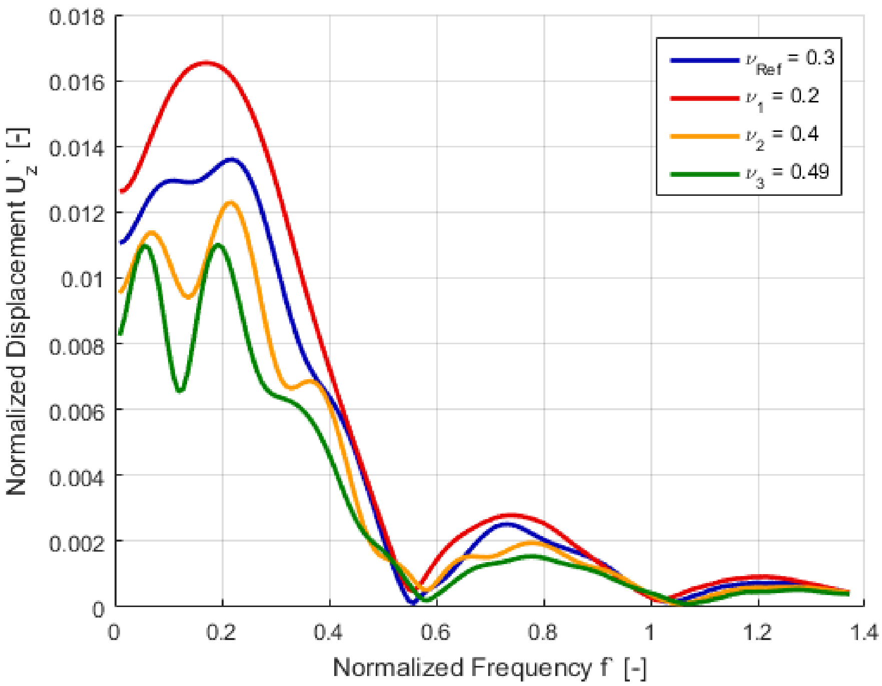

Fig. 3.11: Response for change in Poisson's ratio

Two main observations can be deducted from the figure. First one is the the overall decrease of the response of the model when ν goes towards value 0.5. This is due to the impact of the Poisson's ratio on the Young's modulus and therefore on the stiffness, meaning that with high stiffer soil the resulting response is lowered.
Second observation is the change of the shape of response function where higher ν is causing several additional peaks and the curve becomes more "wavy". The reason for this behaviour rests in the direct relation of ν on the phase velocity of P-wave, shown in Equation 2.13, and therefore for given frequencies the wavelenghts are changed. Moreover the Rayleigh wavelenghts are also changed as these are proportional to both S- and P-waves.

The RMS and the maximum peaks ratios are depicted in Table 3.3 for case A: comparison between ν_{Ref} and $\nu_1 = 0.2$, case B: comparison between ν_{Ref} and $\nu_2 = 0.4$ and case C: comparison between ν_{Ref} and $\nu_3 = 0.49$.

Tab. 3.3: Response deviation by RMS and Maximum Peak ratio.

Cases	Deviation by RMS	MPR
Case A	27.60 %	1.2158
Case B	24.87 %	0.9038
Case C	42.38 %	0.8100

3.4.3 Influence of loss factor

The loss factor gives an idea of the loss of energy in the material. In the computational model the combination of hysteretic and linear viscous damping is used. When waves propagate in soft soils the shear strains are higher than for stiff soils what leads to a development of higher damping. Usually soft soils loss factor reaches magnitudes close to $\eta = 0.08$. For stiff soils it can be around $\eta = 0.01$.

In this study, three cases of variable η are taken into account and are compared with the reference $\eta_{Ref} = 0.04$. The behaviour of the frequency response function can be seen in Figure 3.12.

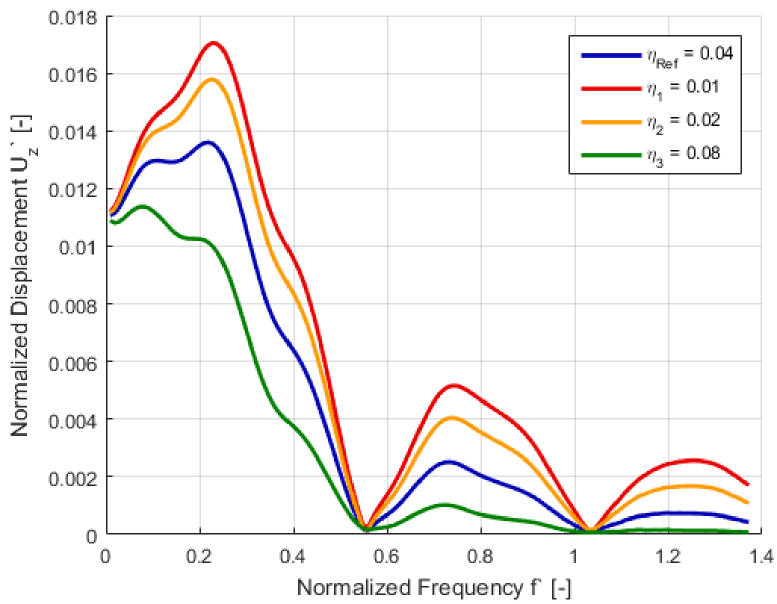

Fig. 3.12: Response for variation of the loss factor.

As seen in the figure the response of the function lowers down as the loss factor is increased. This is reasonable as the waves are damped much more and therefore causing lower displacements. Moreover it can be observed that there is even a higher decrease for high non-dimensional frequencies, f'. This makes sense since high frequency waves are related to more energy dissipation. This is due to the fact that the loss of energy happens for each oscillation of the wave. The most oscillations the higher the energy loss is.

The importance of material damping becomes more significant at the further distances where the geometrical damping does not play the main role, this can be further seen in Section 3.19.

The RMS and the maximum peak ratio are depicted in Table 3.4 for Case D: comparison between η_{Ref} and $\eta_1 = 0.01$, Case E: comparison between η_{Ref} and $\eta_2 = 0.02$ and Case F: comparison between η_{Ref} and $\eta_3 = 0.08$.

Tab. 3.4: Deviation of RMS and Maximum Peak ratio.

Cases	Deviation by RM	MPR
Case D	43.69 %	1.2532
Case E	17.79 %	1.0373
Case F	34.89 %	0.8357

3.5 Soil properties uncertainty modelling

The dynamic amplification of the response is strongly dependent on the material properties of the soil. These properties are normally characterized by a number of uncertainties, including spatial variability and also lack of measured data which can highly influence the variation of the response. To cover these uncertainties the soil properties are described using probabilistic models which include description of the soil parameters based on statistical analysis. The soil properties will be modelled as correlated variables since in reality they are expected to be dependent on one another and have a linear relationship. A simulation technique will be further applied to generate spacial variable values of the property of interest, [Jones et al., 2002].

3.5.1 Material correlation

The soil material properties tend to change in a linear way when one of the material properties changes, and the closeness of this relationship is described by the correlation coefficient ρ, see Section A.1. Values for the correlation coefficient vary from -1 to 1, with a positive value indicating a tendency that two variables will increase together, while a negative coefficient indicating the oppossite.

The shear modulus, G, the mass density, ρ, and the loss factor, η, are assumed stochastic variables which will be modelled as log-normal distributed variables since they cannot take on negative values and are good at modelling material strengths. On the other hand, Poisson's ratio will be modelled as Beta distributed to limit the interval of random variables to finite lengths, since the Poisson's ratio is upwards and downwards bounded, [Det Norske Veritas, 2012]. If the variables were modelled with a normal distribution they could take on negative values which will be non-physical for soil strengths, especially in the case were a high coefficient of variation is used, thereby this distribution is not considered.

The mean values of the shear modulus μ_G, density μ_ρ, loss factor μ_η, and Poisson's ratio μ_ν are assumed according to appropriate guidelines as described in Table 3.1. Here the coefficient of variation is used instead of the standard deviation in order to better control the dispersion, and their values are assumed on an engineering judgement based on their variability as illustrated in Table 3.5.

Tab. 3.5: Assigned distributions, assumed mean values and coefficient of variations for the material properties.

	Best Fit Distribution	Mean value μ	Coefficient of Variation CoV
Shear modulus G [MPa]	Log-normal	32	20 %
Density ρ [kg/m^3]	Log-normal	2000	10 %
Loss factor η	Log-normal	0.4	40 %
Poisson's ratio ν	Beta	0.25	20 %

In order to transform the material properties to correlated log-normal and beta distributed variables, the formulation illustrated in Figure 3.13 is applied.

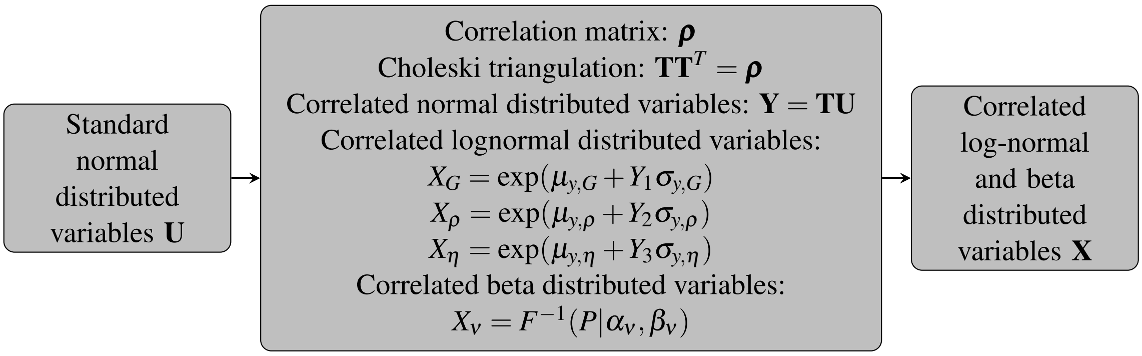

Fig. 3.13: Transformation from ucorrelated to correlated stochastic variables, [Damgaard et al., 2015].

The transformation described in Figure 3.13 can only be applied to standard normal distributed variables, therefore the first step would be to generate a set of random variables which are normal distributed. Randomization is applied separately to each parameter, depending on the parameter of interest whose influence is to be studied i.e. if the influence of variation of the shear modulus is to be studied then only that parameter is randomized, and so on. These stochastic variables are not correlated, therefore in order to transform them to correlated variables, the next step would be to introduce a correlation matrix. The correlation matrix is assumed based on engineering judgement and is given by:

$$\boldsymbol{\rho} = \begin{array}{cc} \begin{array}{cccc} \mu_G & \mu_\rho & \mu_\eta & \mu_\nu \end{array} & \\ \begin{bmatrix} 1.0 & 0.8 & -0.5 & 0.0 \\ 0.8 & 1.0 & -0.5 & 0.5 \\ -0.5 & -0.5 & 1.0 & 0.0 \\ 0.0 & 0.5 & 0.0 & 1.0 \end{bmatrix} & \begin{array}{c} \mu_G \\ \mu_\rho \\ \mu_\eta \\ \mu_\nu \end{array} \end{array} \tag{3.19}$$

If the uncorrelated variables are defined by $\mathbf{U}$, the linear transformation to a new set of correlated variables $\mathbf{Y}$ is done using the Choleski triangulation:

$$\mathbf{Y} = \mathbf{TU} \tag{3.20}$$

$$\mathbf{TT}^T = \boldsymbol{\rho} \tag{3.21}$$

where **T** is a lower triangular matrix. Here it should be mentioned that the randomized variable must always be the leading variable when applying the Choleski triangulation. The final set of values which are correlated, are obtained by converting the random normal distributed set **Y** to log-normal distributed set **X**, more specifically for G, ρ and η while the Poisson's ratio is converted to Beta distributed. They take the following form:

$$X_i = \exp(\mu_y + Y_i \sigma_y) \qquad \text{for} \qquad i = 1,2,3 \tag{3.22}$$

$$X_i = F^{-1}(P|\alpha,\beta) \qquad \text{for} \qquad i = 4 \tag{3.23}$$

where

P	Normal cumulative distribution function
α,β	Beta distribution parameters

The above methodology is applied for the randomization of each parameter one at a time with different coefficient of variations and the set of realizations obtained after each case will be used to find the influence in variation in the frequency response function of each material parameter. This is described in more details in Section 4.3.

3.5.2 Characteristic values for shear modulus

The shear modulus varies for different types of soil, and also for each soil a wide range of values exist. Since the shear modulus is believed to have the highest influence on the response, its wide range should be narrowed down into more specific values. In this case, dry sand is chosen for further analysis and as an input to the model. Since the stiffness of the soil is not predefined, an estimation of it should be made. In order to do so, the shear modulus is found using the relation in Equation 3.24, which is based on Equation 2.15, for known values of the shear wave velocity which can bee seen in Table 2.1.

$$G = \rho \cdot c_S^2 \tag{3.24}$$

The strength of the sand can also vary greatly depending on the type of soil deposition of formation. Therefore, in order to cover this uncertainties the shear modulus, mass density and the shear wave velocity will be treated as random variables. First, by knowing the range of the shear wave velocity for dry sand, three mean values are assumed μ_{c_S} based on engineering judgement, each of them representing a specific strength of sand. More specifically soft sand, medium sand and hard sand. The same is applied to the mass density and the shear modulus is then calculated from Equation 3.24. The mean values for each of the variables is accumulated in Table 3.6.

Tab. 3.6: Mean values of soil properties for soft, medium and hard sand.

	μ_{c_S}[m/s]	μ_ρ[kg/m^3]		μ_G[MPa]
Soft sand	60	1700	$\rightarrow$	6.12
Medium sand	110	1900	$\rightarrow$	22.99
Hard sand	170	2100	$\rightarrow$	60.69

For all three cases, the shear modulus and the density are treated as log-normal distributed stochastic variables since it provides only positive values and eliminates any possibility of non sensical negative values which can never be attributed to the material strengths. A disadvantage of using the log-normal distribution for strength variables is that it may sometimes lead to non-conservative predictions of strengths in the lower part of the distribution, [Det Norske Veritas, 2012]. The two variables are assumed correlated based on the correlation matrix discussed in Section 3.5, and for each set a number of realization is generated. A coefficient of variation of $CoV_G = 20\,\%$ and $CoV_\rho = 5\,\%$ is assumed for the shear modulus and density, respectively. A log-normal distribution is fitted to the realizations obtained for the shear modulus and the mass density while the distribution of the shear wave velocity is found by back calculation of c_S from Equation 3.24. The shear wave velocity will follow a distribution which is close to log-normal, see Figure A.2. The distributions of the shear modulus for soft, medium and hard sand are plotted in Figure 3.14, while the distributions of the mass density can be seen in Figure A.1.

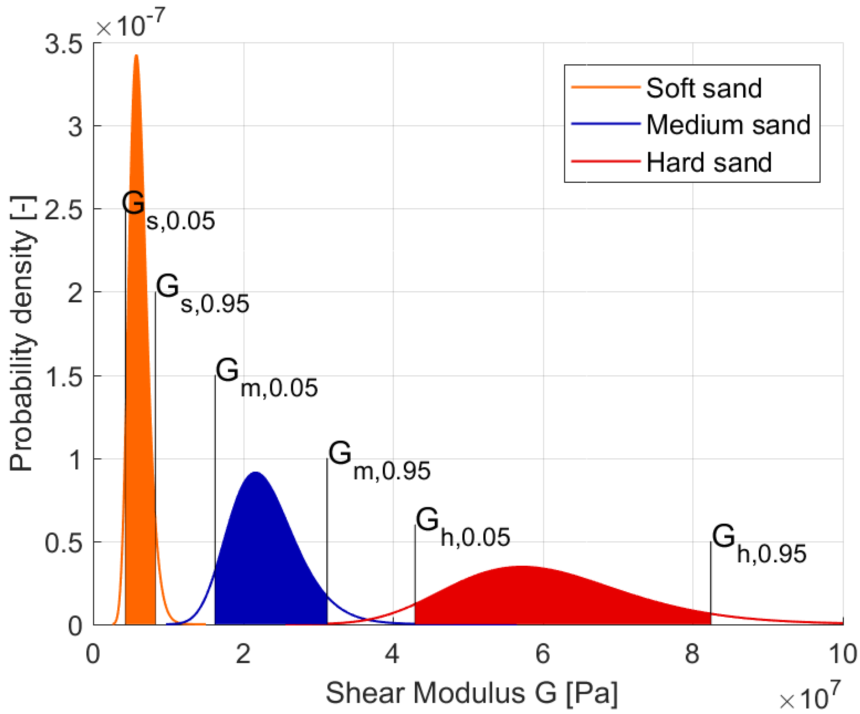

Fig. 3.14: Distribution functions of shear modulus for soft, medium and hard sand.

The 5 % and 95 % quantiles of the shear modulus for soft, medium and hard sand obtained from the distributions are accumulated in Table 3.7.

Tab. 3.7: Characteristics values for the shear modulus.

	Dry Sand		
	Soft	Medium	Hard
$G_{0.05}$ [MPa]	4.33	16.27	42.95
G_{mean} [MPa]	6.11	22.98	60.65
$G_{0.95}$ [MPa]	8.31	31.21	82.39

These characteristics values of the shear modulus obtained for the different kinds of sand will be used as a reference for any analysis performed in the report.

3.5.3 Comparison between medium sand and hard sand

The normalized plots give a good idea of the soil response regardless the load, radius, shear modulus and frequency. Nevertheless, it is also interesting to know the corresponding frequencies ranges where the response shows important changes.

For this reasons, two different sand's response have been illustrated, medium sand and hard sand. The foundation radius considered is $R = 1\,\text{m}$. The soil parameters for both sands are taken deterministic and they are based on the ranges as shown in Table 3.1 by considering that they can be correlated. The values of the shear modulus are chosen as the 5 % and 95 % quantiles for medium and hard sand respectively. Even though those values are calculated on a stochastic process, they are considered as deterministic in this analysis. Table 3.8 shows the values for both medium and hard sand.

Tab. 3.8: Soil parameters.

Soil Parameters	Medium Sand	Hard Sand
ν [-]	0.25	0.25
η [-]	0.04	0.02
ρ [kg/m^3]	1900	2100

These values are used to find the response at a distance of 10 m from the source, see Figure 3.15.

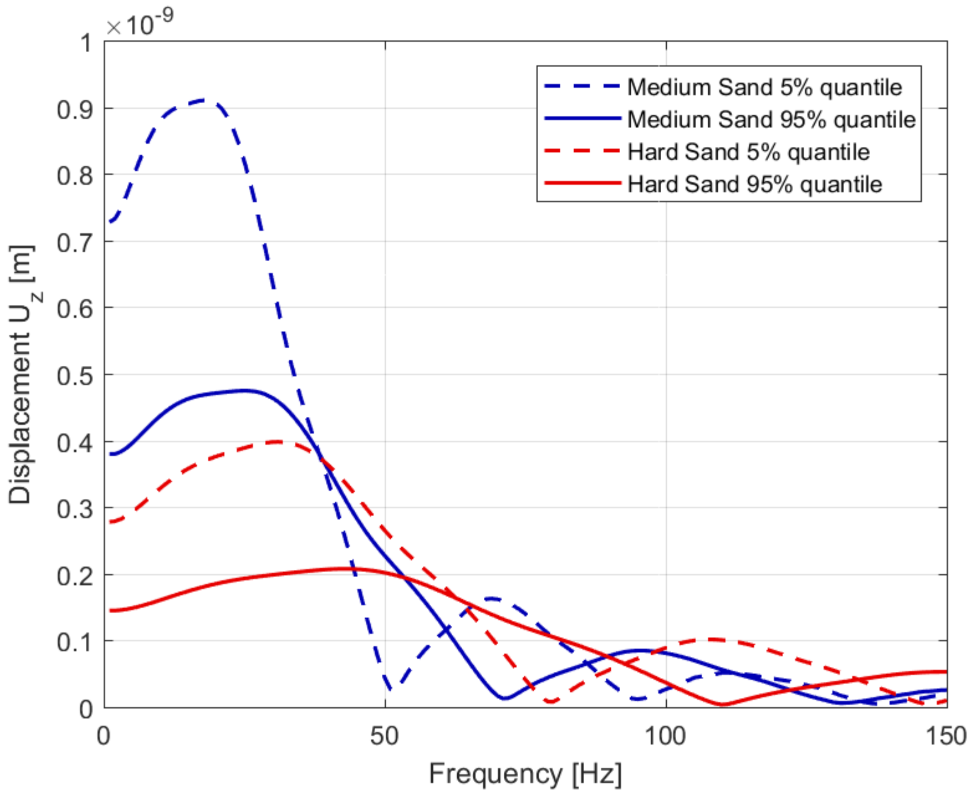

Fig. 3.15: Comparison of medium sand and hard sand

Figure 3.15 shows how the response for different materials is essentially following the same shape as the *normalized response plot*. For medium sand it can be see that the response is the same shape just that it has been elongated. Also the change in the Poisson's ratio affects the local peaks in the response.

3.6 Influence of foundation profiles for load application in the response

When applying the load at either the rigid or flexible foundation the geometrical properties must be defined. In this computational model, rectangular or cylindrical foundations can be modelled. Here cylinder has been considered for both foundations types and the radius of it is given as R.

In order to show the differences when applying the load on a rigid foundation or on a flexible foundation the responses of each of the foundations have been depicted for the same material in three different observation points, see Figure 3.16. The used soil parameters correspond to the reference case given in Table 3.2. Notice that the load is applied on the vertical direction and the response corresponds also to the vertical component.

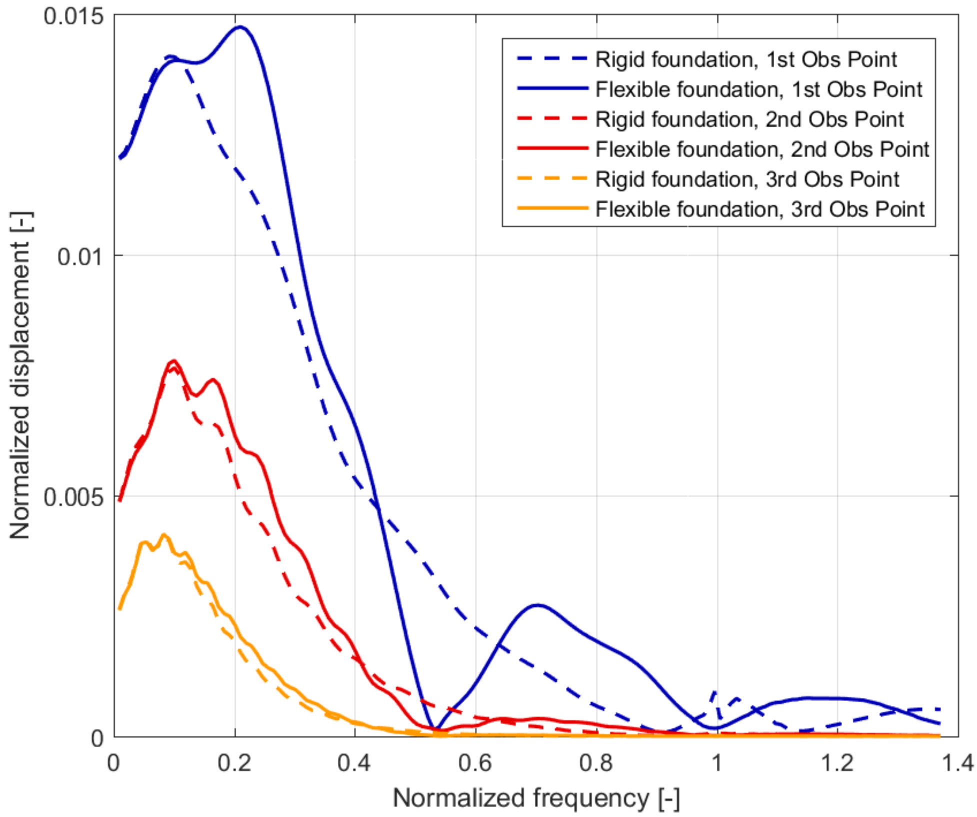

Fig. 3.16: Response of model on different type of load application in frequency domain.

Two main observations can be made out of the chart. First, the response for flexible and rigid foundations matches very well for low non-dimensional frequencies, before they reach the peak. That is, when the foundation's radius is very small in comparison with the wavelength the influence of the foundation type is negligible.

Second, the response at far observations points match better than those closer to the source. When looking at the orange lines which correspond to $50 \cdot R$ distance it can be seen that there is almost a perfect match while for the blue line, observation point at $10 \cdot R$, a notable difference is shown in the shape of the response.

Overall, for rigid foundation, the response has a smoother shape that decreases gradually while for the flexible foundation some fluctuations occur that lead to some local peaks. This local peaks are due to the stress distribution beneath the foundation. For static case some differences can be seen, see Figure 3.17 for rigid foundation and Figure 3.18 for flexible foundation.

For the flexible foundation the stress distribution beneath is uniform while for the rigid foundation it is parabolic. For the dynamic case, these distributions will change but they will still be different. This is the reason why the response look different for rigid and flexible.

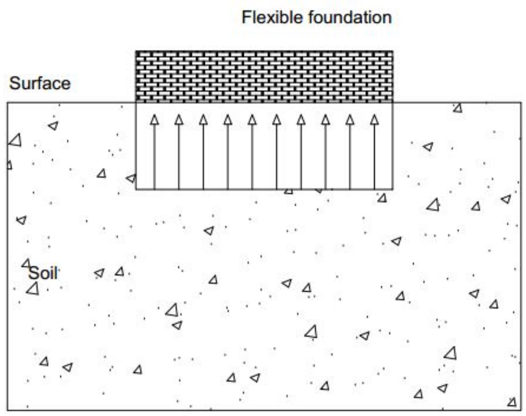

Fig. 3.17: Stress distribution in flexible foundation.

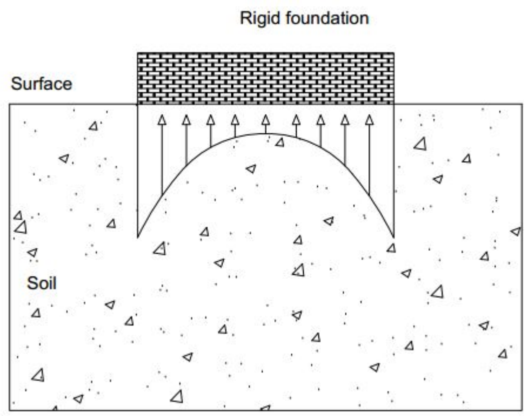

Fig. 3.18: Stress distribution in rigid foundation.

For further study of other parameters influence and moreover in the modelling of real case study of railway site, only flexible foundation is used for the reason of saving computation time.

3.7 Development of displacements over the distance

The development of vertical displacements over the distance in the model is evaluated by applying the reference soil parameter from Table 3.2. Here, both the vertical and horizontal axis are normalized. The distance has been normalized regarding the foundation's radius R. That leads to the normalized distance r', see Equation 3.25. Notice that a flexible foundation has been used in this analysis.

$$r' = \frac{r}{R} \tag{3.25}$$

where

r'	Normalized distance [-]
r	Distance [m]

A range of normalized frequencies has been plotted, $f' = 0.1$, $f' = 0.3$, $f' = 0.5$, $f' = 1$, see Figure 3.19. There it can be seen that the ground response decreases gradually with the normalized distance. This means that for large distances in comparison with the foundation radius, the response dies out. This is caused by dissipation given by geometrical and material damping. On the other hand, it must be mentioned that here dispersion does not occur since it is half-space and the body and Rayleigh waves are non dispersive.

On the other hand, for higher frequencies, lower response is observed. This is because when there are small wavelengths in the system in comparison with the radius and observation points location, that is high frequencies waves, then more material dissipation occurs since the energy loss in the waves occurs for each oscillation of the wave. This is studied in more detail at the end of the section.

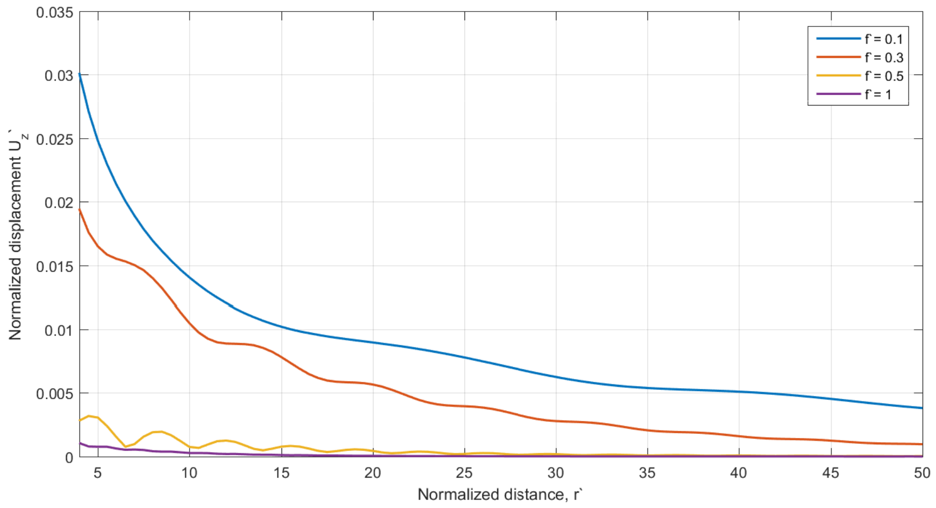

Fig. 3.19: Response of model along the distance.

For better overview, and better representation of the distance and frequency influence on the displacement, all three variables are normalised and plotted in a 3D plot, see Figure 3.20.

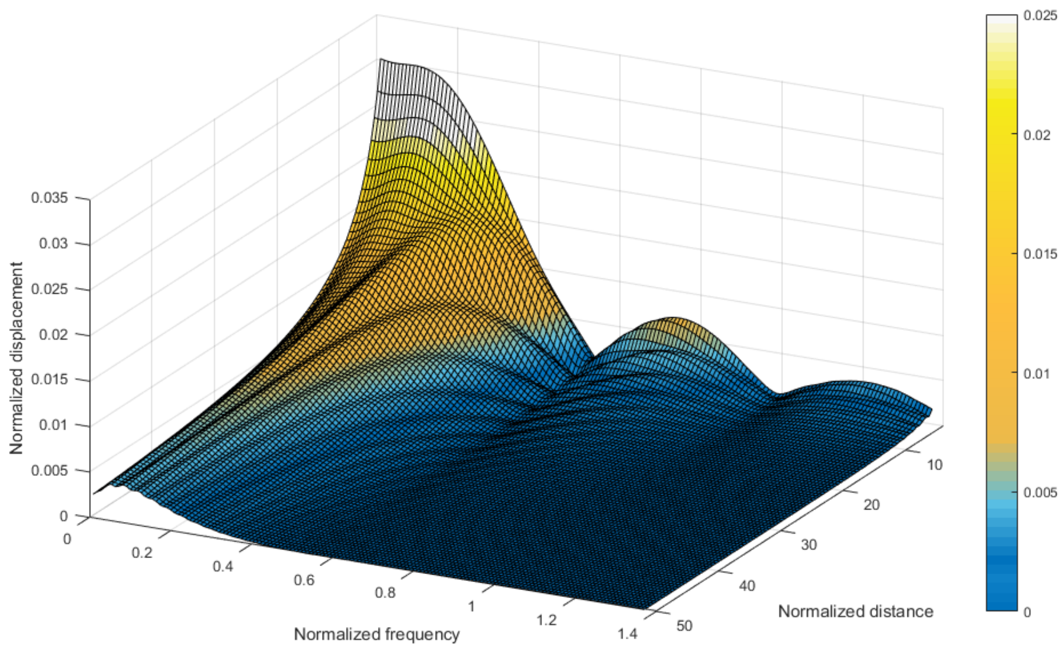

Fig. 3.20: Response of model for different non dimensional frequencies and locations.

It is obvious that highest response is achieved at lower frequencies, where the waves have bigger amplitude, at a distance close to the source. Moreover it can be seen that at certain normalised frequencies, i.e. 0.6 Hz and 1.2 Hz, the response dies out. This is due to above mentioned fact of the load application. Most interesting behaviour is the creation of numerous "waves" which are to be found as highly sensitive to Poisson's ratio changes.

Geometrical and material damping in the model

It is known that the geometrical damping is predominant over material damping at near field while the opposite occurs at far filed. The damping in the computational model includes both geometrical and material damping when plotting the response in normalized frequency, that is, for a given frequency and a given time.

In order to quantify the geometrical and material damping over the distance, first the response where only geometrical damping is considered. This is calculated analytically based on the distance from the source and the amplitude of the wave, see Equation 3.26. Here only the geometrical damping of the surface waves is considered.

$$Displacement = \frac{1}{\sqrt{r}} \cdot Amplitude \tag{3.26}$$

The response obtained from the model is plotted along with the calculated response for only geometrical damping. It should be mentioned that in the model there is also the effect of the body waves which dissipate faster, but since we are measuring in the surface we assume that the Rayleigh waves are the most important.

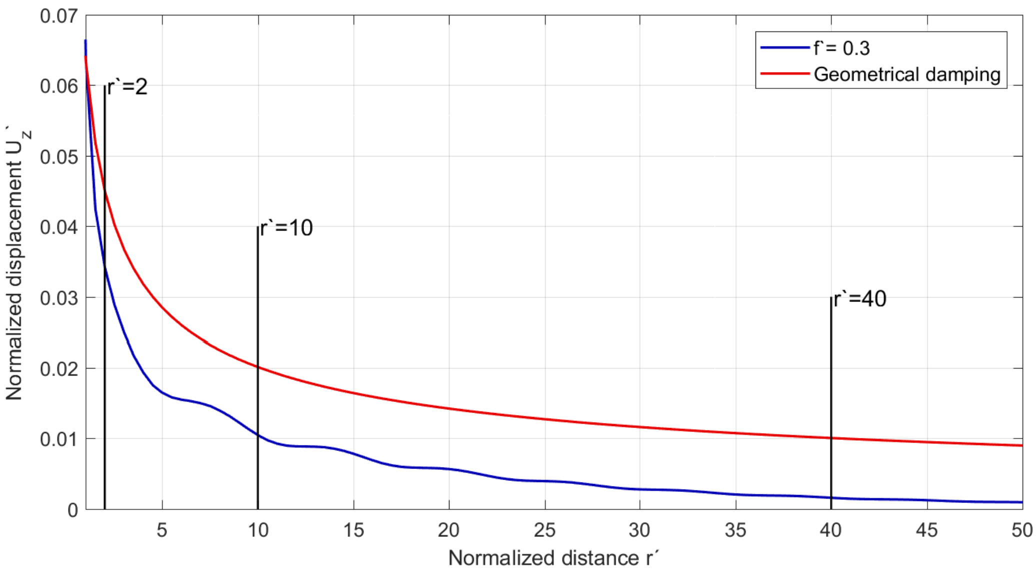

Fig. 3.21: Lost of amplitude due to geometrical damping and model response.

Figure 3.21 shows the normalized response obtained from the model in blue plotted along with the response for only geometrical damping in red. It can be seen that at close distances the influence of the geometrical damping is higher while as we move further the decrease in the response of the model is quite noticeable, which is attributed to the material damping i.e the difference between these two responses

will corresponds to the material damping. As expected, the closer to the source the highest the influence of geometrical damping and further away the highest the influence of material damping.
Three different points have been chosen along the distance and the percentage of material damping in the response has been calculated, see Table 3.9.

Tab. 3.9: Material damping for three locations.

Normalised distance	Percentage of material damping in the response
$r' = 2$ [-]	24.2%
$r' = 10$ [-]	48.2%
$r' = 40$ [-]	84.2%

3.8 Summary

This chapter concerns an analysis and description of the computational model. It can be divided in five main parts, introduction to the formulation for layered soil, verification of the waves type propagation in the media, deterministic analysis of soil parameters, influence of foundation types and development of displacement over the distance.

- **Formulation for layered half space**. Here the basic ideas and formulation for modelling a layered half-space are presented. The basics for the impedance matrix applied in the code as well as the concepts of the semi analytic approach applied in the model are given.

- **Verification of waves types propagating in the media**. Propagation of waves in the surface and inside the idea was investigated where the load was applied in different directions and the displacement also measured for different components.
  - For load applied in x-direction and response also measured in x, SH-waves had the highest influence.
  - For load applied in y-direction and response also measured in y, P- and Rayleigh waves had the highest influence.
  - For load applied in z-direction and response also measured in z, the Rayleigh wave had the highest influence.

- **Material uncertainties** due to limited data and spatial variability were covered by performing a probabilistic analysis where the material were considered to be correlated. Furthermore, the characteristic values of shear modulus for soft, medium and hard sand were calculated based on table values of the shear wave velocity.

- **Soil parameters analysis**. The response given by the model is dependent of the foundation ratio, applied load and soil parameters. Several variables influencing the model have been normalised so the response of the model became linearly dependent on them and therefore only influence of Poisson's ratio and damping ratio had to be analysed.
  - **Poisson's ratio** was found to induce a change of shape in the response for high values of ν, corresponding to a saturated soil.

  - High **loss factor** will increase the response considerably especially at high frequencies mainly due to material damping.

- **Influence of foundation type in the response**. The selection of the foundation type has important influence in the response of the model. Here it has been shown how much the response can vary from one foundation to the other. The main observation come when taking a look at far field where the response for rigid or flexible foundation matches pretty well.

- **Development of displacements over the distance**. In this section the response of the model is evaluated along the distance. As expected the response decreases as the distance increase due to the energy loss and dispersion. Another observation is done for changing the frequencies of the waves. When the frequency is higher the dissipation is higher and thus the response decreases faster.

4 Soil parameters study for layered media

In this chapter the influence of the material properties in a layered media is studied. Two different approaches are considered for this analysis: a deterministic approach and a probabilistic approach.

4.1 Introduction

In layered media, the number of parameters used to describe the soil will change depending on the number of layers. In this case a new parameter is introduced, which is the layer depth, h, and is believed to have a considerable influence in the final response. The situation therefore becomes more complex than for half-space and the parameter study cannot be performed in the same way. This means that normalization cannot be applied in layered media since now the waves will be travelling with different phase velocities for different layers. For simplification, only one layer overlaying a half-space will be considered for the sensitivity analysis and each parameter will be studied separately. The basis of this analysis lies in the impedance mismatch of the two layers, as explained in Section 2.4. Two different approaches are applied to study the sensitivity of the parameters, including a deterministic approach and probabilistic approach. For all cases, the load is applied vertically and only the displacement in the vertical direction in considered. An illustration of the model considered in this analysis is shown in Figure 4.1.

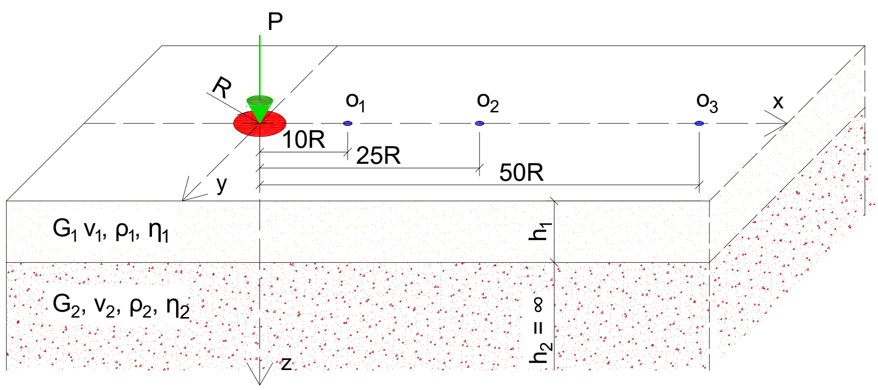

Fig. 4.1: Layered media with three observation points away from the source.

4.2 Deterministic soil parameter study

By using the deterministic approach, the sensitivity of the shear modulus, material density, Poisson's ratio, loss factor and layer depth on the response will be investigated. Each of the before mentioned parameters is studied separately by assigning different values to it while in the meantime keeping everything else constant. The parameters are varied for two cases, once for the top layer, and the second time by changing the parameters in the bottom layer. The reason behind this approach is attributed to the fact that changing one parameter will change the impedance mismatch of the two layers therefore also resulting in a different response. In comparison to having only a half-space the impedance mismatch is always equal to one while for a layered media that will differ. Since the response is measured at three observation points placed on the surface, it is believed that the properties of the top layer will have the biggest influence in the dynamic amplification, therefore more attention will be focused on studying changes in the top layer. Only sand, starting from soft to hard sand as described in the previous chapter, is studied in this deterministic analysis.

4.2.1 Influence of the shear modulus in FRF

The shear modulus is considered to have the biggest influence in the final response. The reason for this is that the shear modulus can vary greatly depending on the type of material used and is the main parameter which defines the strength of the soil. Since a layered soil is considered, that leads to two different shear modulus to describe the media, G_1 for the top layer and G_2 for the underlying half-space, respectively. The influence of each modulus is studied separately, first by giving different deterministic values to the shear modulus of the top layer while keeping all other properties constant, and second by assigning different deterministic values to the shear modulus of the half-space and every other parameter is constant. The values assigned to the shear modulus are the ones shown in Table 3.7, which even though they are obtained based on a probabilistic approach, they will be considered as deterministic during this analysis. For the remaining parameters the values are assigned based on engineering judgement.

A response line representing a half-space where all material properties are the same is taken as the reference line for comparison, see Table 4.1. The 95 % of the shear modulus for medium sand is chosen as the starting value. This is considered based on the fact the $G_{0.95}$ for medium sand is somehow in the middle of the values that are available and more accurate analysis can be performed.

Tab. 4.1: Soil properties of the reference line.

	Shear Modulus G [MPa]	Poisson's ratio ν	Density ρ [kg/m^3]	Loss factor η	Depth h [m]
Top layer	31.21	0.3	2000	0.04	4
Half-space	31.21	0.3	2000	0.04	∞

To analyse the influence of the shear modulus in the top layer, two values smaller than the reference value are assigned to the shear modulus which will correspond to the case where the top layer is softer than the half-space. In addition to these, higher values are also given to the shear modulus which will lead to a stiffer top layer of underlying the half-space. The values of the shear modulus considered during this analysis are presented in Table 4.2. All the values correspond to different strengths of sand as discussed in Section 3.5.2.

Tab. 4.2: Shear modulus for the case of soft and stiff top layer overlaying a half-space.

	Soft top	Stiff top
	G [MPa]	
Top layer	8.31	60.65
	16.27	82.39
Half-space	31.21	31.21

Here it should be mentioned that $G_{0.05}$ for soft sand is not considered because the top layer becomes too soft and the analysis cannot be performed. The response from the two cases is calculated for three distances away form the source, as specified previously and the results are shown in Figure 4.2.

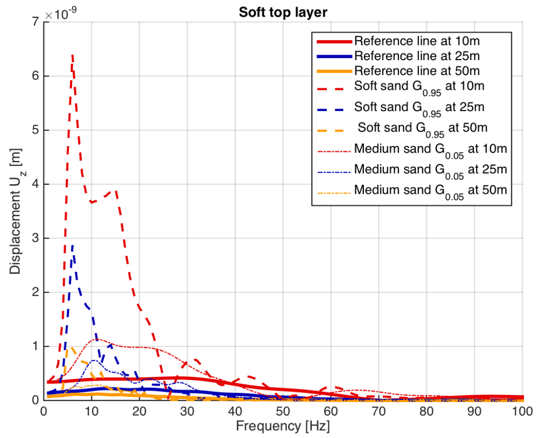

(a) Response of the layered media for soft top layer.

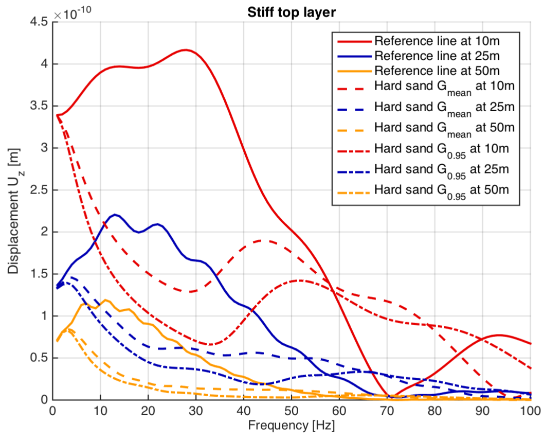

(b) Response of the layered media for stiff top layer.

Fig. 4.2: Influence of the shear modulus in the top layer.

One can clearly notice from Figure 4.2a that the response increases greatly when the stiffness of the top layer is very small in relation to the half-space, which corresponds to the mean value of the shear modulus for soft sand. This can be due to the lower impedance in top layer, leading to higher reflection of waves, thus higher displacement. On the other side, the response reduces significantly over distance which is as expected. Furthermore, for the case of the soft sand, the resonance frequency occurs at around 6 Hz while for the 5 % characteristic value of the medium sand the resonance frequency occurs at 11 Hz. This means that by increasing the stiffness of the top layer, the response at a certain observation point will be affected at higher frequencies.
On the other hand, Figure B.1b, shows the inverse relationship. The stiff layer on top decreases drastically the displacement and also decreasing even further with distance. This corresponds to the case where the impedance mismatch goes towards zero and the amount of the transmitted energy in the bottommost half-space will decrease by increasing the stiffness. Only one peak is seen to occur at high frequencies and at a distance of 10 m from the source while at greater distances this behaviour is not associated.

The influence of the shear modulus is also evaluated in the bottommost half-space, see Figure B.1. One can see from the results that the behaviour is as expected, meaning that by making the half-space stiffer than the top layer, the displacement increases and that can be due to the fact that the mechanical impedance will be higher in the bottom therefore leading to a impedance mismatch greater than 1 which represents the case where the energy of the waves will be reflected to the top layer and less energy will be transmitted. The amount of the reflected energy will depend on how much the impedance mismatch differs from 1 i.e. the stiffer the bottom layer the higher the reflected energy.

The same analysis is performed by varying the shear modulus in the bottommost half-space see Figure B.1. More or less the same behaviour is observed by changing the shear modulus, with the only difference being that the amplitude of the frequency response function is smaller than the one seen in Figure 4.2. This is as expected since the observation points are placed in the surface therefore the top layer is expected to be the most influential.

4.2.2 Influence of the material density in FRF

The mass density of the material is known to have little variation in soils, as shown in Table 3.1, and only a small change in magnitude can be considered therefore also its influence in the response would consecutively be small. Nevertheless, a study of its sensitivity is performed in order to prove and show that assumption and have a better visual understanding of its influence. The same procedure as for the sensitivity of the shear modulus is applied, first by varying the density in the top layer while keeping everything else constant, for the case when the top layer is softer than the underlying half-space, and for the opposite scenario when the top layer is stiffer. Comparison is made by considering a reference observation for the two cases. The respective material properties used in each analysis are accumulated in Table 4.3.

Tab. 4.3: Soil properties for reference observations.

	Shear Modulus G [MPa]	Poisson's ratio ν [−]	Density ρ [kg/m^3]	Loss factor η	Depth h [m]
Soft top layer	16.27	0.3	2000	0.04	4
Stiff top layer	82.39	0.3	2000	0.04	4
Half-space	31.21	0.3	2000	0.04	∞

For each analysis, deterministic values for the mass density are assigned which are lower and higher than the reference value, more specifically $\rho = 1700\,\mathrm{kg/m^3}$ and $\rho = 2300\,\mathrm{kg/m^3}$. In the first case the media consist of a top layer with $G_{0.05}$ for medium sand while in the second case a top layer of $G_{0.95}$ for hard sand, both overlaying the same half-space as before. The influence of the density is found for three different distances from the source, as shown in Figure 4.3.

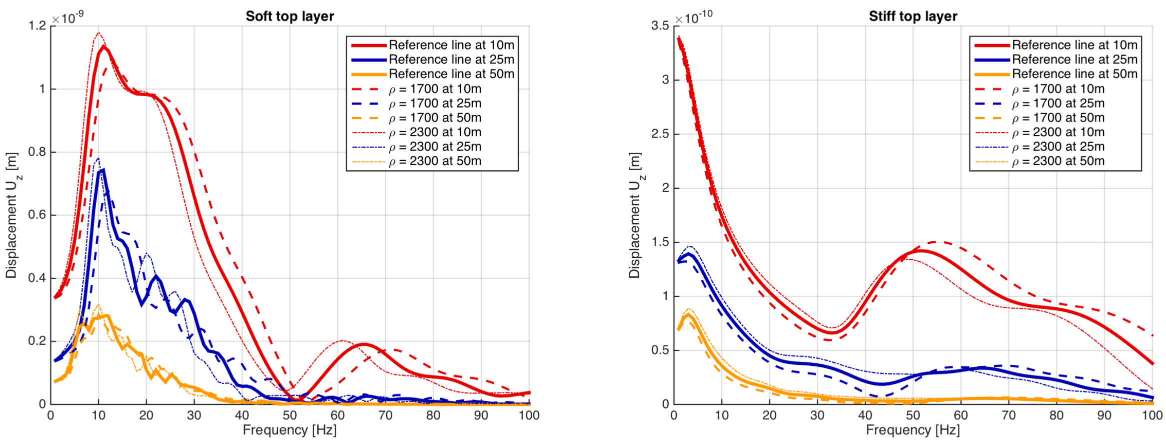

(a) Response of the layered media for soft top layer. (b) Response of the layered media for stiff top layer.

Fig. 4.3: Sensitivity of the material mass density in the top layer.

As expected, the influence of the mass density is very small for all analysed cases. There is only a small change in amplitude of the response, and this change reduces considerably with distance. Another observation is the fact that the response shifts a little when the density varies with the resonance frequency also changing slightly. An explanation for this can be the fact that by increasing the mass density of the material, lower eigenmodes may be effected which can also lead to higher displacements.

The same analysis is performed by varying the density in the half-space underlying a constant top layer, for softer and stiffer half-space. It is found that the influence of the mass density in the half-space is even smaller than before therefore it is regarded as insignificant and is not included in this section. For results, see Figure B.2.

4.2.3 Influence of the loss factor in FRF

In order to look at the effect of damping in a layered media, the loss factor is changed in the top layer while all other parameters are kept constant. For the sensitivity analysis, the same observations as described in Table 4.3 are taken as references while the loss factor is varied with lower and higher values than the reference one, more specifically for $\eta = 0.01$ and $\eta = 0.08$, respectively. The results obtained for all distance are shown in Figure 4.4.

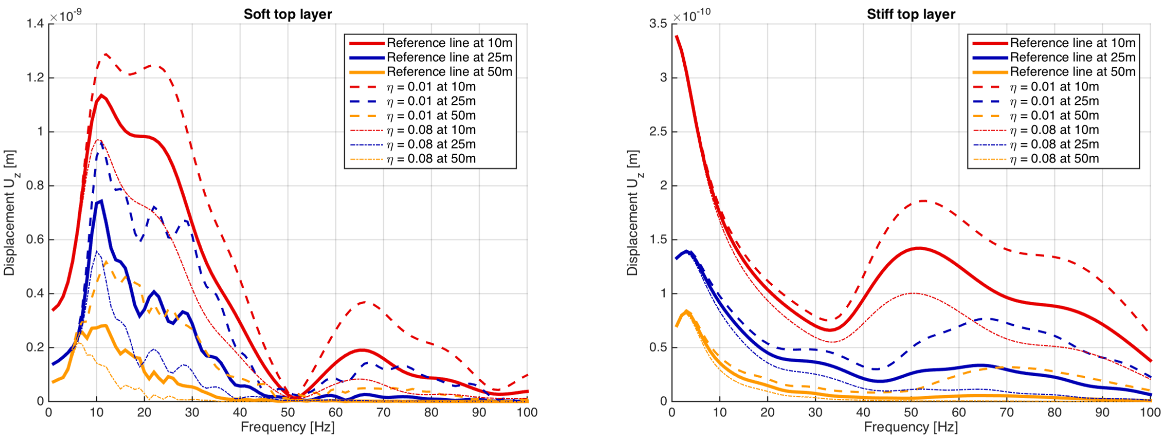

(a) Response of the layered media for soft top layer.

(b) Response of the layered media for stiff top layer.

Fig. 4.4: Sensitivity of the loss factor in the top layer.

One can see that by changing the loss factor the response changes significantly. This phenomenon is better observed in Figure 4.4a when a soft layer is placed on top of a stiff half-space. When the loss factor is decreased by 75 %, an increase of around 13 % occurs for the maximum response at a distance of 10 m from the source, while at 50 m away this increase goes up to 74 %. The opposite behaviour is observed when loss factor is increased by 100 %, leading to a decrease of the maximum response by 15 % at 10 m distance and around 52 % at the furthest observation point. More or less the same behaviour is also noted at higher frequencies. Furthermore, it can be said that damping only influences the magnitude of the response, without changes its shape.
The results look as expected, since the waves are attenuated when spread over large volumes due to the effect of the geometrical damping and material damping at lower frequencies. While at higher frequencies the effect of material damping is more profound since higher frequencies are related to more frequent oscillations and therefore more loss of energy. When a stiffer top layer is considered, the

influence of the loss factor is more significant at higher frequencies, which is due to the material damping while the geometrical damping is very small.

The loss factor is also varied in the bottom half-space and its influence is found to be almost insignificant, see Figure B.3. Only at low frequencies a small change of response happens while at higher frequencies there is almost no variation, hand that is due to the fact that high frequency waves have short wavelength therefore they will only be travelling at the the top layer and not be affected much by the bottommost half-space.

4.2.4 Influence of Poisson's ratio in FRF

As shown in Example 2.3.1, the Poisson's ratio leads to an increase in the speed of P-wave, especially at high values of Poisson's ratio where the increase is significant in comparison to the S-wave and Rayleigh wave. Its influence in the response is regarded important, as was shown in the case of the half-space. In order to find out how it will effect the layered media, the Poisson's ratio in the top layer is changed for the cases of soft sand over medium sand, and hard sand overlaying a half-space of medium strength sand. The values for the Poisson's ratio considered in this analysis include $\nu = 0.2$ and $\nu = 0.49$, with the first one corresponding to a drained material while the second describes an undrained soil. The reference material properties of the response used in the analysis are the same as the ones used to find the influence of the mass density, see Table 4.3 by assuming an almost drained behaviour. Changes in the response for all three observation points can be seen in Figure 4.5.

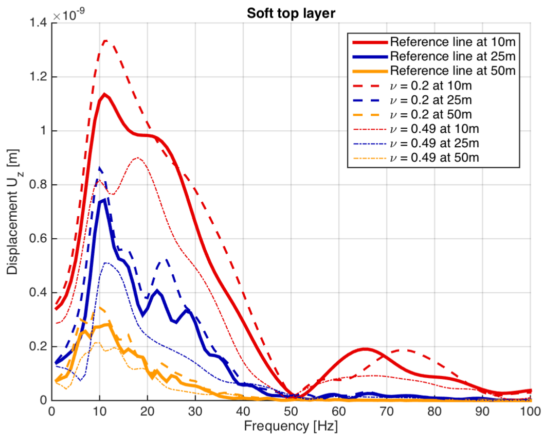

(a) Response of the layered media for soft top layer.

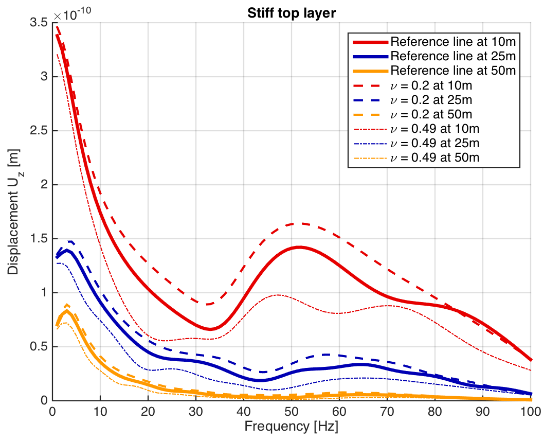

(b) Response of the layered media for stiff top layer.

Fig. 4.5: Sensitivity of the Poisson's ratio in the top layer.

The same characteristics of the influence of Poisson's ratio are observed for both cases where a decrease of the Poisson's ratio leads to an increase of the magnitude of the response since it will lead to an decrease of the elastic modulus, according to the Lame constants and vice versa. More precisely a decrease of the Poisson's ratio by 33 % increases the maximum response by 17.5 % calculated at a distance of 10 m where the variation since to be the highest. On the other side, a 63 % increase in the Poisson's ratio reduces the magnitude of the maximum displacement by around 30 % at 10 m from the source. It is also noted that for $\nu = 0.49$ the shape of the response changes considerably for both cases, which can be due to the fact that the P-wave speed goes towards infinity for saturated soils.

The same behaviour is observed when Poisson's ratio is varied in the bottom half-space, with only a smaller change in the magnitude of the displacement in comparison to the top layer, see Figure B.4.

4.2.5 Depth of the top layer

The depth of the layer is also another factor that has an important influence in the dynamic amplification of the response. Since the measurements are considered at the surface, the Rayleigh wave is the principal wave that creates displacements. Almost all the energy of Rayleigh wave is concentrated in a depth two times the length of the Rayleigh wave, while if the depth becomes larger than twice the wavelength then the Rayleigh wave will not interact with the bottom half-space anymore, [Holm and Riis, 2014].

For the sensitivity of the layer depth, two cases are considered in respect to the reference observations as shown in Table 4.3. First the depth is reduced to 2 m and the response is calculated for all distances, while for second case the depth is increased to 7 m. The response obtained for all simulations is shown in Figure 4.6.

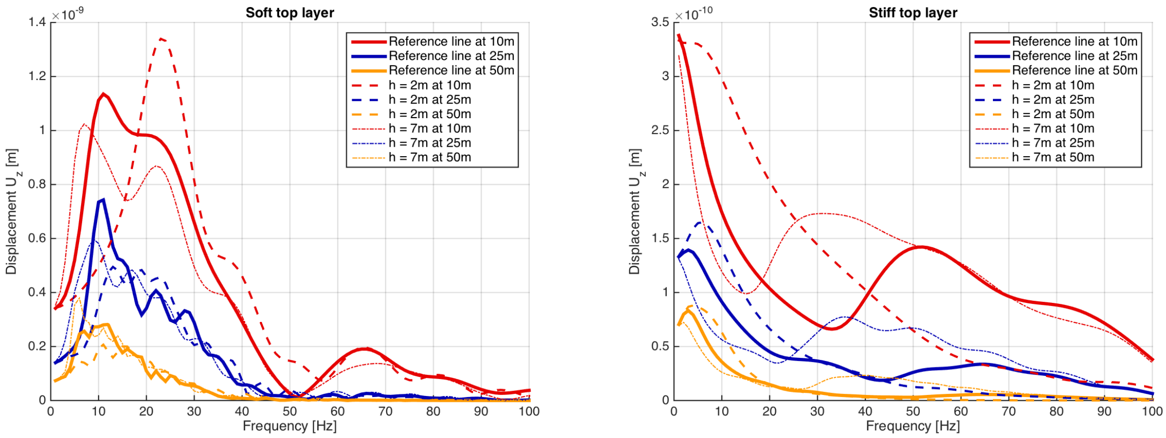

(a) Response of the layered media for soft top layer.

(b) Response of the layered media for stiff top layer.

Fig. 4.6: Influence of the top layer depth for varying strength of the top layer.

It is seen that by changing the depth of the top layer, the response changes drastically. When the top layer is softer than the underlying half-space, the maximum magnitude of the displacement decreases by decreasing the layer depth and the other way around when the depth increases. In the case of a stiffer top layer, the situation changes and it seen that the response varies a lot when the depth increases while for lower depth it seems like the response follows a more linear curve. A common distinction for all cases is the fact resonance occurs at the frequency where the depth of the layer is almost half the Rayleigh wavelength. Furthermore, by increasing the depth, the resonance frequency shifts towards lower frequencies and this due to the fact that the top layer will be influenced by more waves and wavelengths. The influence of the layer depth will be discussed in more detail from the dispersion curves, see Section 4.4.

As for all other parameters, the influence of the layer depth is found for varying properties of the underlying half-space. Although, it was observed that there is no significant change in the response when the properties of the half-space are changed. For further details see Figure B.5.

4.3 Probabilistic soil parameter study

In addition to the deterministic analysis described in the previous section, a probabilistic analysis will be conducted in this section to find the influence of each parameter in the final response. The material parameters will be assumed as stochastic variables which are related to each other by a correlation matrix as described in Section 3.5, where changing one parameter can also infect changes on the other parameters based on the correlation between them. Each variable is randomized separately while the others are allowed changes only based on the correlation matrix. The process includes generating a reasonable number of realizations to obtain more accurate results. This way the influence of each parameter on the output is studied for different coefficient of variations. The probabilistic analysis accounts for the uncertainties related to the material parameters and the idea behind this approach, is to show how the coefficient of variation in the response will vary over frequency based on the variance of each parameter specified in the input. The response is calculated for all cases at 10 m distance from the source. In comparison to the deterministic approach, this method is regarded somehow as a better representation of the reality since the parameters tend to vary together..

4.3.1 Influence of variation of the shear modulus

The influence of variation of the shear modulus is analysed by randomization of the parameter with normal distributed variables. A mean value of μ_G corresponding to the G_{mean} for hard sand is assigned to the shear modulus with a coefficient of variation that includes 10 %, 20 %, 30 % and 40 %. The methodology applied in this case is the one described in Section 3.5, where the shear modulus is assigned as the leading variable while the density and the loss factor will tend to change based on the correlation matrix. On the other hand, since Poisson's ratio and shear modulus are specified independent of each other there will be no variation of the Poisson's ratio and it will remain constant throughout. 50 realizations have been included for each corresponding case of the coefficient of variation and the results are shown in Figure 4.7.

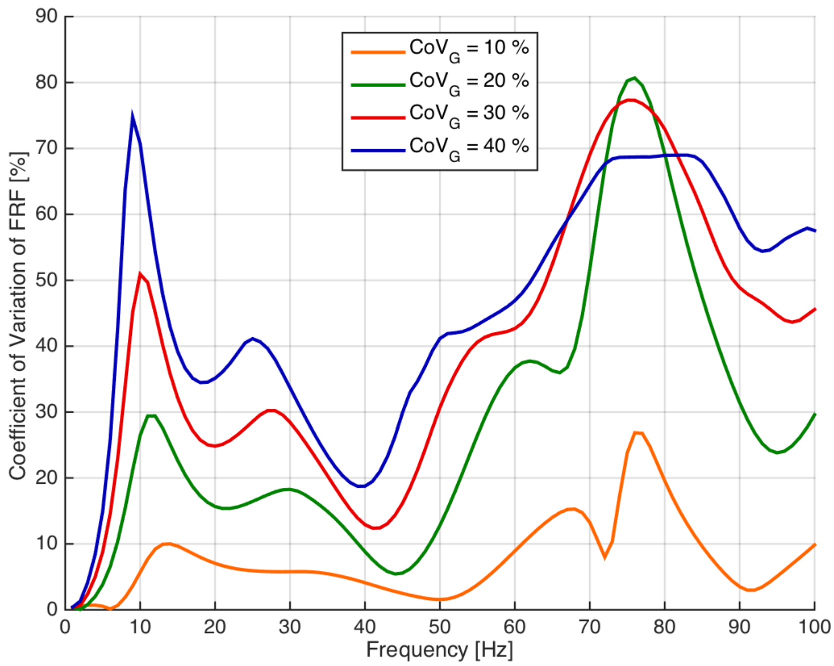

Fig. 4.7: Variation of FRF for randomization of the shear modulus at 10 m distance from the source.

From the above figure it is clearly seen that by increasing the coefficient of variation for the shear modulus, the variation of the response also increases significantly. This looks as expected since having a higher coefficient of variation for the shear modulus its values are spread further from the mean, therefore having a wider range. Also one thing that can be noticed is the fact that at lower frequencies there is a high peak of variation for the response which also correspond approximately at the frequency where resonance occurs and displacement is the highest.

4.3.2 Influence of variation of the mass density

To find the influence of variation of the mass density, the same procedure as for the study of the shear modulus is applied. Although, in this case the mass density is assigned as the leading variable. Randomization of the density is analysed for three different cases with coefficient of variation of 5 %, 10 % and 15 % and 50 realization are included for each. The difference in this analysis is that the density is correlated to all the other materials, so by changing it all other properties will also change accordingly. The results for all the cases are presented in Figure 4.8.

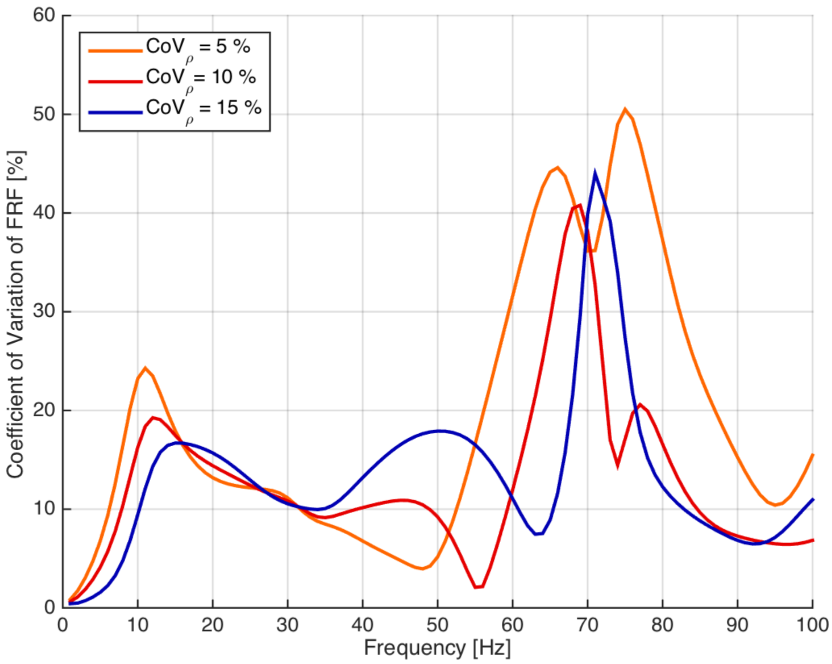

Fig. 4.8: Variation of FRF for randomization of the mass density at 10 m distance from the source.

One can notice that the variation in the response when the density varies, is quite different in comparison to results obtained from the deterministic analysis. Here, a change in density implies higher variations in the frequency response function than it did in the previous analysis. This can be due to the fact that when density changes, all other material parameters change due to the correlation, so the variation is not purely effected from the mass density, which was the case in the deterministic analysis where all other parameters were kept constant. One thing it has in common with the deterministic analysis is the fact the variation in response shifts at lower frequencies during resonance which can be due to an higher density affecting lower eigenmodes.

4.3.3 Influence of variation of the loss factor

Damping in known to have a wide range of values that can be attributed to it, therefore for this analysis coefficient of variations of 20 %, 30 % and 40 % are assigned to it. The loss factor has a negative correlation with the shear modulus and the mass density therefore they will vary in opposite directions while the Poisson's ratio will remain constant throughout. Analysis is performed same way as before and the results obtained are shown in Figure 4.9.

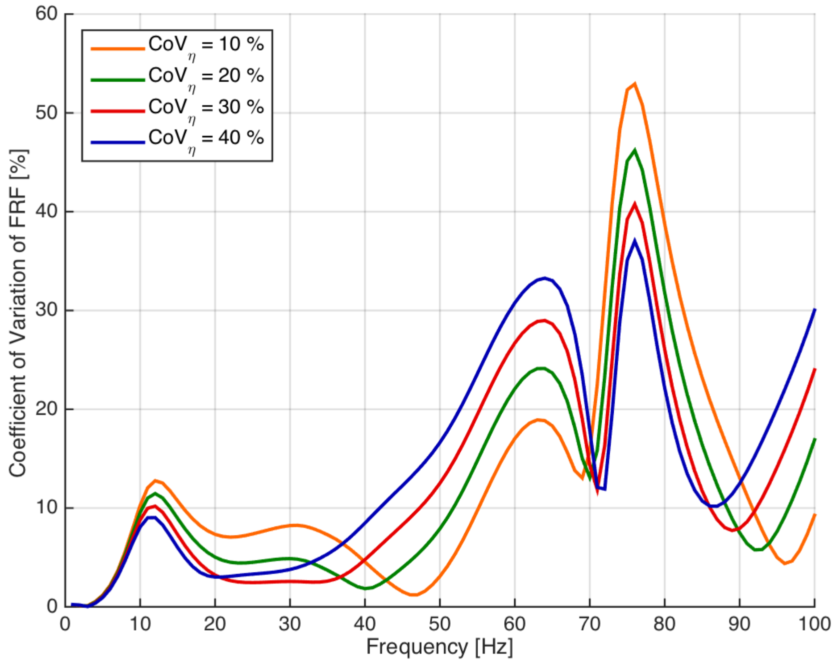

Fig. 4.9: Variation of FRF for randomization of the shear modulus at 10 m distance from the source.

As expected, the influence of the coefficient of variation of the loss factor in the coefficient of variation of the frequency response function is considerably small, with very little variation for the different cases especially at lower frequencies. Its biggest influence is at a frequency range of 40 Hz to 75 Hz while in other positions is almost neglectable which makes perfect sense since damping is known to influence the response at higher frequencies. All in all these results correspond well to the ones obtained from the deterministic analysis.

4.3.4 Influence of variation of Poisson's ratio

Studying the influence of variation of the Poisson's ratio involves the randomization of the parameter for three different occasions with coefficients of variation of 10 %, 15 % and 20 % from mean μ_ν as specified in Section 3.5.1. Variation is limited in this case since Poisson's ratio can only vary in a certain range, see Table 3.1. Based on the correlation matrix, by randomizing ν only the density will change while the shear modulus and loss factor will remain constant all the time. By performing the same procedure as before, the results obtained are shown in Figure 4.10.

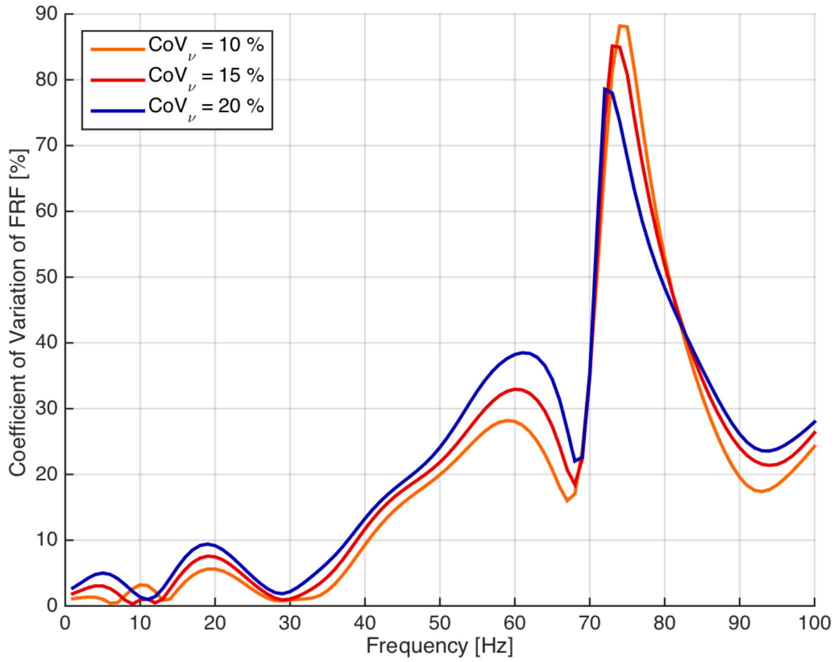

Fig. 4.10: Variation of FRF for randomization of the Poisson's ratio at 10 m distance from the source.

Figure 4.10 shows that randomization of the Poisson's ratio changes the shape of the response completely especially at low frequencies where resonance occur. Although the variation in response over frequency for different coefficients of variation of the ν is very small. This behaviour is typical for the Poisson's ratio and the same was observed during the deterministic analysis of the layered media but also for the case of a half-space.

4.4 Dispersion relation

So far we have discussed about the fact that Rayleigh waves, P- and S- waves, are non-dispersive. But that was the case on a homogeneous half-space. If a layered half-space is considered, then the waves will propagate with different wavenumbers and different wave speeds between the layers. Therefore, depending on the properties of the soil, especially the stiffness and depth of the layer, the response will change considerably. In this section, the influence of these parameters on the response of the soil will be investigated further based on the dispersion relation. These relations will help to describe the dynamic behaviour of a soil deposit and examine weather these behaviour is acceptable. As it was already observed in the previous sections, the influence of the density of the material, Poisson's ratio and loss factor on the final response was very low, therefore those values will be kept constant throughout and the focus will be mainly on the shear modulus and depth of the layer, for different frequencies. The properties of the materials are described in the Table 4.4, where the changing value is the shear modulus.

Tab. 4.4: Soil properties for two different materials considered.

	Shear Modulus G [MPa]	Poisson's ratio ν	Density ρ [kg/m^3]	Loss factor η	Depth h [m]
Material 1	16.27	0.3	2000	0.04	4
Material 2	60.65	0.3	2000	0.04	4
Half-space	31.21	0.3	2000	0.04	∞

In the first case, a single layer with properties of material 1 overlays a homogeneous half space, while in the second model a layer of Material 2 overlays the same half-space. For both cases, the depth of the layer is kept the same. The dispersion relations is shown for observations points placed in the surface. The load is applied vertically and also the displacement is measured in the vertical direction. The results for the two models are presented in Figure 4.11.

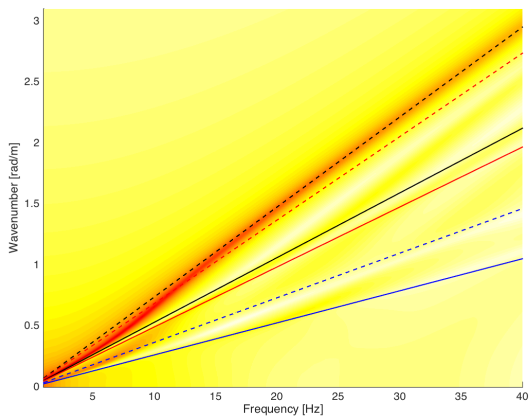

(a) Material 1.

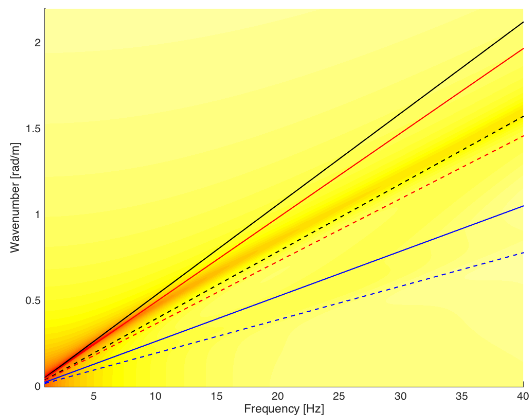

(b) Material 2.

Fig. 4.11: Dispersion diagrams for layered half-space. Black lines represent Rayleigh waves, Red lines for S-waves, and Blue lines for P-waves. Depth 4 m

From the above plots, the straight lines represent the non-dispersive relations for surface and body waves, where the dashed lines indicate the top layer while the solid lines represent the half-space. On the other hand, the dark red shades show the response that correspond to a given combination of the frequency and wavenumber. In Example 2.5 it was shown that the highest wave speed correspond to the P-wave, while the lowest to the Rayleigh wave. Therefore, the non-dispersive relations of this waves can be said to act as 'boundaries' for the response, meaning that there will be no waves that have a higher wave speed than that of the P-wave of the half-space (represented by the solid blue line), and lower than the Rayleigh wave speed of the top layer.

In Figure 4.11a it can clearly be seen that the highest response is produced by the surface waves. Furthermore, this response is the highest at around the frequencies of 5-10 Hz where the most energy is generated. This range, represents a shift of phase speeds, where for the low frequency limit the waves travel with a phase speed that is equal to the speed of the Rayleigh wave for the half space, while in the high frequency limit, this speed changes asymptotically towards the Rayleigh wave speed of the surface layer. The change of velocities is normally related to the effect of wave propagation through different materials. The shift of velocities can tell, that resonance occurs in between that range, also leading to

higher displacements. Resonance is most likely related to the shear waves being reflected up and down in the layer and also due to the effect of the Rayleigh wave. The wavelength increases by decreasing the wavenumber, and at the point where we have resonance it corresponds to a low wavenumber, where the wavelength of the Rayleigh wave equals twice the depth of the soil layer. At that point maximum response will occur. Furthermore, for higher frequencies (short wavelengths) the Rayleigh waves only 'see' the top layer and hence travels in a homogeneous medium with no further dispersion, so there is no distinction between phase and group velocity, [Foti, 2000]. In comparison to the frequency response function found in the sensitivity analysis for soft sand $G_{0.95}$ at 10 m, see Figure 4.2a, the results seem to fit quite well , where the highest response in both cases occurs at the same frequency range.
Apart from the dark red shades, some lighter shades can also be observed in Figure 4.11a. Those shades are associated to the response generated from the body waves, although they have a much smaller effect than the surface waves.

A different case is considered in Figure 4.11b, where the stiffness of the overlaying layer is higher than that of the half-space. Since the wave speeds depend on the stiffness of the soil, a shift of the non-dispersive waves can clearly be observed in the second case, since the wave speeds will be higher in the stiffer layer on top, therefore leading to a smaller wavenumber for the corresponding frequency. The response in this situation is much smaller than in model one, since a stiffer layer on top will normally lead to smaller displacements. One thing that can be noted, is the fact that in low frequencies the wave travels with the Rayleigh wave speed of the half-space, and for higher frequencies this wave speed shifts towards the phase speed of the Rayleigh wave for the top layer but the response is so small that it looks like it never reaches that speed. The response coming from the body waves is much smaller then in the first case. This is also known as the inverse dispersion relation.

In order to check the effect of the depth in the final response, the depth of the top layer is increased to 7 m for both cases of Material 1 and 2. This depth, also corresponds to the maximum depth one layer can have in the model used. The reason behind this is related to the fact that the Green's function matrix for a layered half space becomes singular, it's determinant approaches zero, and consecutively the Impedance matrix, which is the inverse of the Green's function can not be obtained. The dispersion relations for both cases is shown for a vertical applied load and the displacement measured in the vertical direction at observation points in the surface. The results are plotted in Figure 4.12.

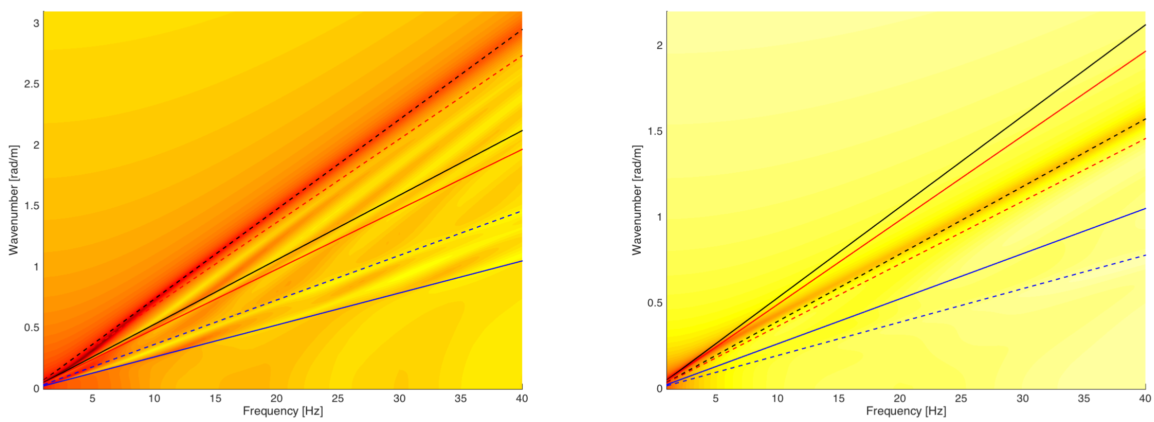

(a) Material 1. (b) Material 2.

Fig. 4.12: Dispersion diagrams for layered half-space. Black lines represent Rayleigh waves, Red lines for S-waves, and Blue lines for P-waves. Depth 7 m.

One can notice from the plot, that in comparison to the first case with depth of four meters, the highest response in the Material 1, occurs at lower frequencies. So the Rayleigh wave changes velocity from the phase speed of the half space to the phase velocity of the top layer, until it becomes asymptotically close, at a frequency range of around 4-8 Hz. This shows that by increasing the depth of the layer, resonance is shifted towards lower frequencies which was also the case observed in the deterministic analysis for the layer depth. The reason for this is attributed to the fact that lower frequency waves have larger wavelengths, and since the depth of the layer is also bigger, more waves will travel and also be reflected up and down at the overlaying layer.

The one thing that these two cases have in common, is the fact that the Rayleigh wave has the biggest influence in the response. But, despite this when the layer depth is increased to 7 m, one can notice that the effect of the body waves in the response is higher than before. This is shown in Figure 4.11a from the darker shades that are spread around. The corresponding case of the response function found in the sensitivity analysis of the layer's depth, see Figure 4.6a, shows the same results, with a resonance frequency at 8 Hz.
On the other side, if the two different cases of Material 2 are considered, there is not much difference separating the two sides, besides the fact that the response in the case of 7 m depth will bend at a lower frequency, changing the phase speed velocity from that of the top layer until it asymptotically approaches the Rayleigh wave speed of the half-space. And since, in this case, a stiff layer with a larger depth is considered, it is reasonable that the response will also be smaller, therefore leading to smaller displacements.

4.5 Summary

In this chapter, the sensitivity of the soil parameters in a layered media is discussed. The influence of the parameters is studied based on a deterministic approach, and a probabilistic approach which is considered to simulate reality. The main points observed during the analyis, are summarized in a general overview.

- **Deterministic analysis** includes assigning deterministic values to the soil parameters, more specifically G, ρ, η, and ν to find their influence in the response for observation points situated at distances of 10 m, 25 m and 50 m away from the source.

- **Probabilistic analysis** was used to find the influence of each soil property by covering the uncertainties related to the material parameters where all parameters are correlated and can change in relation to each other. This is performed by randomization of each variable and finding the influence in variation on the frequency response function.

- The **top layer** is the most sensitive to the variation of the soil properties, since the observation points where the response is measured are placed in the surface.

- The **shear modulus** was found to be the most influential soil parameter in the frequency response, changing significantly the magnitude of the displacement. Low stiffness lead to higher displacements with resonance occurring at lower frequencies while by increasing the stiffness the opposite behaviour was observed. The same behaviour was observed in both approaches with the shear modulus having the highest variation.

- The **mass density** of the material did not change the final response by much, therefore being regarded as a low influential property. Its only effect was a shift and a small increase in the response when the the density was increased which can be attributed to the fact that lower eigenmodes may be affected. A higher influence was observed in the probabilistic analysis but that variation is attributed more to the change in the shear modulus due to the high correlation of the two parameters.

- The **loss factor** has a high influence on the dynamic amplification especially at longer distances due to spreading of the waves over larger distances. Waves are dissipated faster by increasing the material damping while it also has a higher effect on higher frequencies, as was found during the probabilistic analysis while at very low frequencies the variation is almost insignificant.

- **Poisson's ratio** tends to effect more the shape of the response function rather than the amplitude of it. By increasing the Poisson's ratio, the magnitude of the response will decrease but only with little variation, especially at larger distances where the is not much difference in between ratios.

- The **depth** of the top layer has a high sensitivity in the response and is regarded as an important parameter. It was seen that an increase in layer's depth shifts the resonance frequency towards lower frequencies since more waves i.e. wavelengths, will affect the top layer.

- **Dispersion curves** showed that the Rayleigh wave has the highest influence in the response. The waves start to travel with the phase velocity of the half-space but after resonance velocity changes towards that of the top layer. Also for larger depths, there was a higher influence of the P- and S-waves, while the resonance frequency tends to shift towards lower frequencies.

The conclusions made from this chapter, will act as a foundation for the comparison and validation of the semi-analytical model to the experimental results in Chapter 6.

5 Ground Vibration Test in Railway Site

This chapter describes the experimental test which was performed in order the measure the ground response of real vibrations induced by passing trains. All obtained data and videos can be found in Appendix C and provided digital file.

5.1 Introduction

In order to validate the semi-analytical method several field measurements had been conducted. The testing was assisted by COWI which provided the necessary equipment. Passing trains have been chosen as a suitable source for the measurements as they generate the suitable vibrations for further assessment and comparison with the model.

Fig. 5.1: Site location in Ellidshøj, Denmark. [maps, 2017]

With agreement with the company the suitable location, see Figure 5.1, was chosen in Ellidshøj, Svenstrup J located around 15 km from city Aalborg, Denmark. This site was chosen due to several criteria which had to be fulfilled:

- Sufficient distance from train station where trains reach relevant or maximum speed.
- Quiet area with no significant background noise, e.g. construction works, heavy traffic, industry noise.
- Open space, with no obstacles, where measure devices can be placed at certain distances up to 50 m.
- Public area where no permissions are needed.

5.2 Geophones

The measuring tool used for the field testing is geophone. This section describes the principle and mechanism of the device and moreover the explanation of the particular equipment used in testing.

5.2.1 Introduction

Geophone is a device which can measure the ground vibrations or movement. It is the basic tool used by geophysicists and seismologists. The principle is in transformation of the earth motion into electrical impulses. In Figure 5.2 the components of geophone are shown. Here the magnet is fixed to the casing and the mass with the coil around is attached with the sensitive springs which keep the mass, due to inertia, almost stable during the movement of casing. Figure 5.3 shows the real geophone used during the field testing, which is capable to catch vibrations in all directions.

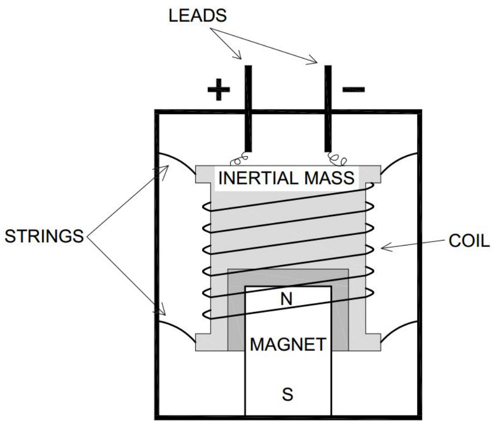

Fig. 5.2: Detail of geophone.

Fig. 5.3: Real device.

The conversion of motion to voltage is based on Faraday's law where the casing with permanent magnet is moving according to earth vibrations around the mass with coil which is catching the change of magnetic field. The induced voltage is than directly proportional to the relative velocity between the magnet, following the earth movement, and the mass with coil.

The advantage of the device is that it does not require any power supply. Moreover the tool is able to catch quite large frequency range. Nowadays the geophones are able to measure vibrations in three directions as they have implemented three coils and magnets inside.

The frequency range is highly dependent on the natural frequency of device. If the ratio between the driving frequency and natural frequency is very small, $\omega << \omega_0$, the motion of the mass follows the casing and therefore the relative velocity is almost zero which leads to no electromagnetic resonance. On the other hand when frequency is too large in comparison to the eigenfrequency, $\omega >> \omega_0$, the mass inside the geophone is almost static and therefore the relative velocity is equal to the ground motion [Hons and Stewart, 2006].

5.2.2 Transfer function

Based on Hons and Stewart [2006] the transfer function is relationship between the input and output of a system in terms of the transfer characteristics, mathematically given:

$$\frac{B}{A} = H \tag{5.1}$$

where

B	Output - Voltage
A	Input - Relative velocity
H	Transfer function

The equation of motion for damped harmonic waves with relative displacement between mass and ground is:

$$\ddot{x} + 2\lambda\,\omega_0\,\dot{x} + \omega_0^2 x = -\ddot{u} \tag{5.2}$$

where

x	Proof mass motion relative to the ground [m]
u	Ground motion [m]
λ	Damping ratio [-]
ω_0	Natural frequency [rad/s]

For better understanding of the relative displacements see Figure 5.4, where one can see that every time the movement of the ground is upwards the mass is going downwards.

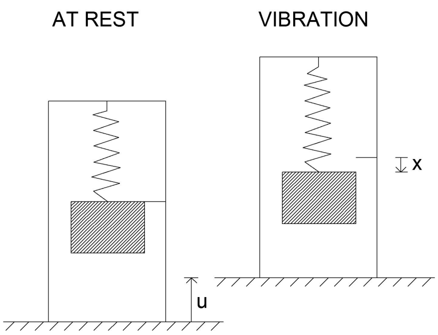

Fig. 5.4: Mass motion during the vibration.

To solve the partial differential equation represented by this equation of motion Fourier Transform is used. It allows to substitute iω for d/dt. The solution of transfer function for geophone where the driving frequency is similar to natural frequency of device, $\omega \cong \omega_o$, meaning that the displacement of the proof mass relative to the sensor is proportional to velocity of the ground motion. Therefore the resulting transfer function will lead to Equation 5.3.

$$H_0 = \frac{\omega^2}{-\omega^2 + 2\, j\, \lambda\, \omega_0\, \omega + \omega_0^2} \tag{5.3}$$

This equation is the main transfer function for geophones whereas it has to be taken in account that it is only valid in a given range of frequency band. For very low and very high frequencies the geophone transducer do not follow this equation precisely, because input A is more proportional either to relative displacement or acceleration.

5.2.3 Geophone INFRA V12

The used geophone in this project is INFRA V12 from Sigicom which allows to measure three directions. The whole field monitoring system is composed of the Datalogger and connected geophones, see Figure 5.5. According to Sigicom [2013a] there can be connected 9 nodes per each Datalogger, where each node represents one direction in this case. In total three geophones V12 can be then connected.

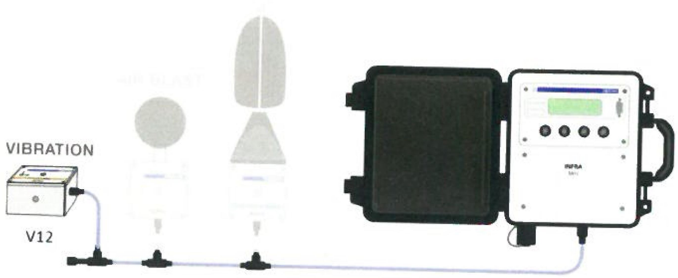

Fig. 5.5: Setup of the INFRA field monitoring system. [Sigicom, 2013a]

Geophone contains several measurement standards. They vary with their velocity and frequency range. The used standard for the measurements is DIN4150-3 Anlage, which is a German standard dealing with vibrations in buildings and their effects on structures. The frequency range covers $1 - 315\,\mathrm{Hz}$ and maximum velocity of $25\,\mathrm{mm/s}$. Further on given parameter has to be set up before the measurement.

The Interval time can be defined between 5 seconds up to 20 minutes which means it collects data for given time period and after sends it to database. If the device is not triggered the only data which is stored is maximum velocity in each direction measured during the interval.

To obtain and store the precise data, the device has to be triggered. This means that the data collected during the certain time, defined by transient time, will be stored in a time domain with timestep of $t_s \cong 2.45\ 10^{-4}\ s$. The range of the transient time can be set up between 1 up to 40 seconds. Moreover one more second before the geophone was triggered is also saved.

Based on Sigicom [2013b] there are two modes for Datalogger. Reg Off mode means that all nodes(geophones) are connected but no data is registered and stored. In this mode is possible to change connections and geophones. In the Reg On mode the data of measurements with its specifications and settings is sent by GSM signal from the Datalogger to Sigicom servers. In here it is not recommended to unconnect and connect any geophone as the signal from nodes might be lost and the Datalogger has to be rebooted.

The provided devices from COWI company as part of Urban Tranquility project are:

Tab. 5.1: Devices.

	Serial number	Note
Sensor 1	2110	-
Sensor 2	4960	-
Sensor 3	20800	-
Datalogger	S/N U14-01330	-

5.3 Experimental set-up

Before the testing can be performed the proper set-up of devices has to be done. First the holes of depth approximately 60 cm are dug to remove the top layer soil which usually includes vegetation, mud or some other elements that can fake the measurements and do not correspond to real behaviour of the soil medium itself. As the geophones have to levelled and properly attached to the ground, they are fastened on the concrete bricks which are then placed inside the holes. The bricks are afterwards covered by the soil also from the sides to ensure no undesired movement, see Figure 5.6.

Fig. 5.6: Geophone attached to the ground through brick.

Geophones are placed perpendicularly at distance of 8, 20 and 40 m from the centre of double track where Sensor 1 is the closer to the track and Sensor 3 is the furthest, see Figure 5.7. Sensors longitudinal direction is pointing parallel to the track and transversal direction is aimed perpendicularly away from the track.

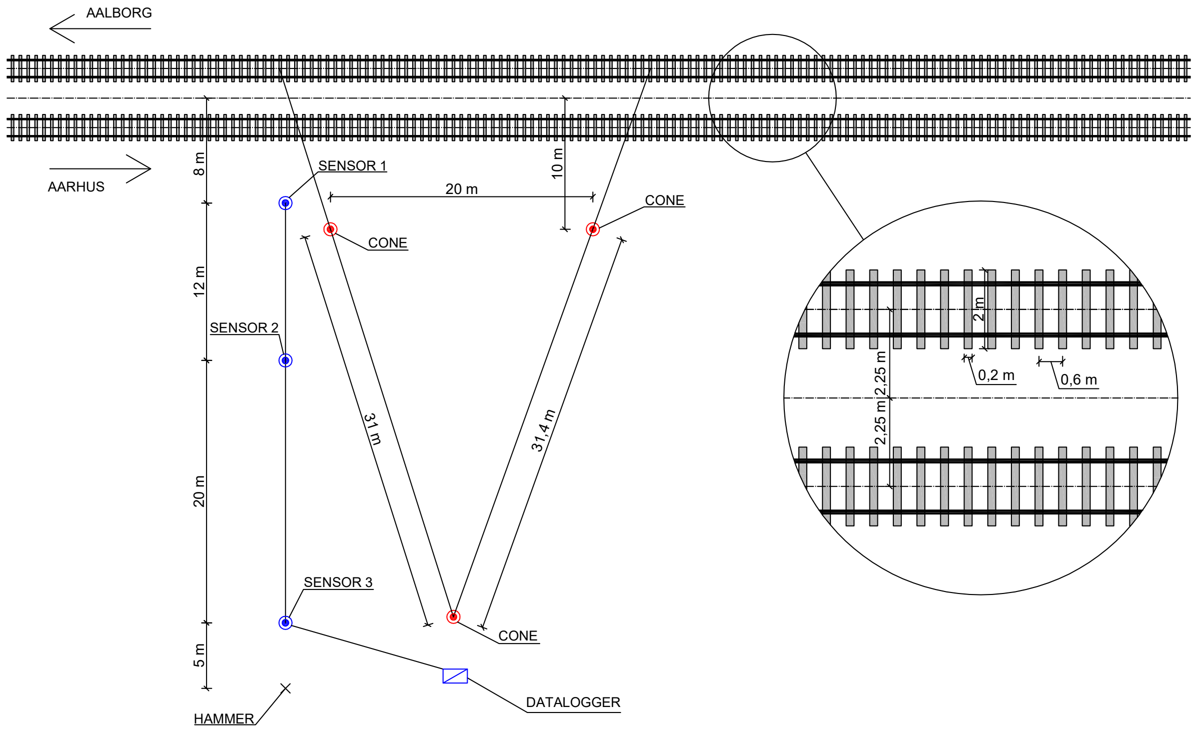

Fig. 5.7: The layout of the site.

On the site there are placed three marking cones at given places as seen in the Figure 5.7 which are used in Section 5.4 for calculation of speed of the trains. One cone is used as an observation point where the video of approaching trains is made and two other cones are placed in a parallel line with the track to create a triangle which is used to measure the exact distance for calculation of speed of the train.

Hammer test

Moreover, four hammer tests were conducted at the site. Test 1 and 2 correspond to horizontally excited impulses while test 3 and 4 are vertically excited impulses. The hammer was placed 5 m away from the sensor 3 and lined with the other two sensors. The idea here is to produce some rapid impulses so that they can be clearly interpreted and used for a more precise calculation of the wave speed.

Figure 5.8 shows the hammer equipment used in the test. The equipment made of three main parts, the hammer itself, the support for the hammer and the base. This system allows a regular and constant impulse generation since the hammer is released at the same height in every performance. The original purpose of the test is to create SH-waves where the force from hammer is applied in the perpendicular direction to the sensors arrangement as can be seen in the figure.

Fig. 5.8: Hammer system for SH-wave generation.

The wave speed calculated from the hammer test is used as a first guess for the modelling of the soil. Unfortunately it was not possible to obtain approaching SH-waves from the horizontal test as the two sensors located further away did not show the proper response due to high noise. Therefore two vertical tests are used to estimate the Rayleigh waves which is assumed to have highest influence on the response. In order to prove these waves the particle paths are showed in Figures 5.9 and 5.10, where the transversal response is plotted against the vertical.

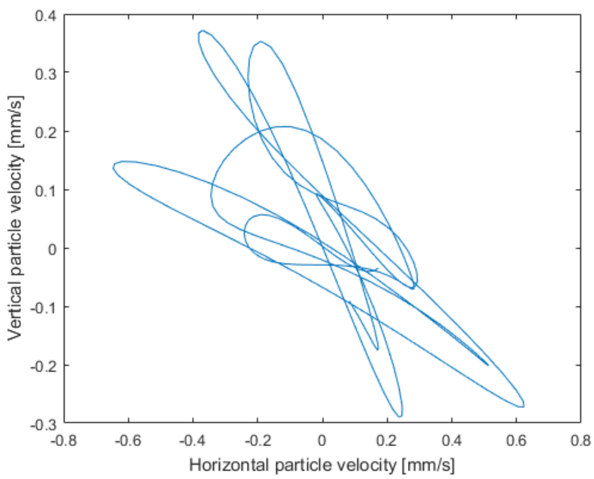

Fig. 5.9: Particle path for Hammer test 1.

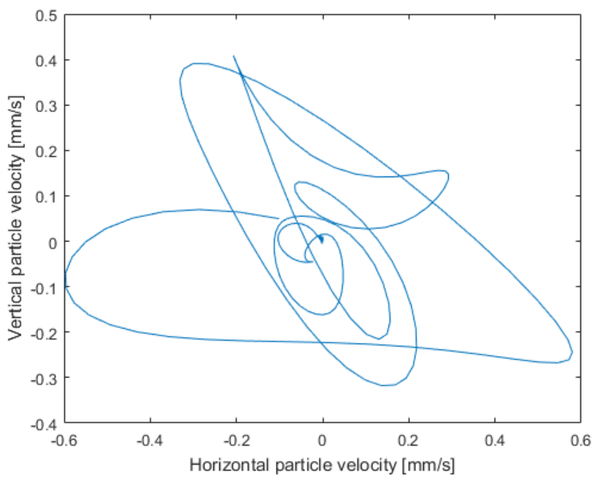

Fig. 5.10: Particle path for Hammer test 2.

Two main observations can be mentioned here. First, in both cases the particle path shows elliptical movement which indicates Rayleigh waves. If the the incident waves would be harmonic then the behaviour would be pure ellipses as was explained in Section 2.3.2. It should be noted that when the response was plotted by each time step it showed the retrograde motions which indicates also the Rayleigh wave behaviour near the surface. Moreover, the ellipses are not vertical, they change the angle of rotation, which is usually the case for layered elastic medium.

Datalogger set-up

The interval time of device for storing data is set to 2 minutes which was recommended by COWI employees and transient time for precise measurements is set to 16 seconds which is assumed as a reasonable time to capture all necessary data from the passing train. The device is triggered manually each time when there is visual contact on approaching train.

5.4 Train types

The focus in the experiment is on the ground-borne noise resulting from trains. The main source of vibrations in the site location are two types of trains *IC2* and *IC3*.

IC3 is a Danish inter city train powered by diesel engines operating in Denmark since 1989 [Jernbanen.dk, 2017]. The number three indicates simply three-carriage trainset, where front and end carriage are combined passenger and motor carriages and the centre one is purely for passengers. The train *IC2* is basically offspring of the *IC3* but is only composed of two carriages and instead of four engines only two are placed. Some technical properties of the trains can be seen in Table 5.2.

Tab. 5.2: IC2 and IC3 trains Characteristics.[Banedanmark, 2016]

	*IC*2	*IC*3
Length [m]	41.0	58.8
Wagon length [m]	20.5	20.5
Medium wagon length [m]	-	17.75
Max speed [m/s]	140	180
Weight [t]	64	97

Then the speed of the actual trains when the test was performed is calculated. The speed is simply calculated from the videos recorded at the site and the distances calculated by the triangulation shown at Figure 5.7. The trains speed are depicted in Table 5.3.

5.5 Measurements

In this section the raw data obtained from geophones are presented and processed for further comparison and validation with the model.

5.5.1 Presentation of raw data

Several measurements have been conducted on the site. Each time the train was passing by, the Datalogger was manually triggered and the data was sent and stored at Sigicom server. In Table 5.3 can be seen all the measured trains with the calculated velocities and their masses.

Tab. 5.3: Measurements.

Name	Direction	Type	Velocity [m/s]	Weight [*tones*]	Note
Train 1	N: Aalborg	IC2	28.531	64	-
Train 2	N: Aalborg	IC3	30.095	97	-
Train 3	S: Aarhus	IC3	26.030	97	-
Train 4	N: Aalborg	IC3	29.778	97	-
Train 5	N: Aalborg	IC2	29.125	64	-
Train 6	S: Aarhus	IC2	27.751	97	-
Train 7	N: Aalborg	IC3	28.575	97	-
Train 8	S: Aarhus	IC2	32.003	64	-
Train 9	S: Aarhus	IC6	data not stored	194	double set IC3 data not stored
Train 10	N: Aalborg	IC2	26.325	64	data not stored
Train 11	N: Aalborg	IC3	30.257	97	data not stored

There have been several misreadings of the device when not all the necessary information was sent to the server and several measurements from given nodes (read directions) were not stored and therefore last three trains are not used for further processing.

Further on the trains are split in two groups depending on the direction they traveled as it significantly affects the measurements. This is caused by different distances of the sensors from each track. Whereas for trains traveling to direction of Aalborg the first sensor is located at distance of 10.25 m, for trains going to Aarhus, that is the opposite direction, the sensor is situated only 5.75 m from the center of the track. In Figure 5.11 there can be seen the response of the train number 8 in time domain for all three sensors, this train is an IC2 train.

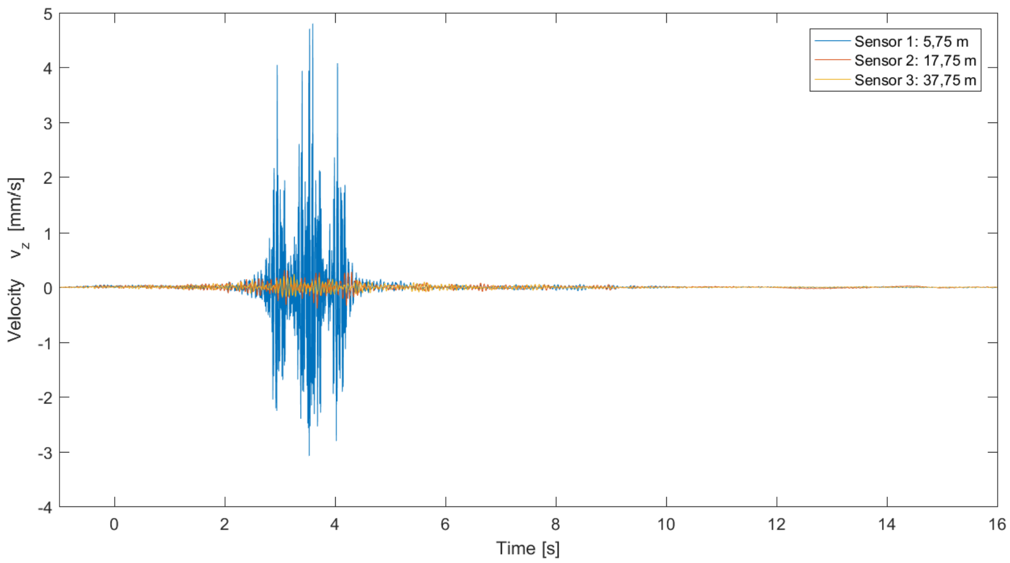

Fig. 5.11: Response of sensors in time domain for Train 8.

There, it can be seen the significant response at time between 2th and 5th second which indicates the passage of the train. Sensor 1 is showing reasonably the highest response. Additionally three main peaks are clearly shown, these are due to the distance between the wheel axles of the train.

5.5.2 Data processing

Since the raw data obtained from the geophones is in time domain a Fast Fourier Transformation (FFT) is needed to calculate the response in frequency domain. The response in frequency domain gives an idea of the frequency ranges of the waves generated by the trains-track-soil interaction and the irregularities related to it. The response of Train 8 in frequency domain can be seen in Figure 5.12.

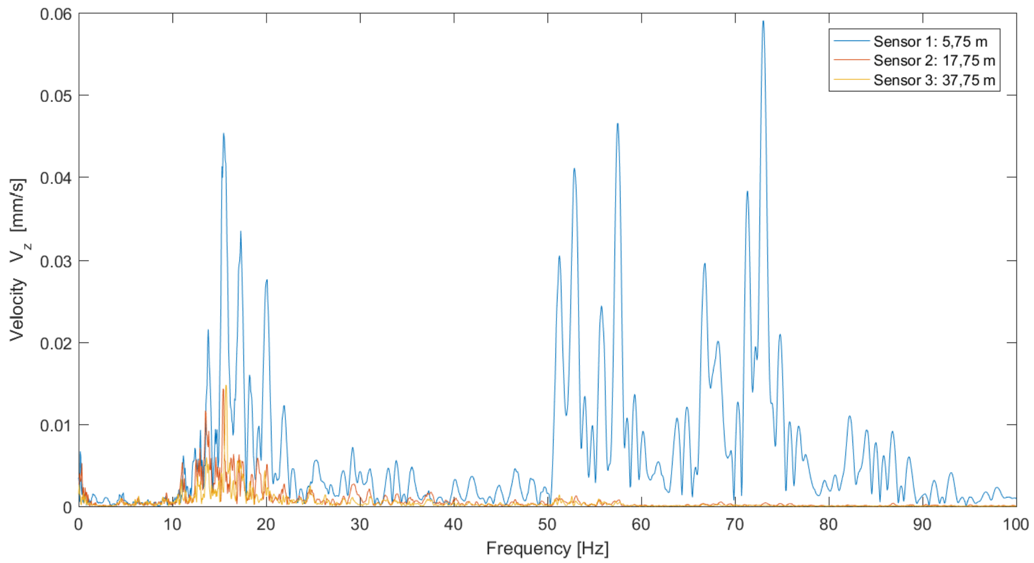

Fig. 5.12: Three sensors response in time domain for Train 8.

As the time step of measurement for each geophone is low, $t_s \cong 2,45 \cdot 10^{-4}$ s, the actual frequency range of the data after FFT goes up to 2000 Hz. Nevertheless, since the project is dealing with the train induced vibrations affecting surrounding buildings and people, only frequencies up to 100 Hz are evaluated.

Factors affecting the vibrations induced by train

Figure 5.12 shows wide ranges of frequencies in the response. These are due to multiple factors related to the train and track. Based on Hall [2003] and also Krylov and Ferguson [1994] the main factors influencing the behaviour of train-induced ground vibrations are:

- Stress waves from track structure response
  - Speed of train
  - Axle weight
  - Spacing of wheel axles
- Vibration from wheel-rail interface
  - Wheel irregularities: eccentricity, imbalance, flats
  - Dynamic properties of the bogies
  - Unsteady movement of the vehicle: bouncing, rolling, pitching
  - Misalignment of motors
  - Acceleration and deceleration of train
- Discontinuity on the track
  - Rail defects: unevenness, waviness
  - Spacing and interval of rail joints
  - Switches

  - Curves and tiling track
- Variable support
  - Geometry, stiffness and spacing of sleepers
  - Geometry, stiffness and heterogeneity of the ballast
  - Stiffness and geometry of the ground

To be able to interpret the the data obtained from geophones it is essential to know the speed of the train and dimensions such as spacing of wheel axles, wheel diameter, length of bogie and so on. The scheme of selected dimensions can be seen in Figure 5.13. Moreover the velocity of each train was calculated and shown in Table 5.3. For Train 8 particularly the velocity is 32.003m/s. By knowing these parameters the relation with the peaks in the measured responses in the frequency domain.

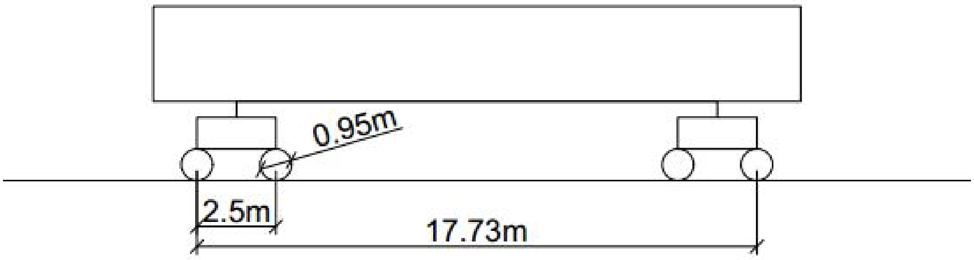

Fig. 5.13: Scheme of carriage dimensions.

Five main factors have been considered for calculating these frequencies. Wheel irregularities, spacing of wheel axles, sleepers, spacing of bogies and the train weight as quasi-static load. Table 5.4 shows the frequencies corresponding to each factor. Then Figure 5.14 shows the location of the respective frequency in the frequency domain response.

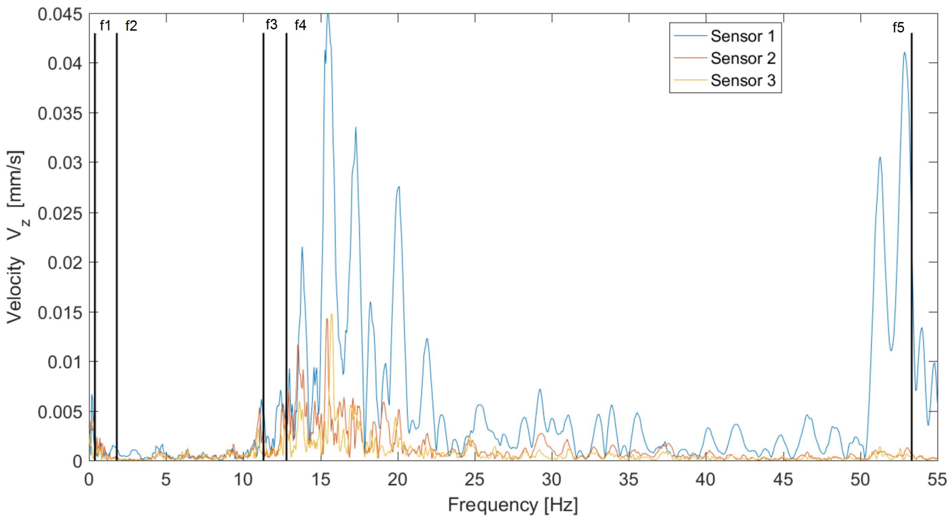

Fig. 5.14: Location of frequencies due to irregularities in the frequency domain response.

Tab. 5.4: Corresponding frequencies to factors affecting the frequency domain response.

Factors	Frequency [Hz]
Train weight	$f_1 = 0.379$
Spacing of bogie	$f_2 = 2.101$
Wheel irregularities	$f_3 = 11.310$
Spacing of wheel axles	$f_4 = 12.800$
Sleepers	$f_5 = 53.338$

5.5.3 Conversion to 1/3 octave band center frequencies and decibels

The further evaluation of the data and comparison with the model is performed in sound spectra where the x-axis of the spectrum is represented in 1/3 octave frequency bands rather than in narrow frequency bands. This representation is based on the perception of sound by human ear and allows to compress the amount of data [Recipes, 2004]. However there is a significant loss of information.

There are 21 1/3 octave band frequencies in the range from 1 to 100 Hz, which are used in the project. These are: f_n = [1 1.25 1.6 2 2.5 3.15 4 5 6.3 8 10 12.5 16 20 25 31.5 40 50 63 80 100] Hz.

There is an upper and lower bound in between each consecutive frequency where the RMS value in this range is taken as a centre frequency velocity, see Equation 5.4.

$$V_{n,RMS} = \sqrt{\frac{\sum_{i=f_{n,lower}}^{f_{n,upper}} (V_{n,i} \cdot V_{n,i}^{*})}{m_n}} \tag{5.4}$$

where

$V_{n,RMS}$	RMS velocity for given centre frequency [mm/s]
$V_{n,i}$	Response velocity of response velocity at certain frequency band [mm/s]
$f_{n,lower}$	lower bound for given 1/3 octave band frequency: $f_{n,lower} = f_n \cdot 2^{-\frac{1}{6}}$ [Hz]
$f_{n,upper}$	upper bound for given 1/3 octave band frequency: $f_{n,upper} = f_n \cdot 2^{\frac{1}{6}}$ [Hz]
m_n	number of frequencies in the range between upper and lower bound [-]

The resultant velocities are afterwards converted to decibels by Equation 5.5 where $V_0 = 5 \cdot 10^{-8}\ m/s$, which is the reference particle velocity in the air.

$$V_{RMS,dB} = 20\ \log_{10}\left(\frac{V_{RMS}}{V_0}\right) \tag{5.5}$$

RMS values in 1/3 octave bands are now plotted in Figure 5.15 where the response in all three sensors for Train 8 can be seen. For this purpose a staircase diagram is chosen for clearer understanding of response in each octave band.

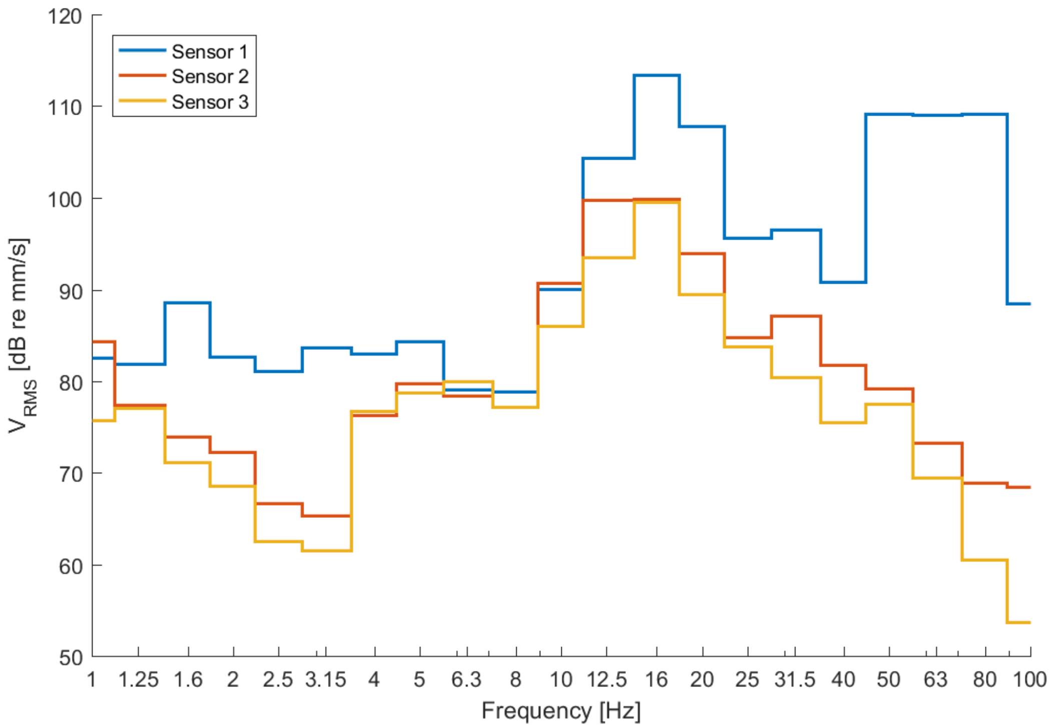

Fig. 5.15: RMS velocity response for Train 8 in 1/3 octave bands.

When the data is smoothened the overall response follows the original behaviour. Further on, several comparisons between different trains are done. All trains are in both directions are plotted together in Figures 5.16 5.17, 5.18 which correspond to Sensor 1, Sensor 2 and Sensor 3, respectively . The trains with same parameters, like direction and type of train are characterized by the same colour and line type. These trains are later used as reference trains for modelling the soil medium.

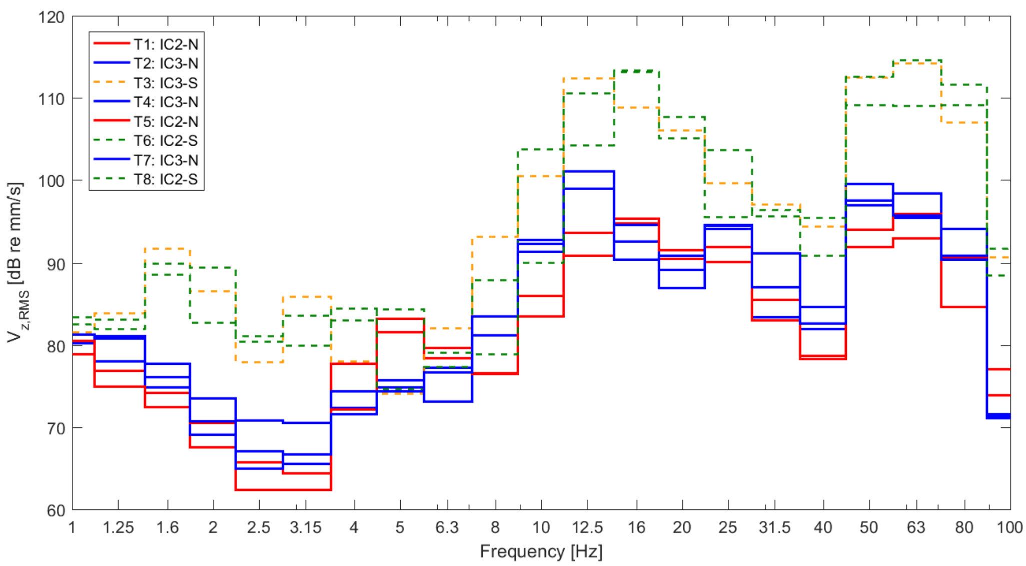

Fig. 5.16: RMS vertical velocity response of all trains at Sensor 1 in 1/3 octave bands.

In Figure 5.16 it can be seen that trains passing on south bound (Aarhus direction) exhibits significantly higher response which is reasonable as the sensors relative distance is 4.5 m lower than in case of north bound. At certain octave bands, 5 and 6.3 Hz specifically, the same response from the trains can be seen no matter on which bound they are located. This behaviour is further studied in Chapter 6. Moreover *IC2* trains generally exhibits lower response at most of the frequencies which is reasonable due to the lower weight and smaller size, but at three octave bands between $4 - 6.3$ Hz the behaviour is reversed for both tracks which by be the resonance for the given geometry of the train.

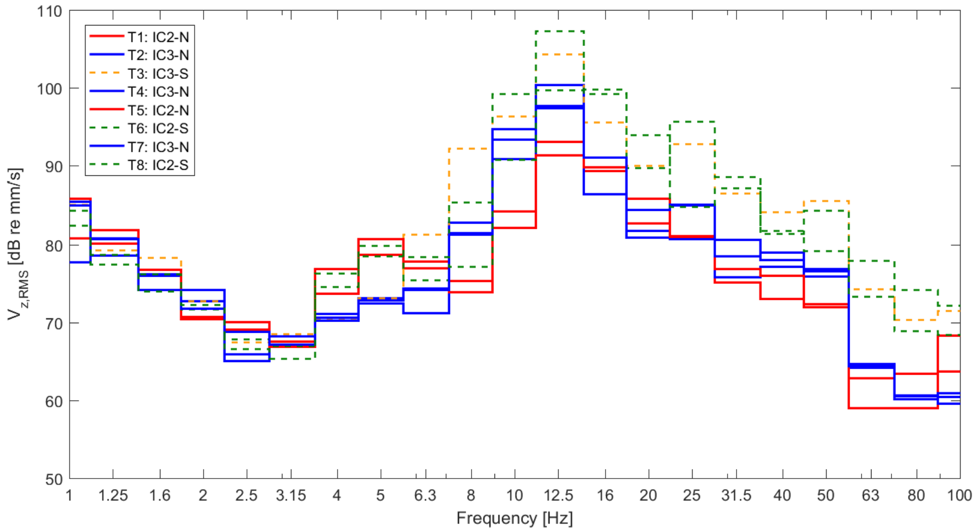

Fig. 5.17: RMS vertical velocity response of all trains at Sensor 2 in 1/3 octave bands.

In Sensor 2 the overall response drops which is caused by further distance and waves attenuation. The differences between train directions also decreased as the ratio between distances from both tracks is lower. Moreover high frequency responses drop rapidly which is probably caused by high material damping of waves in these frequencies.

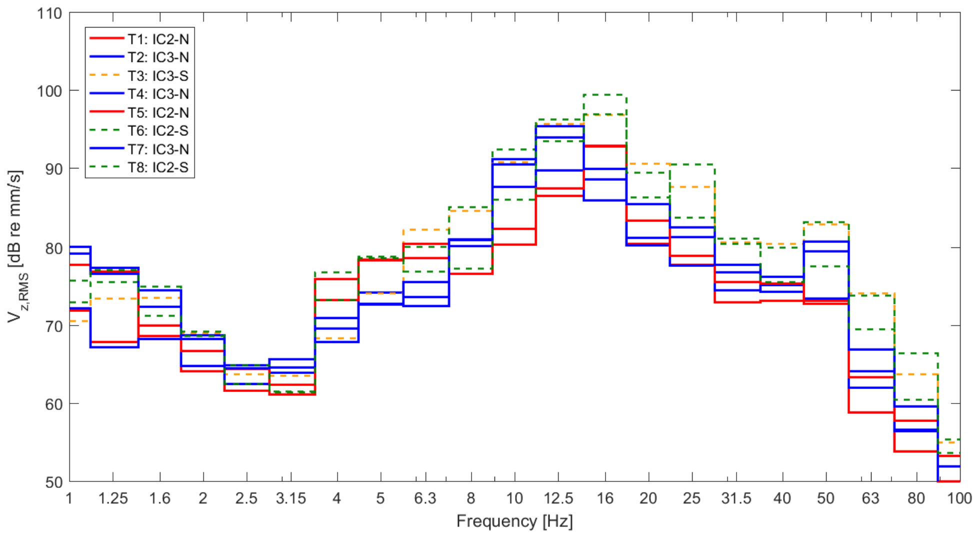

Fig. 5.18: RMS vertical velocity response of all trains at Sensor 3 in 1/3 octave bands.

Last sensor in comparison to first two shows only small deviation both for the train type and also direction, which is due to the far distance of the observation point.

5.6 Summary

The experimental test was conducted in order to have some real data from the soil response behaviour. The chosen location had to satisfy specified requirements in order to get proper measurements from passing trains.

- For the purpose of the experiment **geophones** were used as the main tool in order to measure ground vibration. The overall description of the device and its physical principles were provided for better understanding how the device should be properly used.

- There were 11 measurements of passing trains conducted and the data was processed and smoothened to 1/3 octave band frequencies for the further process of validation of the model. This provides the advantage of saving the computational power and time of the calculations.

- During the site investigation several **hammer tests** were performed to find the wave propagation behaviour and further calculation of the top soil parameters. The main objective was to find phase velocities of SH-waves, however only Rayleigh waves from vertical hammer tests were obtained and could be used for further investigation.

- **Investigation of the measured data** was also conducted in order to explain the sources of vibrations. Therefore the velocities of individual trains were calculated and characteristic features and dimensions of the trains were described.

- Finally the responses from the trains at each sensor were discussed in order to understand different behaviour at certain octave bands. These trains are used in Chapter 6 for the purpose of implementing real loads to the computational model.

6 Validation of the model based on experimental test

This chapter deals with the validation of the computational model where the real case is implemented. Meaning that the measured data from the field is used for estimation of the model, soil stratigraphy and soil parameters. Further the response of the model is compared to the real measurements.

6.1 Estimation of soil stratigraphy and properties for reference model

In this section the first estimations on soil parameters and layers are made. This is based on available data of boreholes located close to the experimental site and moreover the calculation of the phase velocity of shear wave in the top layer performed by hammer tests. Furthermore, a reference model has been built which includes all these parameters and stratification estimated which is later used for comparison and fitting to the final design of the modelled soil.

6.1.1 Estimation of in situ soil shear modulus

In order to calculate the shear modulus, G, of the top soil on site, first it is necessary to obtain the S-wave speed, based on the relation specified in Equation 2.15, rewritten here, $G = c_S^2 \cdot \rho$. The SH-wave was supposed to be obtained from the horizontal hammer test, but since the data was not sufficient due to the large distance between the sensors and the effect of noise, then only the vertical hammer test was taken into account. Therefore it is assumed that the Rayleigh wave can be found as it has the highest influence on the surface.

The distance of travel is known from Figure 5.7 and a travel time is calculated from the shift between the response of Sensor 3 and Sensor 2. This is a crude estimation as this shift is calculated from peaks from vertical response of the geophones, meaning that the peak at one sensor represents the same wave as the peak in second sensor. This estimation leads to neglecting reflections and grouping of waves. Therefore this calculation is used only as a first guess. The c_R is then calculated by Equation 6.1

$$c_R = \frac{distance\ of\ travel}{travel\ time} = \frac{x}{t} \tag{6.1}$$

In theory the wave velocity calculated for each test should be the same. Nevertheless some differences arise due to the irregularities of the soil and measurements. Once the Rayleigh wave velocity is calculated, then c_S can be found based on the approximation where c_R is 90% of c_S. Table 6.1 shows the shear wave speeds corresponding to each test.

Tab. 6.1: Wave propagation velocity for S-wave.

Test no.	Wave propagation velocity [m/s]
1	138.12
2	127.48
3	126.94
4	100.35

To further be able to calculate the shear modulus, first the soil mass density, ρ, is assumed to be $2000\,\mathrm{kg/m^3}$ and the wave propagation velocity has been averaged for all the tests. The resulting value for the shear modulus of the top layer is $G = 30.37\,\mathrm{MPa}$.

6.1.2 Boreholes data

There are four available boreholes in a reasonable distance from the site. The data is taken from the Geological Survey of Denmark and Greenland database. See Figure 6.1. One can see the location of three geotechnical boreholes represented by brown dots and one environmental shallow borehole performed directly on the track, shown in yellow color. Red dot represents the place where the experimental test was conducted.

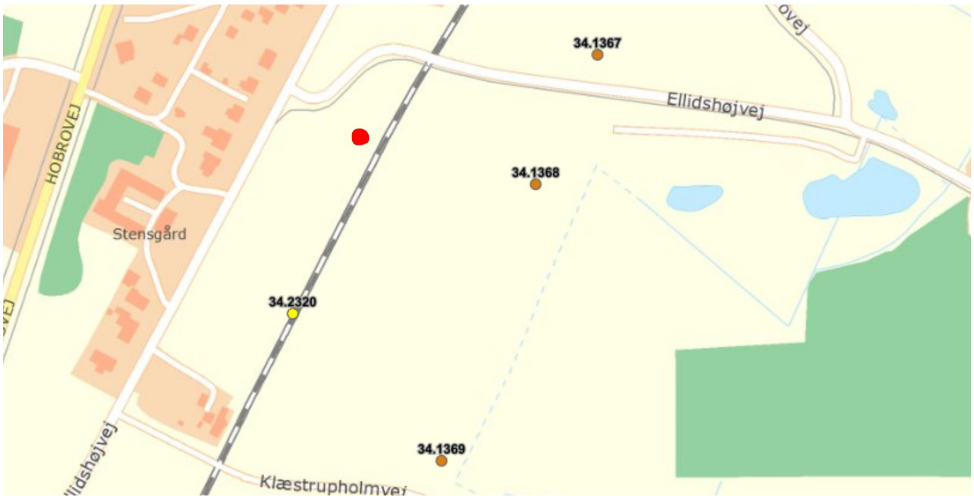

Fig. 6.1: The location of available boreholes close to site. [GEUS, 2000]

The actual boreholes and their stratification classification can be found in Appendix D. All borehole data vary significantly, so the classification of the soils on the site was estimated mainly by engineering judgement. The table of the soil layers and their estimated properties can be seen in table 6.2.

Tab. 6.2: Soil properties of reference model.

	Shear Modulus G [MPa]	Poisson's ratio $\nu[-]$	Density ρ [kg/m^3]	loss factor $\eta[-]$	Depth h [m]
Layer 1	30	0.3	1900	0.04	1.5
Layer 2	30	0.4	2000	0.04	1.5
Layer 3	42	0.4	2000	0.04	4
Layer 4	81	0.4	2100	0.04	∞

Here the top layer is split into two layers with different Poisson's ratio, by assuming that the water table is situated at the depth of 1.5 m and therefore the ground below is saturated. This layer is considered mainly organic soil mixed with sand and clay. Based on the boreholes the third layer is assumed stiffer mix of mainly sand and some organic material. The bottom layer is designed as a half-space made of $G_{0.95}$ for hard sand.

6.2 Calculation of the Force spectrum

Modelling of the rail track - Force modelling

The passing train produces dynamic loads on the rail track which are then transferred to the soil medium through the sleepers. These loads cause the ground response vibrations. The excitation mechanisms were mentioned in Chapter 5 while here a detailed explanation on how to apply the load in the computational model is given.

In reality the load is applied through each sleeper throughout the time. The loads are then assumed to behave independently of each other. According to Andersen [2010], the total load is then calculated as the root mean square value of all these independent loads.

The way how the track is modelled in the computational model is somehow reversed. Instead of generating multiple loads at different positions, depending on the train length, multiple observation points (response points) are created which are at the distance of a given sensor and the load is applied only through a single flexible disc.

The reason why flexible disc is used, and not the actual model of a sleeper represented by rigid foundation, is that in the frequency range $1-100$Hz the wavelenghts of the generated elastic waves are much larger than the sleeper dimensions [Krylov, 1995]. This was also proven in Section 3.6 where it was shown that in low frequency and moreover larger distances it does not really matter which kind of load application is used. Therefore to avoid discretisation of several points in rigid body, flexible load is assumed as a reasonable solution for the problem.

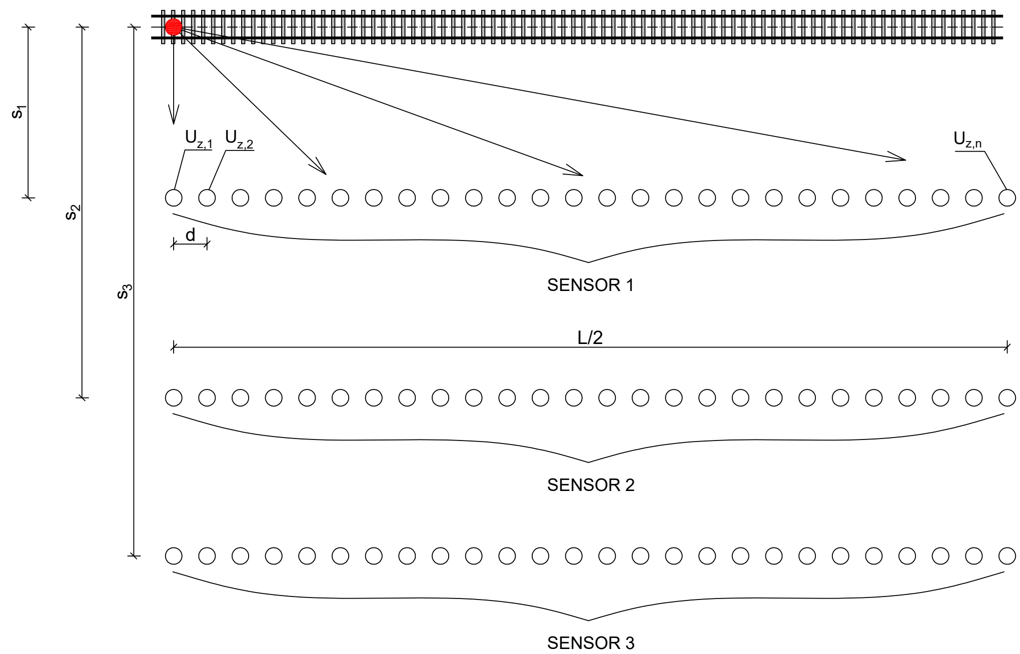

Fig. 6.2: Points representing the actual sleepers.

In Figure 6.2 the red circle represents the load and points $U_{z,1}$, $U_{z,2}$...$U_{z,n}$ represent the frequency response functions at given distance from the source. This corresponds to same situation as if the load was applied individually on each sleeper (point) and the response was measured at single location. Moreover in order to save computational time, only half of the points are simulated as Figure 6.2 shows, then by applying symmetry all the rest can be obtained. The total length, L, is meant to be the length of the train while the distance, d, is the actual span between the sleepers.

Frequency response function for applied loads

In this project only the influence in vertical direction is considered. Moreover the displacement field has to be transferred to velocity field as all the real data is stored and processed in manner of velocity, see Equation 6.2

$$V_z(s,f) = U_z(s,f)\,2\pi f\,\mathrm{i} \tag{6.2}$$

The resultant frequency response function is calculated as RMS of all individual velocity fields, $V_{z,n}$, located at given distances s_1, s_2 and s_3 from the track, see Equation 6.3.

$$V_z(s,f) = \sqrt{\frac{V_{z,1}(s,f)\cdot V_{z,1}^*(s,f) + \sum_{i=2}^{n}\left(2\,V_{z,n}(s,f)\cdot V_{z,n}^*(s,f)\right)}{2n+1}} \tag{6.3}$$

where

$V_{z,n}(s,f)$	FRF for given sleeper at vertical direction.
$V_{z,n}^*(s,f)$	Complex conjugate of FRF for given sleeper at vertical direction
n	Number of sleepers where the force is applied

This is actually a simplified way of constructing a force caused by the train as it is assumed that each sleeper behaves as an independent load. By this manner the response functions are calculated for each individual sensor location. The affect of different train sizes and spans between sleepers on FRF is studied in the following Section 6.4.

Real force spectrum calculation

As the force applied in the model is a unit load, the real force spectrum has to be derived. This can be done by using the real spectrum of a given train at certain location and divide it by the frequency response function at the same point, see Equation 6.4

$$P(f) = \frac{V_{Real}(f)}{FRF(f)} \tag{6.4}$$

Once $P(f)$ is known it is possible to solve the real response at any location in the medium by using the model. Here the model has to be validated and defined with the actual soil properties and stratification to ensure realistic results. To do so, a calibration must be applied to the model by using the response from different locations and by comparing this to the real data from geophones.

6.3 Response of the reference model

In the reference model the length of the applied load, L, is assumed to be 60 m which illustrates the approximate size of the train IC3, while the distance between the sleepers, $d = 0.6$ m, is taken from real situation as was shown in Figure 5.7. Based on the symmetricity of the problem, it will cover a total number of sleepers of $n = 51$. The force spectrum is derived from Train 2 at the location of Sensor 1, meaning $s_1 = 10.25$ m. The response and comparison with the real measurements can be seen in Figure 6.3 for Sensor 2 and in Figure 6.4 for sensor 3. Notice that the force spectrum was calculated for 1/3 octave bands and the final response was converted to decibels.

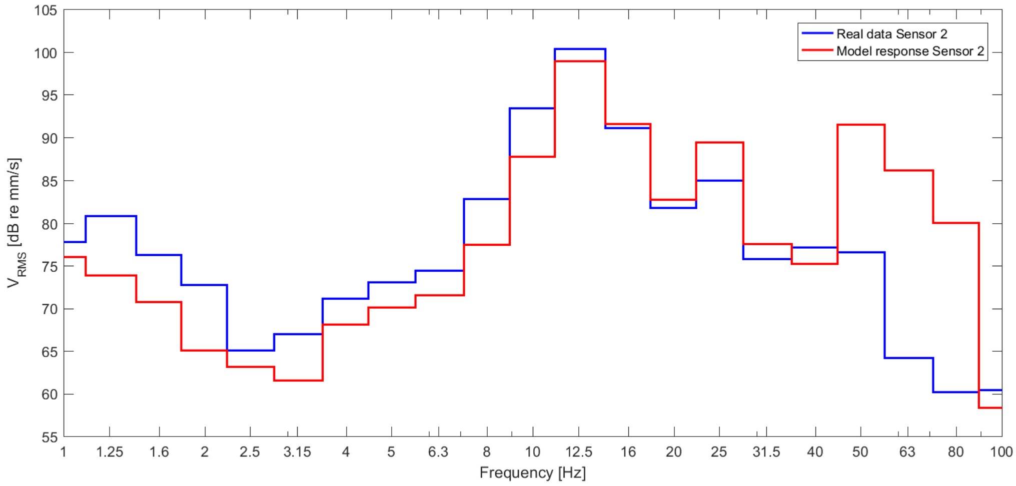

Fig. 6.3: Comparison of real response from T2 to model response at Sensor 2.

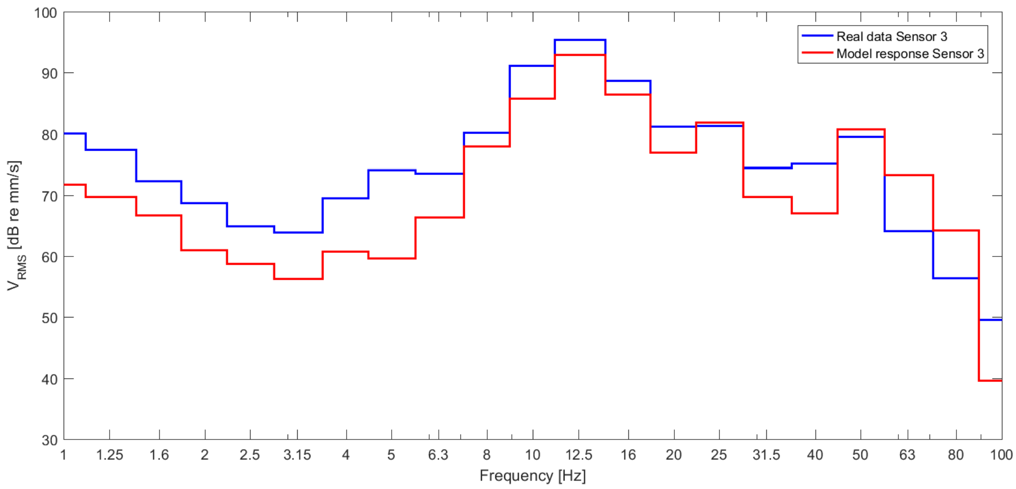

Fig. 6.4: Comparison of real response from T2 to model response at Sensor 3.

The model exhibits lower response in both sensors for lower frequencies and on the other hand higher velocities at high frequency. This might be caused by several factors. The first factor can be due to the incorrect design of the load application where in reality the response at the sensor might be affected by larger lengths than the train itself. The second reason can be related to the crude stratigraphy assumed for the medium and also its material properties. Therefore in the following section the study of these aspects is conducted.

6.4 Optimisation of the input parameters

The aim of this section is to obtain a closer match of the response generated from the model to the real measurements, by assessing different input parameters, more specifically the length of the track, the distances between the sleepers and the loss factor.

6.4.1 Variation of the length of modelled track and distance between sleepers

Here, three cases are studied and their impact on the final response is assessed. In Table 6.3, the input parameters for the model are presented for each of the cases.

Tab. 6.3: Cases for track variation.

	Length L [m]	Span between sleepers d [m]	Number of Sleepers n [$-$]
Reference model	60	0.6	51
Case 1	120	0.6	101
Case 2	30	0.6	26
Case 3	60	1.2	26

At first the influence on frequency response functions is discussed. A unitary load is still assumed, which is spread over the observation points i.e. sleepers. In Figure 6.5 all three cases and the reference model at each sensor are plotted.

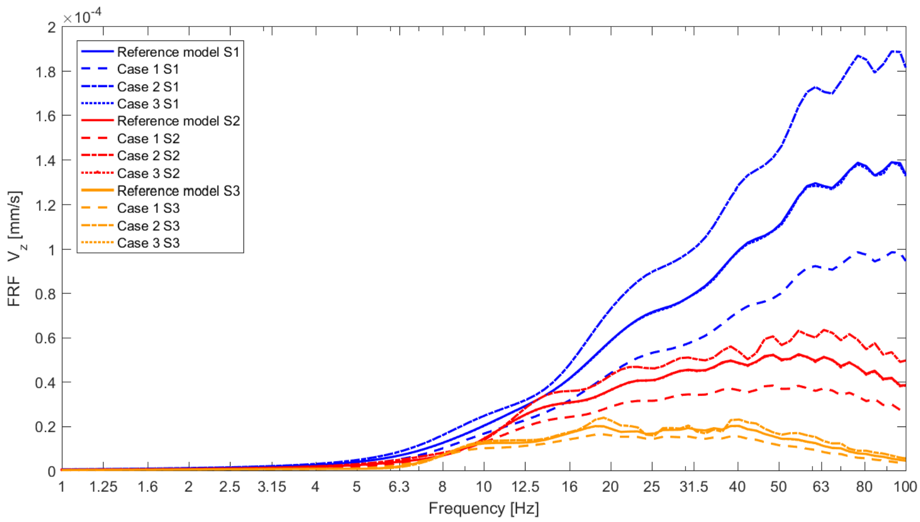

Fig. 6.5: FRFs in vertical direction of four cases at each sensor.

One can see that for the two cases where the length of the track is changed there is a significant impact on the FRFs, which can be due to the fact that the unit load is distributed on different area, and therefore the response at the sensor is changed. In another words, e.g. in Case 1, the total response is lower as there are twice the amount of sleepers which are located further away and exhibit low velocities. Therefore when the RMS is done, the resultant velocity is lower.

In Case 3 when the spans between sleepers were changed, no impact on the FRF is observed. The reason is that the same unitary load is applied and distributed in both 26 or 51 sleepers. It does not have any affect on the total response (RMS) as the distances are kept the same, the only change being that in Case 3 the response from each sleeper is double that of the reference model.

The effect of these response functions on the real case can be seen in Figures 6.6 and 6.7. Case 3 is omitted as it was proven that it has no impact on the model.

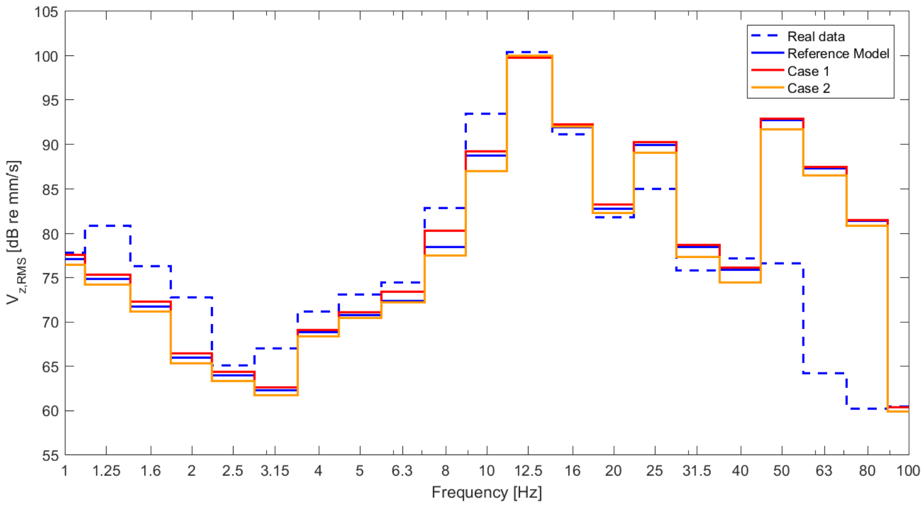

Fig. 6.6: Vertical response at three modelled cases and the real train T2 at Sensor 2.

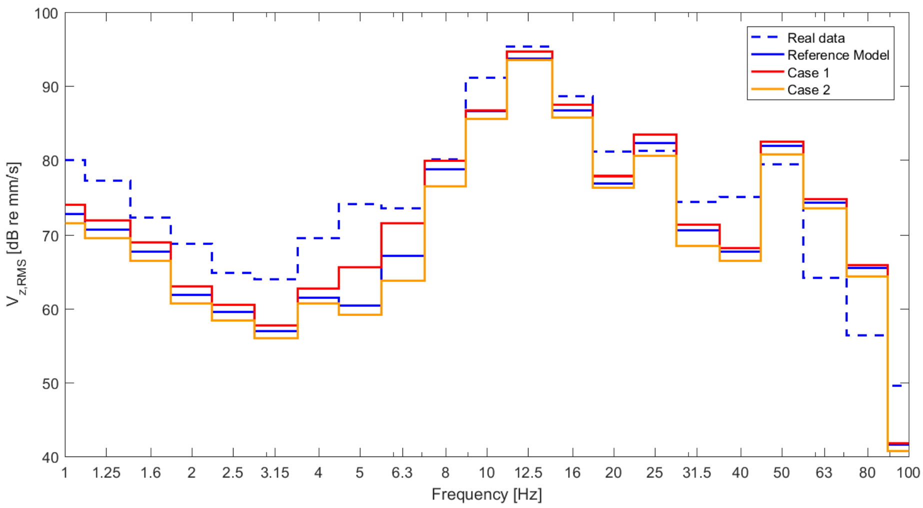

Fig. 6.7: Vertical response at three modelled cases and the real train T2 at Sensor 3.

Generally it is observed that the size of the affected track has no major influence on the overall response. On the other hand at certain frequencies, mainly in the third sensor it has reasonable impact by several decibels.

At last it is concluded that the track should be modelled with a longer distance than the size of the train. The reason is that there are more sleepers affected as the train is passing and therefore also the signal is coming from further distances.

6.4.2 Optimisation of soil stratification

As was mentioned in previous chapters, the stratification of soil medium plays an important role in the final response of of the ground. Since there is no proper data available, like direct boreholes provided with the laboratory tests or CPT data to find real soil parameters, the reference model soil layers and their properties are based mainly on engineering judgement. Therefore the impact of different soil stratification is also assessed. In comparison to the reference model, soil stratification is simplified only to two layers overlaying a half-space. As the water table is omitted the top layer is assumed with Poisson's ratio of $\nu = 0.3$. The Table 6.4 shows again three cases where the depth of the two top layers is varied up to a depth of 7 m. Moreover alternative three cases are added where the shear modulus of these layers is changed.

Tab. 6.4: Cases for depth and shear modulus variation.

		Layer 1	Layer 2	Layer 3
Case A(2)	G [MPa]	30 (17)	42 (59)	81
	d [m]	1	6	∞
Case B(2)	G [MPa]	30 (17)	42 (59)	81
	d [m]	3	4	∞
Case C(2)	G [MPa]	30 (17)	42 (59)	81
	d [m]	5	2	∞

The FRFs of all cases can be seen in Figures 6.8 and 6.9 also with the reference model described in table 6.2.

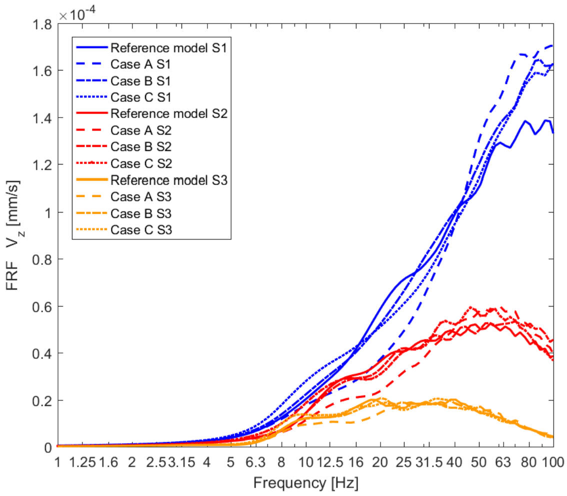

Fig. 6.8: FRFs for reference soil parameters and depth variation.

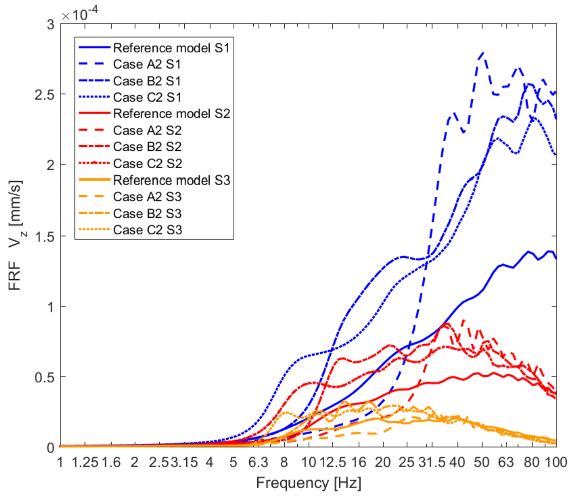

Fig. 6.9: FRFs for updated shear modulus and depth variation

In the first figure the depth variation is not that influential as the soil properties of both layers are very similar, mainly the values of the shear modulus. Therefore the alternative cases are also studied, where the shear modulus of top layer is significantly decreased and the second layer stiffness is increased. For the top layer this is estimated as a good assumption as the soil is more composed of organic material where low values for shear modulus are expected, instead of approximately medium sand properties obtained from the hammer test. It can be seen that the impact of depth variation is much larger between two significantly different soils.

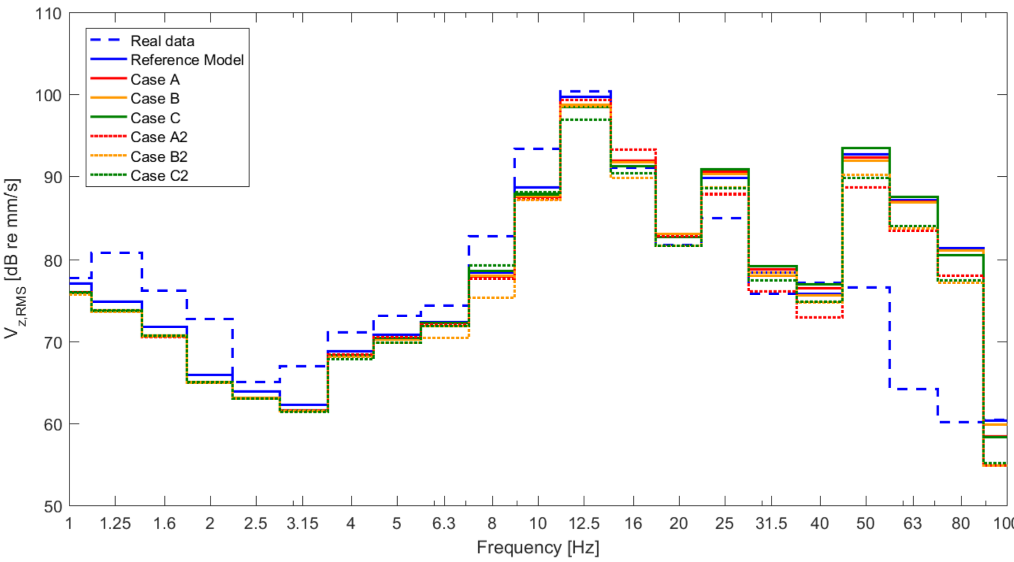

Fig. 6.10: Vertical response of 6 cases with G and depth variation at Sensor 2.

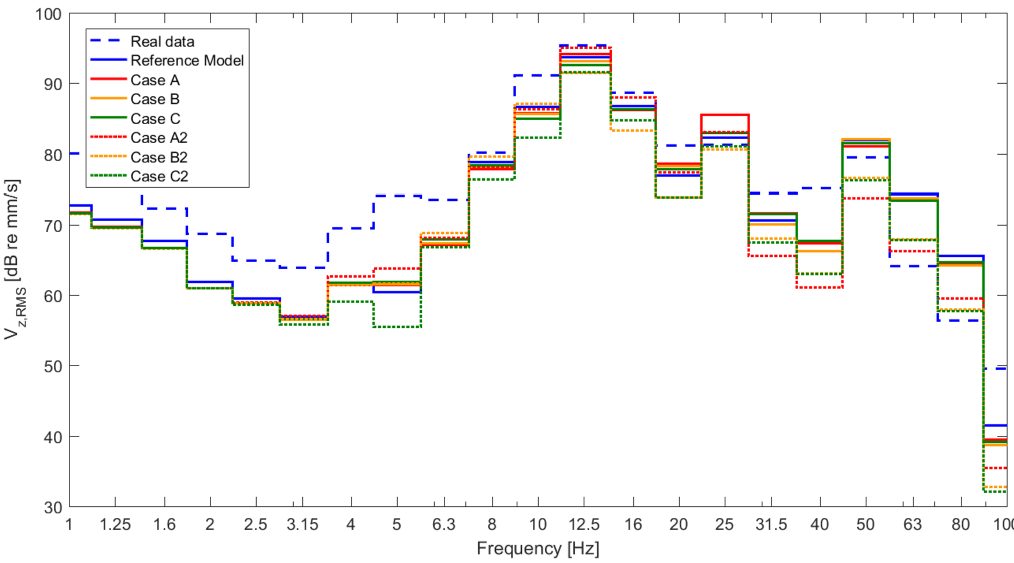

Fig. 6.11: Vertical response of 6 cases with G and depth variation at Sensor 3.

In the final response, see Figures 6.10 and 6.11, it can be seen that depth variation in cases A, B and C are almost irrelevant and all follow the behaviour of reference model. On the other hand, alternative cases influence the result significantly mainly in higher frequencies, which is due to the soft top soil which seems to prove better results. The proper stratification is almost impossible to define as at certain frequencies the best fit is achieved, but at the others the deviation just increase.

6.4.3 Optimization of soil by Loss factor

Loss factor is another parameter that has considerable influence in the response. This has more influence in high frequencies than in low frequencies. It is also known that a change in loss factor in bottom layers has little influence as it was demonstrated in Chapter 4. Then, the frequency response function is depicted for different loss factors changes in different layers. Figure 6.12 corresponds to η change for top layer while Figure 6.13 corresponds to second layer. The same procedure is applied for the bottommost layers. See Appendix E.1.

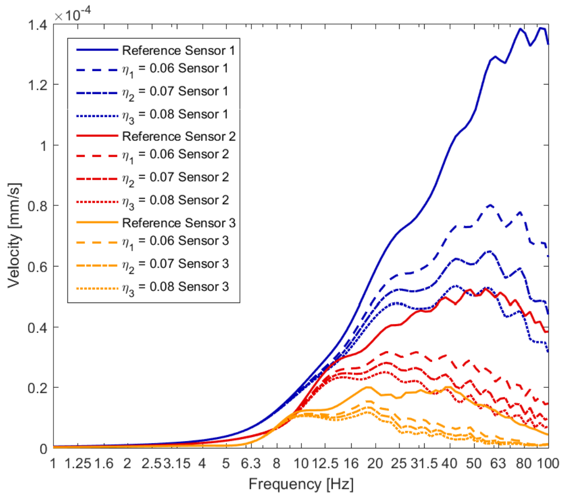

Fig. 6.12: FRFs for reference soil parameter and depth variation.

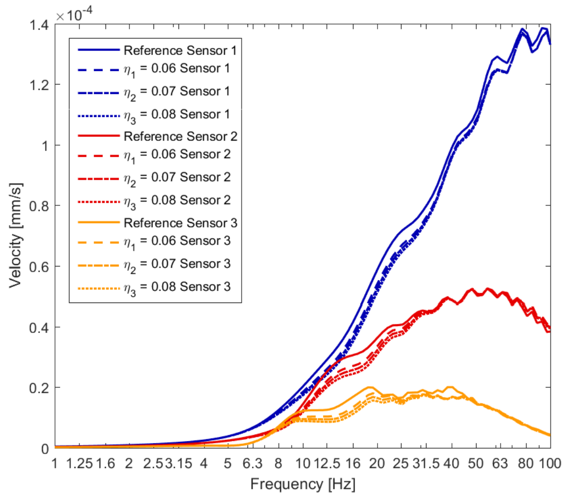

Fig. 6.13: FRFs for updated shear modulus and depth variation

As expected the change in loss factor for the bottom layers can be neglected and thus only the top layer is considered for the fitting.

Further, in order to see the effect of loss factor on the modelled response, this has been plotted for three different values, $\eta_1 = 0.06$, $\eta_2 = 0.07$ and $\eta_3 = 0.08$. The response from the model is plotted for different loss factors for Sensor 2 and Sensor 3. See Figures 6.14 and 6.15.

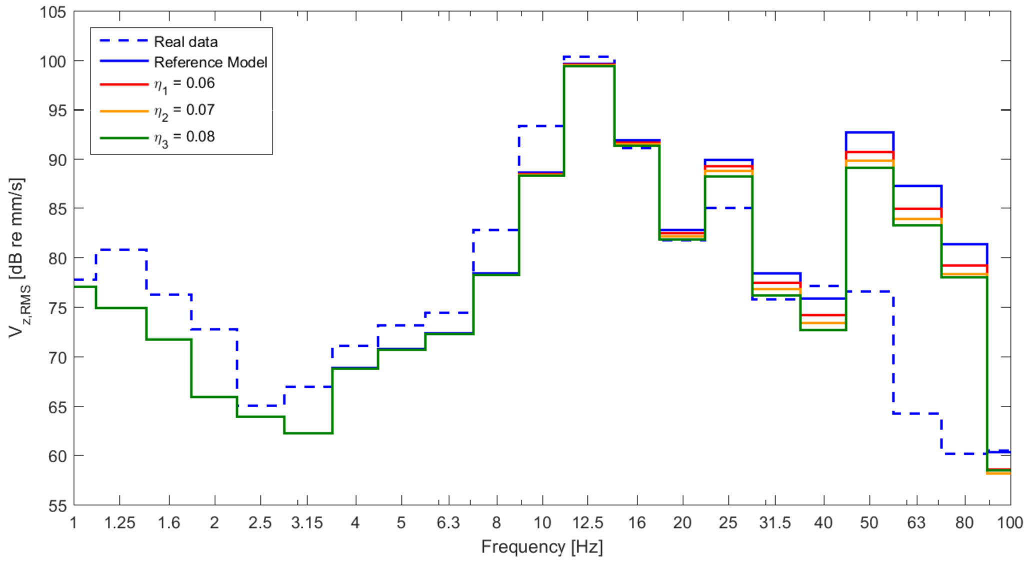

Fig. 6.14: Comparison of real response and different damping ratios for sensor 2.

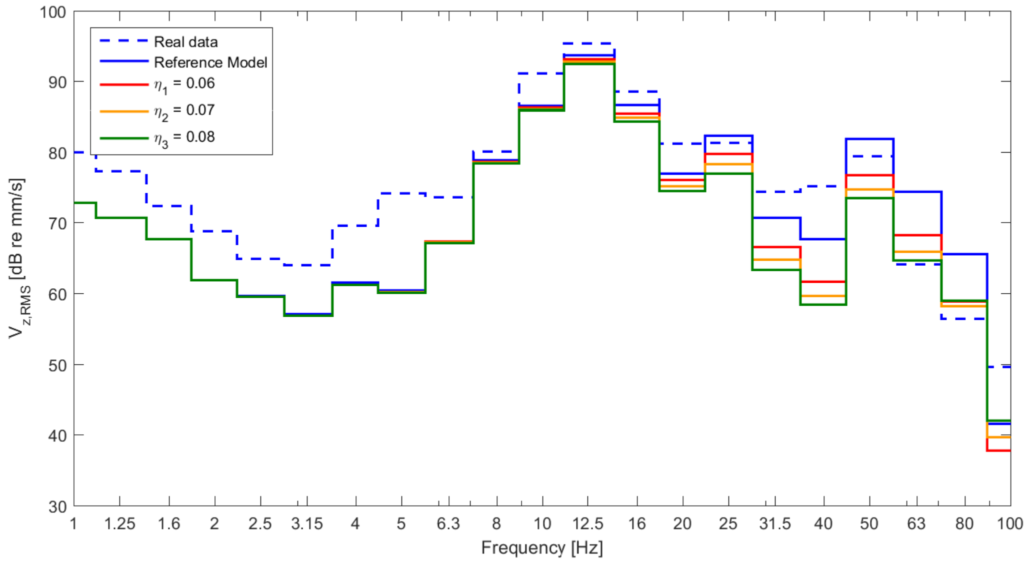

Fig. 6.15: Comparison of real response and different damping ratios for sensor 3.

As it can be seen for Sensor 2, the loss factor gives a closer fit to the real data for frequencies from 20 Hz to 40 Hz and for frequencies above 40 Hz the response gets closer but still some drift is present. For Sensor 3 on the other hand, the opposite is observed where frequencies in the range of $20-40$ Hz show some drift while for frequencies higher than 40 Hz there is a good match with the real data . Notice that this is the case for high loss factors, that is, $\eta_1 = 0.06$ and $\eta_3 = 0.08$. Finally, it can be said that the damping of the soil on site is high, probably close to $\eta = 0.08$.

6.5 Evaluation of differences in the response due to the track

When observing the measurements for all the different trains recorded, there can be seen several significant differences at certain frequencies between north bound trains and south bound trains. These variations in the response may be due to some differences in the track since they are not perfectly identical and also due to the distance from the sensor.

The idea here is to simulate the different directions and see if the differences in the response are due to the distance of the tracks or also due to some other factor that alters the response.

In Chapter 5, Figures 5.16 and 5.17 show differences in the response of north bound trains and south bound trains. Train 1 and train 8 are depicted in Figure 6.16 and 6.17 for Sensor 1 and Sensor 2 respectively. Further, in order to see what factor affect this difference in the response, the FRF of the modelled response for both directions has been illustrated in Figure 6.18 for both sensors.

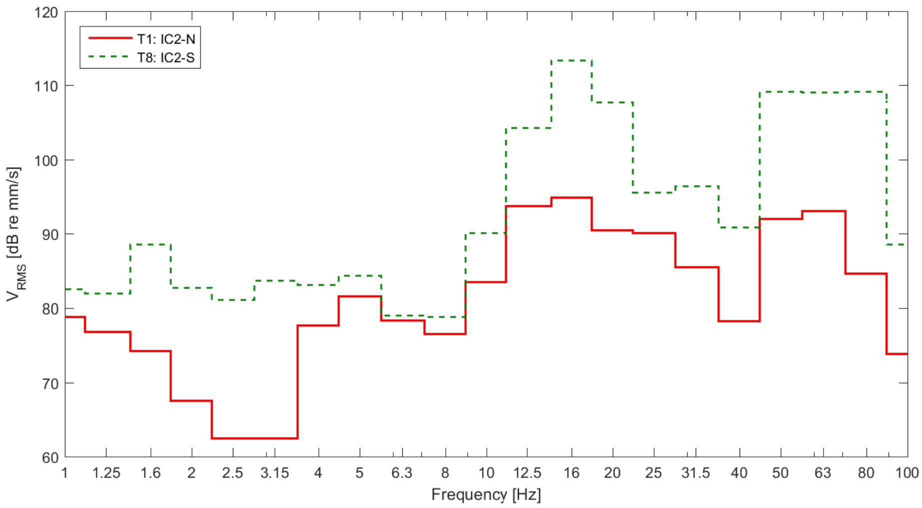

Fig. 6.16: Comparison of train 1 and train 8 response in octave bands for Sensor 1.

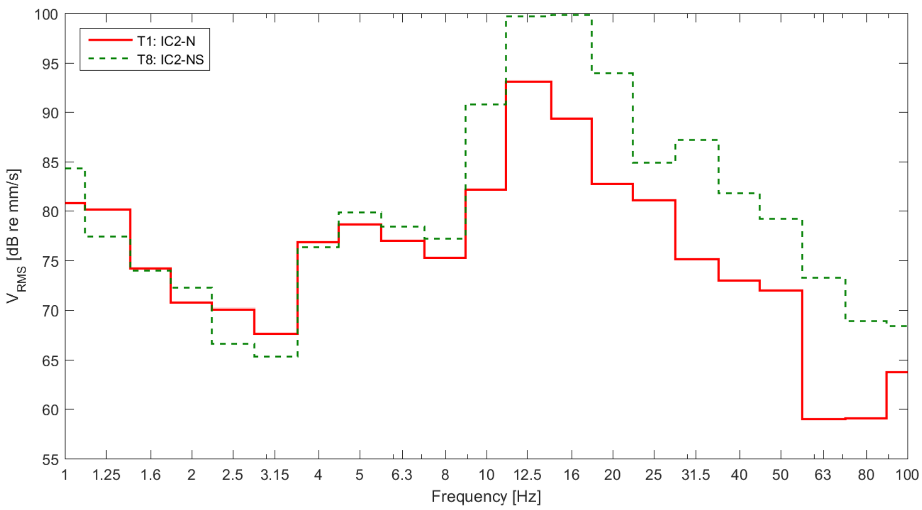

Fig. 6.17: Comparison of train 1 and train 8 response in octave bands for Sensor 2.

Both Figures 6.16 and 6.17 show a drift in the response that starts at frequencies around 10Hz. Moreover, another drift can be observed occurring at low frequency of range $1-5$Hz at Sensor 1.

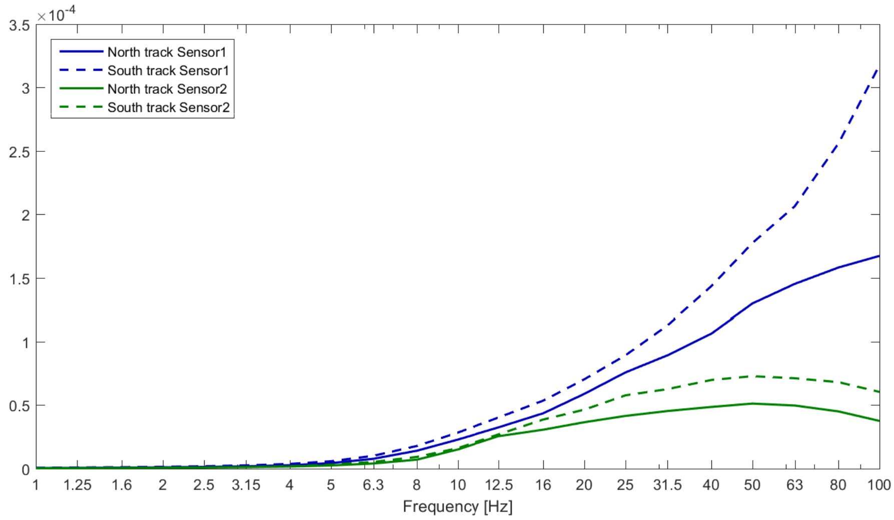

Fig. 6.18: Comparison of FRF for North and South bound trains.

In Figure 6.18, the FRF response also shows some drift starting at frequency around 10 Hz for both sensors. Thus, it can be concluded that this difference is due to the distance from the tracks to the sensors. On the other hand, the modelled response at Sensor 2, see Figure 6.17, shows no changes at low frequencies while Sensor 1 does. This may be due to some resonance occurring at that location since Sensor 2 is not measuring such a response for those low frequencies.

6.6 Final design of the model on site

The final model of the soil is designed based on the previous sections. Table 6.5 shows the final soil parameters chosen. Moreover, the load was applied throughout the length of $L = 90$ m with total number of observation points $n = 76$.

Tab. 6.5: Soil properties of reference model.

	Shear Modulus G [MPa]	Poisson's ratio $\nu[-]$	Density ρ [kg/m^3]	Loss factor $\eta[-]$	Depth h [m]
Layer 1	17	0.3	1900	0.06	1
Layer 2	30	0.4	2000	0.04	6
Layer 3	81	0.4	2100	0.04	-

A top soft soil layer with a depth of 1 m is assumed and high loss factor which was desired to lower down the response at high frequencies at Sensor 2. By elongating the train there is little rise of response achieved between octave bands $6.3-10$ Hz.

In Figures 6.19 and 6.20 one can see the final behaviour of the model in comparison to reference model and the measurements of three relevant IC3 trains located on the north bound. Moreover, three different force spectra based on each train are created.

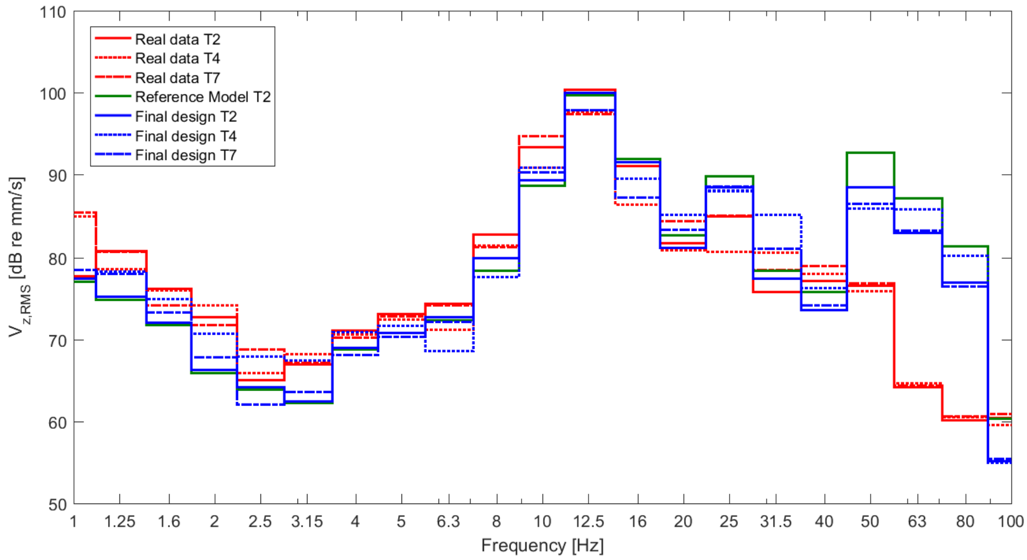

Fig. 6.19: Vertical response of real and modelled trains at Sensor 2.

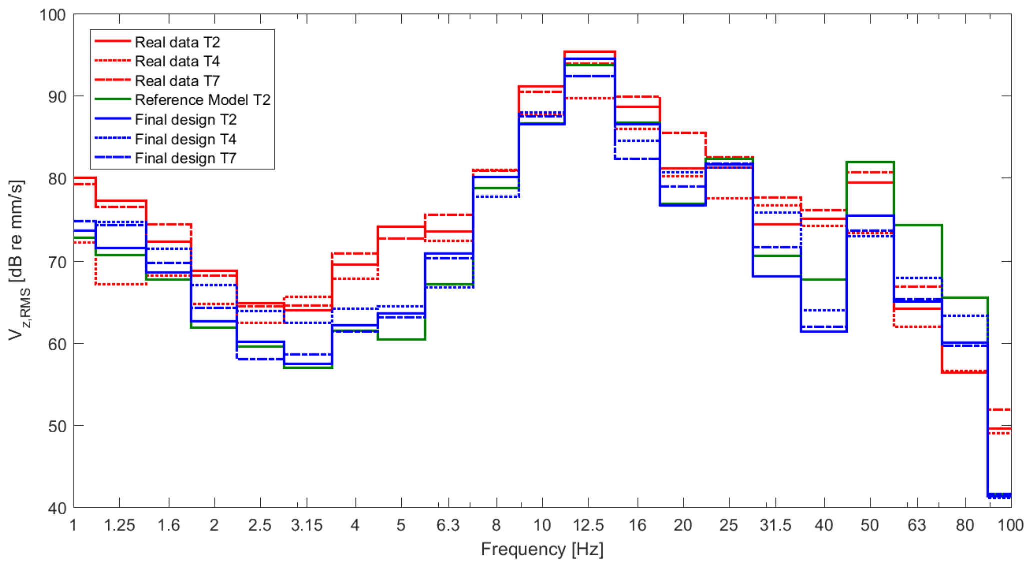

Fig. 6.20: Vertical response of real and modelled trains at Sensor 3.

As both figures show, the final model of the soil fits better with the real response overall. For Sensor 2, the response shows some drift at high frequencies but still closer than the reference case and for same sensor also the new model represents a better estimation for all the domain of frequencies apart from some fluctuation at frequencies of 30 – 45 Hz where the reference gives better fit.

Generally it is almost impossible to get a proper fit for a model as there are many variables which are affecting each other. Another main problem is that the force spectra are based on Sensor 1 and therefore at certain frequencies will always show higher response, mainly from 50 to 100 Hz, where the response is significantly higher at the closest sensor.

Finally, the fitting of the modelled response has been quantified in terms of RMS error in order to have an idea of the precision of the fits. Table 6.6 shows the RMS between the real and modelled response for the three trains shown previously. Then train 2 is also compared to the reference case. Note that the reference case was calculated based on this train.

Tab. 6.6: Deviation of the models in terms of RMS.

Trains	Sensor 1		Sensor 2	
	RMS(Real/Model)	RMS(Real/Ref)	RMS(Real/Model)	RMS(Real/Ref)
T2	6.768	8.129	6.042	6.661
T4	7.351	-	4.982	-
T7	6.688	-	6.621	-

6.7 Summary

The purpose of this chapter was to implement semi-analytic model on the real case. Several steps were performed in order to find the best fit of the model to the real soil behaviour.

- First the **soil stratigraphy** and **parameters** were estimated based on boreholes located close to the area of measurements and also by processing the data from hammer test. Crude value of shear modulus was estimated based on the propagation velocity of the Rayleigh wave.

- The **track is modelled in order to imitate the load application** from the passing train. The method used in this report was to create only one single unitary load, but instead of "catching" response at one location, several observation points were created in the line of certain distance and spans between the points. The total response was calculated as a RMS value.

- **Force spectrum** is calculated so the actual loads from the train could be implemented in the model, instead of unit load. After this, the response at given locations could be obtained by multiplying the force spectrum by the frequency response functions of model at chosen points, in this case Sensor 2 and 3.

- **The optimization of the model** was also provided where the new soil stratigraphy and their properties were assigned and their variation was assessed and compared to reference model and real responses.

- Moreover an **analysis of the track location** is performed. This is done due to the reason that the measured response showed no impact at certain octave bands. It was found in frequency response functions that for long waves, meaning low frequencies, there is no difference between track location, where at high frequencies when the waves are shorter it influences the overall response.

7 | Discussion and conclusions

The use of the semi-analytical model developed by Lars Andersen and Paulius Bucinskas made it possible to investigate the propagation of waves in the soil medium and the impact that they can have on the surrounding area. It was found to be a very practical model, which allows the user to simulate a test based on a good representation of the real properties of the soil in a medium and the desired source of ground-borne vibrations.

In order to test and verify the efficiency of the model, first a homogeneous half-space was considered where the waves were generated by applying a vertical source and the response was measured in the vertical direction at distances of $10R$, $25R$ and $50R$ away from the point of load application. Secondly, the media was simulated as a layered half-space. In both cases it was observed that the highest influence in the response measured in the surface at all distances was mainly due to the Rayleigh waves which would fit nicely with the theory of waves propagation.

Furthermore, a parameter study was performed for the shear modulus, Poisson's ratio, loss factor and mass density for both half-space and for the layered media to find the influence that each parameter has on the response. In addition to the half-space, for the layered media the depth of the top layer is considered in the study. The results showed that the shear modulus is the most influential parameter, having the highest impact in the amplitude of the dynamic amplification. On the other hand, Poisson's ratio would change the shape of the response especially at resonance frequency for high values of Poisson's ratio corresponding to a saturated soil. The loss factor is another important parameter which tends to affect more the influence at higher frequencies and also over distance. At last, the mass density of the material seemed like the only parameter which has the lowest influence.

The experimental test was performed in order to validate the model on the real case. Several train induced vibrations were measured by use of geophones at the given site location. A large variation was observed between the different trains which was assumed to be the consequence of specific parameters, properties and irregularities of the trains. It was also noticed that the direction of the train plays a major role at close distances as the relative distance of the Sensor 1 from north bound track is significantly different than the south one. The difference in response drops down for the other two sensors as the ratio between two relative distances of the track is smaller. Moreover in case of very long waves, octave bands $1-6.3\,\mathrm{Hz}$, the relative distance is irrelevant when the sensors are located further from the tracks.

To be able to implement the real measurements in the model, first the site investigation had to be performed in order to estimate the soil stratigraphy and parameters of the reference model. This is the source of first uncertainties where there was no proper data available, meaning that the parameters had to be assumed based on the engineering judgement as there were only few boreholes located quite far away from the site. Moreover hammer test could only be used to obtain the Rayleigh waves which was not the purpose of the procedure and several factors affecting the behaviour of waves were neglected. Nevertheless, it provided the crude estimation for the shear modulus of top layer.

Later on the procedure of the track modelling was described, where the method of "reversed" loads was applied in order to imitate the rail sleepers through which the vibrations induced by the train are propagating into the soil medium. Here it was concluded that the length of the force application should be longer than the actual size of the train.

Once the soil properties were defined and the track was modelled the reference model behaviour could be evaluated where the force function was derived from the real data. It has to be noted that this function was based on Sensor 1 where the real data of the ground response exhibited extremely high values at upper octave bands which are then significantly affecting the behaviour of other sensors.

Furthermore, optimisation of the input parameters was performed in order to simulate the real behaviour. Here it was found that changing the soil parameters can only influence certain octave bands, while at very low frequencies the change is almost insignificant. It was further observed that as soon as the parameters fit one sensor the accuracy in the second one drops. This was mainly the case at higher octave bands when there was high damping implemented to the soil in order to match with Sensor 2, leading to a significantly lower response in Sensor 3 than the real measurements.

The reason for this behaviour probably lies in the uncertainty of soil properties, where it is assumed that there are horizontally layered homogeneous media which is in this case it may not be the best assumption. Also the measurements were performed over a distance of 50 m and the soils in this case might vary a lot. It was also observed that while digging the holes for Sensor 1 and 2 the top soil was very easy to remove, while on the other hand at the place of Sensor 3 it was much stiffer and harder to remove. This might lead to the conclusion that the loss factor in between first two sensors is much higher than between the second and last sensor.

All in all, it can be said that the semi-analytic model provides a reasonable approximation of the vibration levels measured at the site. Although, this can be further improved if the there is accurate data of the soil properties in the site of reference.

Bibliography

Achenbach, 1973. Jan Achenbach. *Wave Propagation in Elastic Solids*. North-Holland Publishing Company, 1973.

Andersen, 2006. Lars Andersen. *Linear Elastodynamic Analysis*. ISSN 1901-7286, Lecture Notes. Aalborg University, 2006.

Andersen and Clausen, 2011. Lars Andersen and Johan Clausen. *Efficient Modelling of Wind Turbine Foundations*. INTECH Open Acess Publisher, 2011. ISBN 978-953-307-508-2. URL `https://www.intechopen.com/books/howtoreference/fundamental-and-advanced-topics-in-wind-power/efficient-modelling-of-wind-turbine-foundations`.

Andersen and Clausen, 2008. Lars Andersen and Johan Clausen. *Impedance of surface footings on layered ground*. Computers & Structures, 86(1–2), 72 – 87, 2008.

Andersen, 2010. Lars Vabbersgaard Andersen. *Vibrationer fra jernbane til den ny Femern Bælt forbindelse*, Aalborg Universitet, Institut for Byggeri og Anlæg, Sektionen for Bygningsmekanik, 2010.

Banedanmark, 2016. Banedanmark. *Network Statement 2016*. no. 14-06331, pages 1–47, 2016.

Cadforum, 2008. Cadforum. *Train block - Elevation view*, 2008. URL `http://www.cadforum.cz/catalog_en/block.asp?blk=2277`.

Damgaard et al., 2015. M. Damgaard, L. V. Andersen, L. B. Ibsen, H. S. Toft and J. D. Sørensen. *A probabilistic analysis of the dynamic response of monopile foundations: Soil variability and its consequences*. Probabilistic Engineering Mechanics, 41, 46–59, 2015. URL `www.scopus.com`.

Det Norske Veritas, 2012. Det Norske Veritas. *Statistical Representation of Soil Data*. `http://www.dnv.com`, 2012.

Foti, 2000. Sebastiano Foti. *Multistation Methods for Geotechnical Characterization using Surface Waves*. 2000.

GEUS, 2000. GEUS. *Geological Survey of Denmark and Greenland - Well Database*, 2000. URL `http://data.geus.dk/geusmap/?mapname=jupiter#zoom=14.81817170415501&lat=6309528.4672992&lon=552699.64597302&visiblelayers=Topographic&filter=&layers=jupiter_boringer_ws&mapname=jupiter&filter=&epsg=25832&mode=map&map_imagetype=png&wkt=`.

Hall, 2003. Lars Hall. *Simulations and analyses of train-induced ground vibrations in finite element models*. Soil Dynamics and Earthquake Engineering, 23(5), 403 – 413, 2003.

Haskell, 1953. Norman A Haskell. *The dispersion of surface waves on multilayered media.*, volume 43. Seismological Society of America, 1953.

Holm and Riis, 2014. Søren Holm and Andreas Riis. *Dynamic Amplification of Deformations in Railways due to High-Speed Traffic on Soft Ground*. 2014.

Hons and Stewart, 2006. Michael S Hons and Robert R Stewart. *Transfer functions of geophones and accelerometers and their effects on frequency content and wavelets*. CREWES Res. Rep, 18, 1–18, 2006.

ISO, 1997. ISO. *Mechanical vibration and shock — Evaluation of human exposure to whole-body vibration — Part 1: General requirements*. International Organisation for Standardisation, 1997. Technical Committee : ISO/TC 108/SC 4.

Jensen et al., 2013. Bjarne Chr. Jensen, Gunner Mohr, Asta Nicolajsen, Bo Mortensen, Henrik Bygbjerg, Lars Pilegaard Hansen, Hans Jørgen Larsen, Svend Ole Hansen, Dirch H. Bager, Eilif Svensson, Ejnar Søndergaard, Carsten Munk Plum, Hilmer Riberholt, Lars Zenke Hansen, Kaare K. B. Dahl, Henning Larsen, Per Goltermann, Jørgen S. Steenfelt, Carsten S. Sørensen and Werner Bai. *Teknisk Ståbi*. ISBN: 978-87-571-2775-1. Nyt Teknisk Forlag, 2013.

Jernbanen.dk, 2017. Jernbanen.dk. *DSB lyntog og togsæt*, 2017. URL `http://www.jernbanen.dk/lyntog.php?typenr=5`.

Jones et al., 2002. Allen L Jones, Steven L Kramer and Pedro Arduino. *Estimation of Uncertainty in Geotechnical Properties for Performance-Based Earthquake Engineering*. Pacific Earthquake Engineering Research Center, College of Engineering, University of California, 2002.

Kramer, 1996. Steven L Kramer. *Geotechnical Earthquake Engineering*. ISBN: 0-13-374943-6. Prentice-Hall, Inc., 1996.

Krylov and Ferguson, 1994. Victor Krylov and Colin Ferguson. *Calculation of low-frequency ground vibrations from railway trains*. Applied Acoustics, 42(3), 199 – 213, 1994. URL `http://www.sciencedirect.com/science/article/pii/0003682X94901090`.

Krylov, 1995. Victor V. Krylov. *Generation of ground vibrations by superfast trains*. Applied Acoustics, 44(2), 149 – 164, 1995. URL `http://www.sciencedirect.com/science/article/pii/0003682X9591370I`.

Look, 2014. Burt G . Look. *Handbook of Geotechnical Investigation and Design Tables*. ISBN: 978-1-315-81323-3. CRC Press, 2014.

maps, 2017. Google maps. *Google maps*, 2017. URL `https://www.google.dk/maps/@56.926644,9.8674951,450m/data=!3m1!1e3?hl=sk`.

Recipes, 2004. Acoustical Porous Material Recipes. *Octave and one-third octave frequency bands*, 2004. URL `http://apmr.matelys.com/Standards/OctaveBands.html`.

Semblat and Pecker, 2009. Jean Françsois Semblat and Alain Pecker. *Waves and Vibrations in Soils: earthquakes, traffic, shocks, construction works*, 2009.

Sigicom, 2013a. Sigicom. *INFRA V12, V11, V12 Manual*, 2013. Manual provided with the device.

Sigicom, 2013b. Sigicom. *INFRA Master Manual*, 2013. Manual provided with the device.

Sørensen, 2004. Jones Dalsgaard Sørensen. *Notes in Structural Riliability Theory and Risk Analysis*. Aalborg University, 2004.

Thomson. William T Thomson. *Transmission of elastic waves through a stratified solid medium*.

Zapfe et al., 2009. Jeffrey A Zapfe, Hug Saurenman and Sanford Fidell. *Ground-borne noise and vibration in buildings caused by rail transit*. ISBN 978-0-309-43003-6. Transit Cooperative Research Program, Transportation Research Board of the National Academies, 2009.

A | Theory of probabilistic approach

A.1 Correlation coefficient

The correlation coefficient is a measure of linear dependence between two stochastic variables. If the two stochastic variables are defined as X_1 and X_2 which can represent any two of the material properties i.e. G and ρ, the correlation coefficient between the two is given by:

$$\rho_{x_1,x_2} = \frac{Cov[X_1,X_2]}{\sigma_1 \sigma_2} \qquad where \qquad -1 \leq \rho_{x_1,x_2} \leq 1 \tag{A.1}$$

For $\rho_{x_1,x_2} = 0$ the variables are considered to be uncorrelated. In Equation A.1, σ_1 and σ_2 represent the standard deviations of the stochastic variables while $Cov[X_1,X_2]$ is the covariance between the two, defined by:

$$Cov[X_1,X_2] = E[(X_1-\mu_1)(X_2-\mu_2)] \tag{A.2}$$

It can be seen that the covariance of one stochastic variable corresponds to the variance, given by:

$$Cov[X_1,X_1] = Var[X_1] = \sigma_1^2 \tag{A.3}$$

When more than two stochastic variables are considered i.e. more soil properties, the covariance is present by a matrix for the stochastic variables of $X = (X_1,X_2...X_n)$, [Sørensen, 2004], which is given by:

$$\mathbf{C} = \begin{bmatrix} Var[X_1,X_1] & Cov[X_1,X_2] & \cdots & Cov[X_1,X_n] \\ Cov[X_1,X_2] & Var[X_2,X_2] & \cdots & Cov[X_2,X_n] \\ \vdots & \vdots & \ddots & \vdots \\ Cov[X_1,X_n] & Cov[X_2,X_n] & \cdots & Var[X_n,X_n] \end{bmatrix} \tag{A.4}$$

Therefore the correlation coefficient matrix becomes:

$$\boldsymbol{\rho} = \begin{bmatrix} 1 & \rho_{x_1,x_2} & \cdots & \rho_{x_1,x_n} \\ \rho_{x_1,x_2} & 1 & \cdots & \rho_{x_2,x_n} \\ \vdots & \vdots & \ddots & \vdots \\ \rho_{x_1,x_n} & \rho_{x_2,x_n} & \cdots & 1 \end{bmatrix} \tag{A.5}$$

Th correlation coefficient matrix has to be positive definite.

A.2 The log-normal distribution

The distribution function is normally described by its mean value and standard deviation, however in this procedure we will make use of the coefficient of variation, which represents the ratio of the two before mentioned parameters, $CoV = \sigma/\mu$. The reason behind this is due to the fact that the variables can be widely spread depending on the expected value, and by using the coefficient of variation instead of the standard deviation this dispersion can be controlled. The log-normal cumulative distribution function that relates the sets of input variables is described as follows:

$$F_X(x) = \Phi(\frac{\ln x - \mu_y}{\sigma_y}) \tag{A.6}$$

where,

$$\sigma_y = \sqrt{\ln(CoV^2+1)} \approx CoV, \qquad \text{Standard deviation} \tag{A.7}$$

$$\mu_y = \ln\mu - \frac{1}{2}\sigma_y^2 \approx \ln\mu, \qquad \text{Expected value} \tag{A.8}$$

Note that $\mu \neq \mu_y$ and $\sigma \neq \sigma_y$!

The probability density functions of the density and the shear wave velocity obtained after randomization for soft, medium and hard sand can be seen in Figures A.1 and A.2.

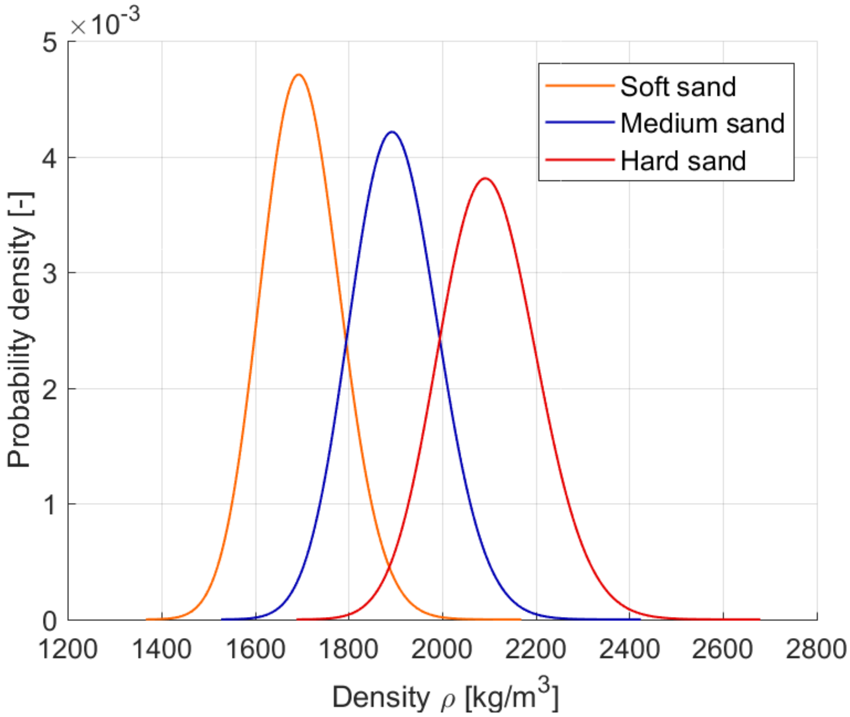

Fig. A.1: Probability density functions of the density for soft, medium and hard sand.

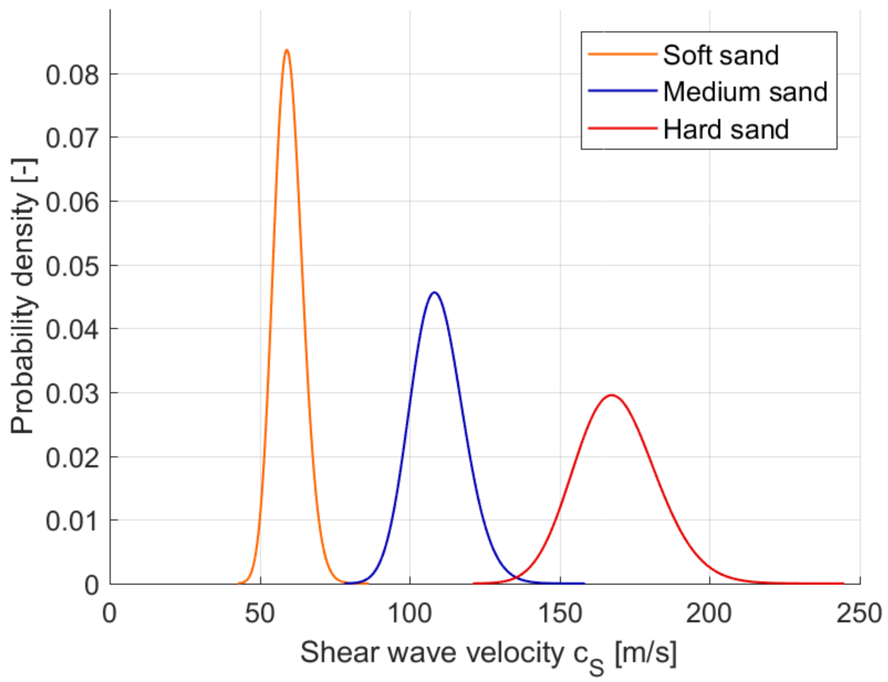

Fig. A.2: Probability density functions of the shear wave velocity for soft, medium and hard sand.

B Parameter study for the bottommost half-space

B.1 Sensitivity related to shear modulus

Here the effect of changing the shear modulus in the bottommost half-space is studied. The properties of the top layer are kept constant while the shear modulus is varied by first making the half-space stiffer than the top layer, and secondly by considering a softer half-space. The values considered in this anaylsis are accumulated in Table 4.2.

Tab. B.1: Shear modulus for the case of stiff and soft bottommost half-space.

	Stiff half-space	Soft half-space
	G [MPa]	
Top layer	31.21	31.21
Half-space	60.65	8.31
	82.39	16.27

The two cases are compared to a reference line corresponding to a half-space with the same material properties as described in Table 4.1. The results from this analysis are shown in Figure B.1.

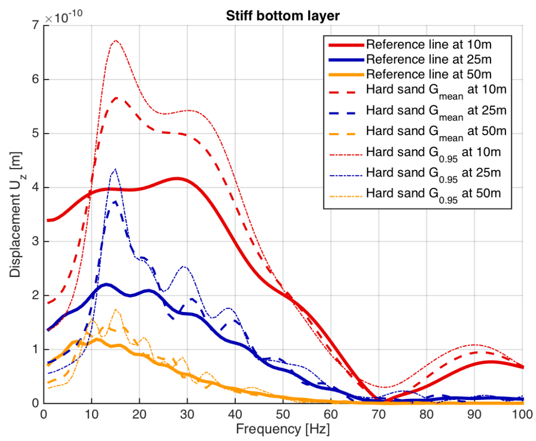

(a) Response of the layered media for stiff underalying half-space.

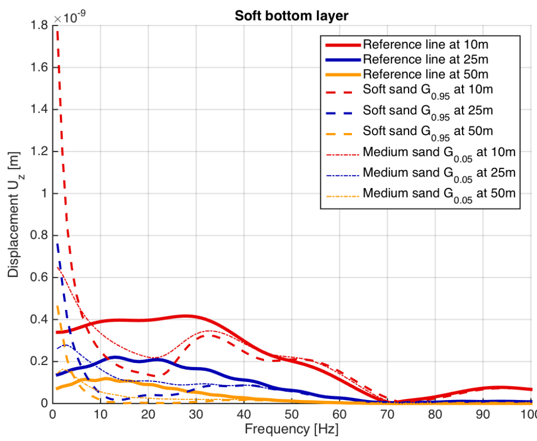

(b) Response of the layered media for soft underlaying half-space.

Fig. B.1: Sensitivity of the shear modulus in the bottommost half-space.

B.2 Sensitivity related to mass density

Material properties accumulated in Table B.2 are used as the reference cases to find the influence in the response of the mass density, loss factor, Poisson's ratio and layer's depth , for varying material properties in the bottommost half-space.

Tab. B.2: Soil properties for reference observations.

	Shear Modulus G [MPa]	Poisson's ratio ν	Density ρ [kg/m^3]	Loss factor η	Depth h[m]
Top layer	32.629	0.3	2000	0.04	4
Soft half-space	16.863	0.3	2000	0.04	4
Stiff half-space	80.806	0.3	2000	0.04	∞

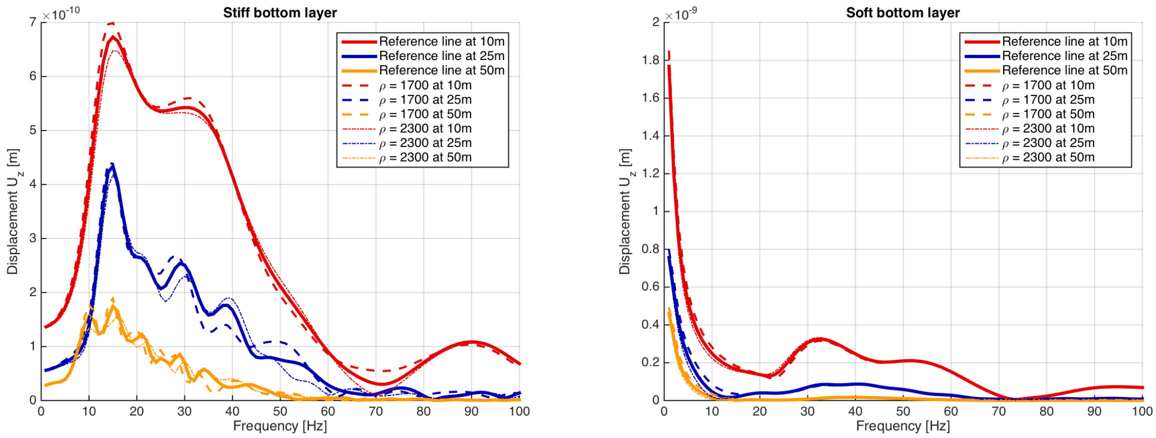

(a) Response of the layered media for stiff underalying half-space.

(b) Response of the layered media for soft underlaying half-space.

Fig. B.2: Sensitivity of the mass density in the bottommost half-space.

B.3 Sensitivity related to loss factor

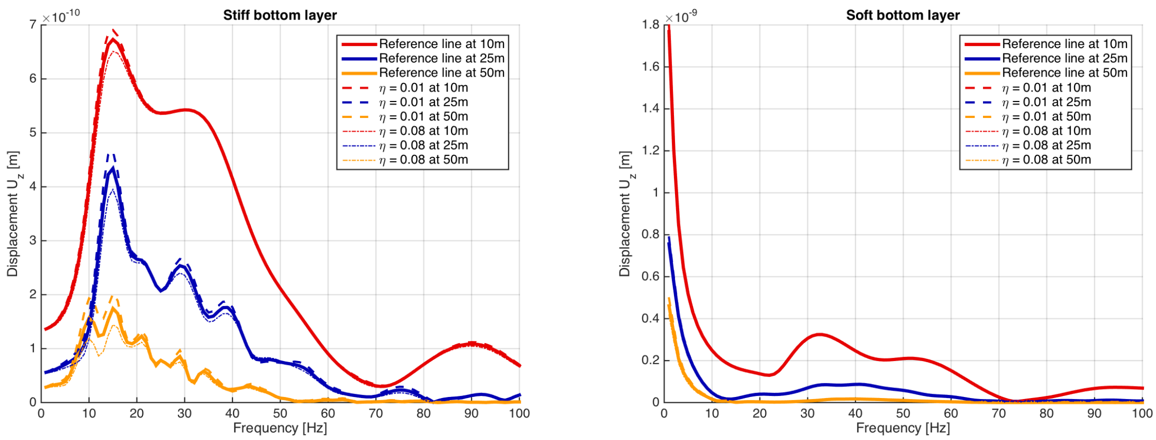

(a) Response of the layered media for stiff underalying half-space.

(b) Response of the layered media for soft underlaying half-space.

Fig. B.3: Sensitivity of the loss factor in the bottommost half-space.

B.4 Sensitivity related to Poisson's ratio

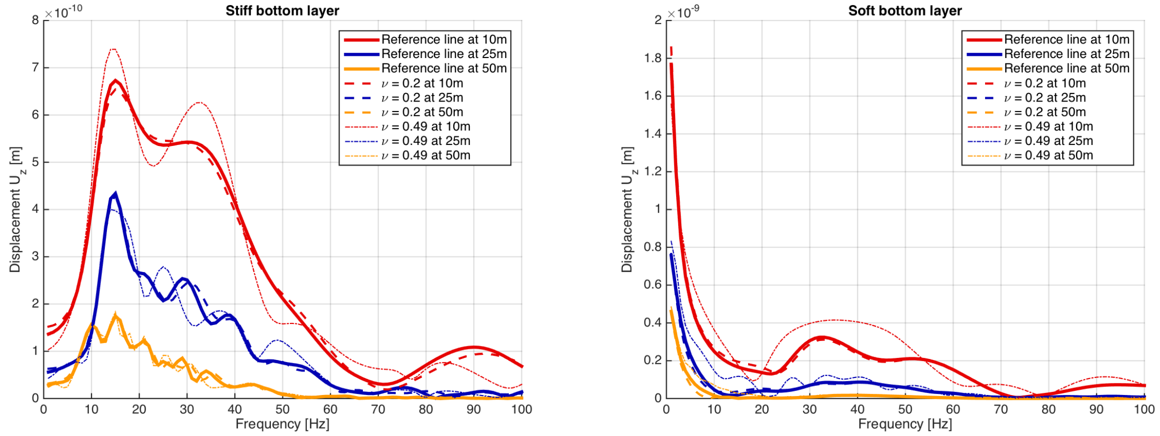

(a) Response of the layered media for stiff underalying half-space.

(b) Response of the layered media for soft underlaying half-space.

Fig. B.4: Sensitivity of Poisson's ratio in the bottommost half-space.

B.5 Depth of the top layer

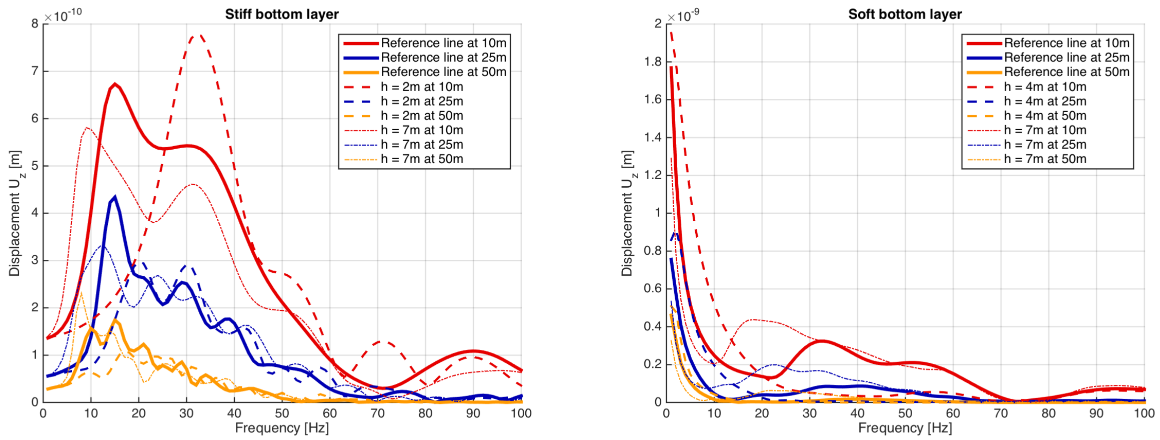

(a) Response of the layered media for stiff underlaying half-space.

(b) Response of the layered media for soft top layer.

Fig. B.5: Influence of the top layer depth for varying strength of the bottommost half-space.

C | Raw data presentation

Here is presented the measured data in both time and frequency domain for each train in vertical direction.

Train 1

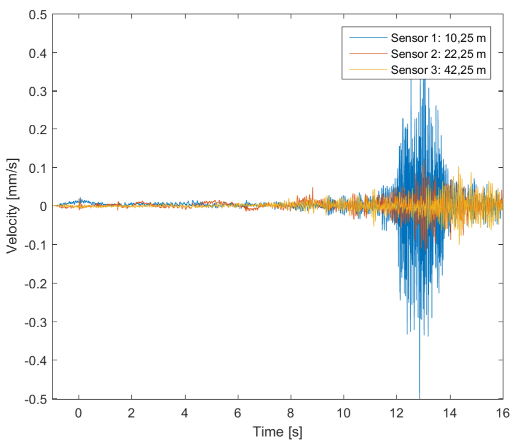

Fig. C.1: Response of train in time domain.

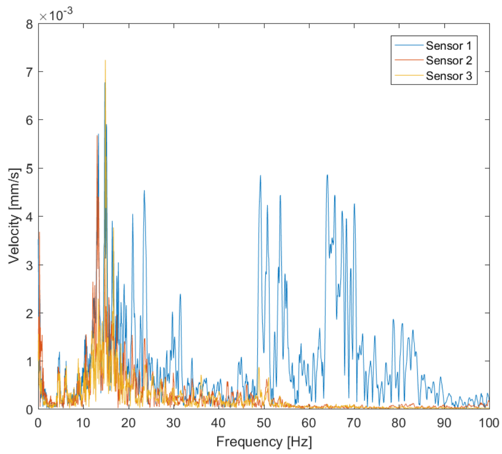

Fig. C.2: Response of train in frequency domain.

Train 2

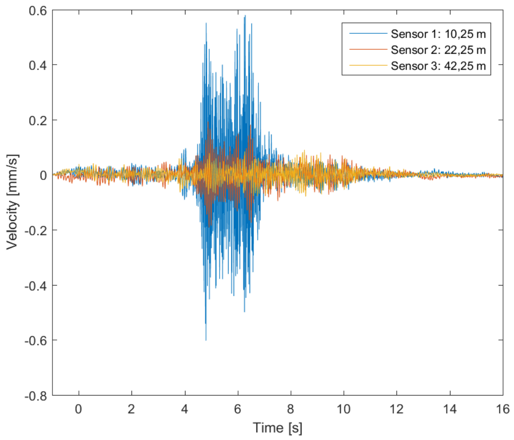

Fig. C.3: Response of train in time domain.

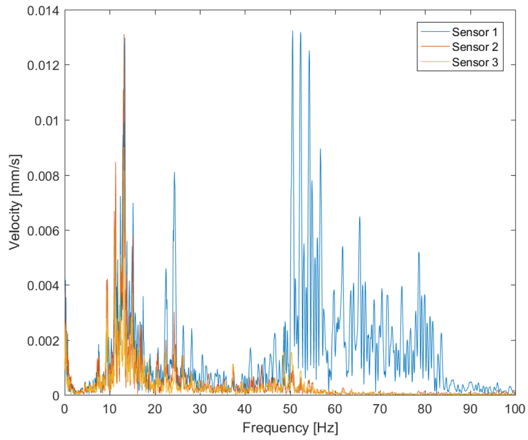

Fig. C.4: Response of train in frequency domain.

Train 3

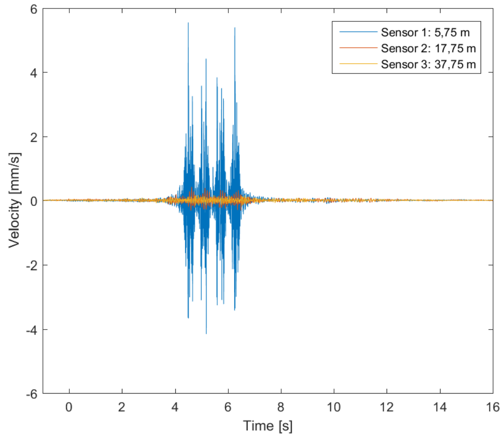

Fig. C.5: Response of train in time domain.

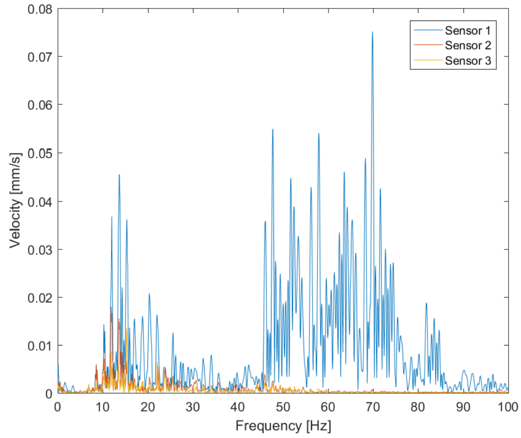

Fig. C.6: Response of train in frequency domain.

Train 4

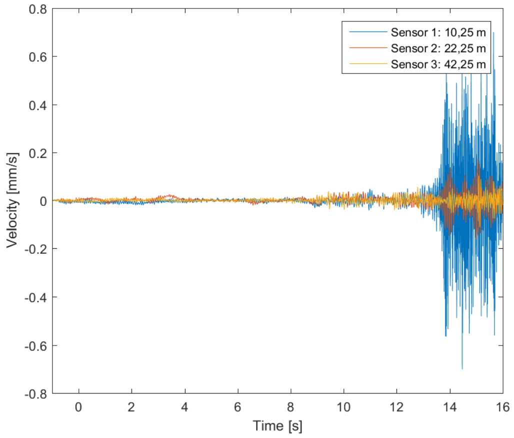

Fig. C.7: Response of train in time domain.

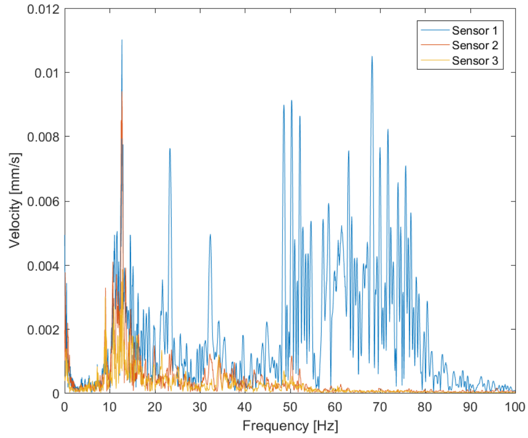

Fig. C.8: Response of train in frequency domain.

Train 5

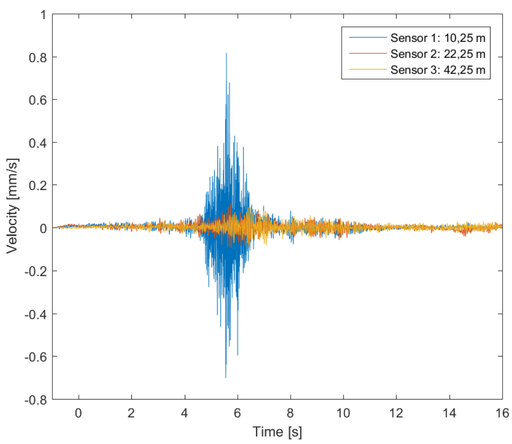

Fig. C.9: Response of train in time domain.

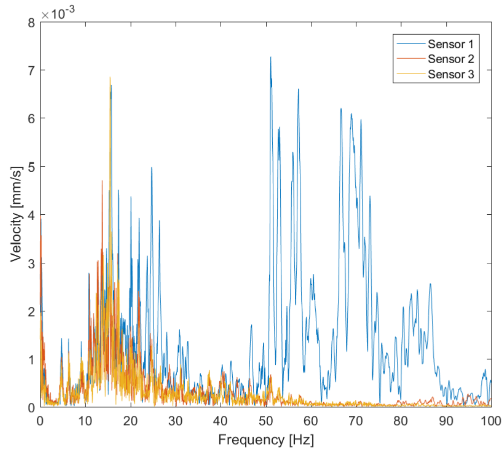

Fig. C.10: Response of train in frequency domain.

Train 6

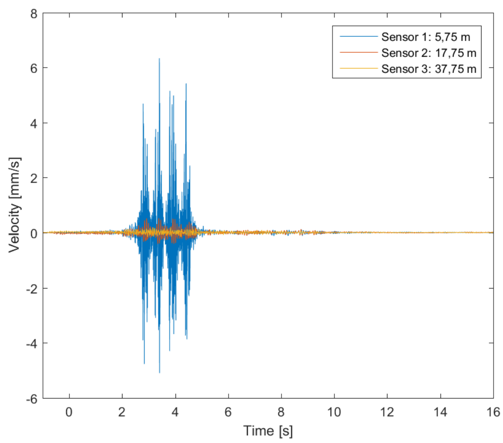

Fig. C.11: Response of train in time domain.

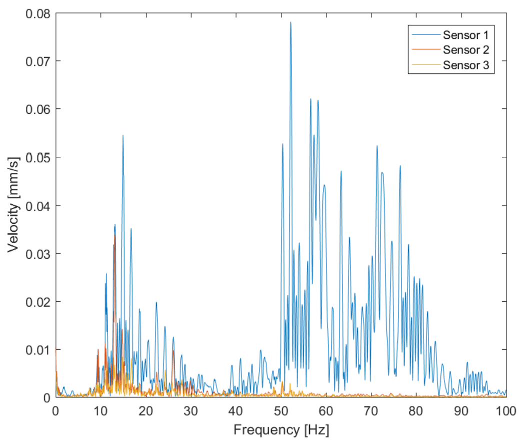

Fig. C.12: Response of train in frequency domain.

Train 7

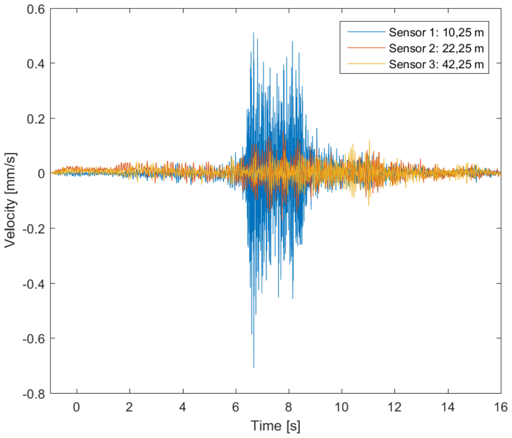

Fig. C.13: Response of train in time domain.

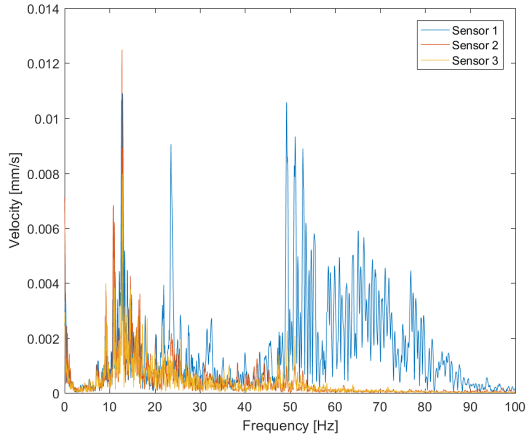

Fig. C.14: Response of train in frequency domain.

Train 8

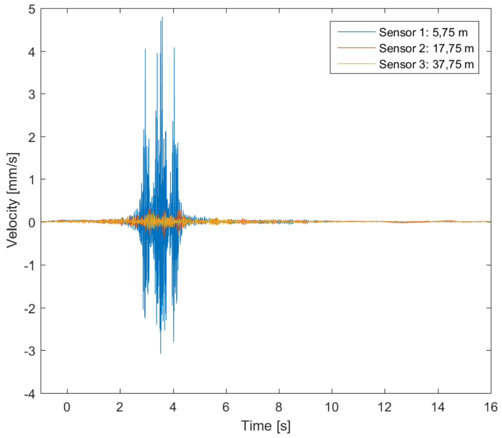

Fig. C.15: Response of train in time domain.

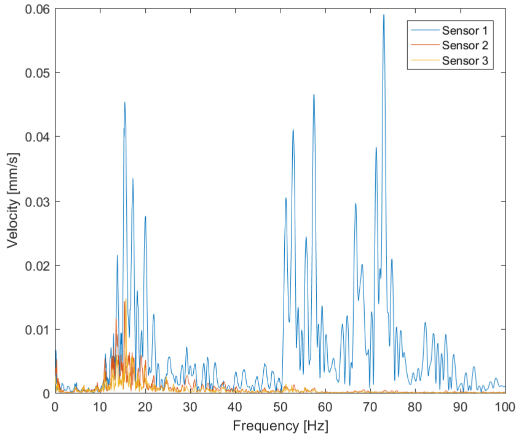

Fig. C.16: Response of train in frequency domain.

D | Boreholes

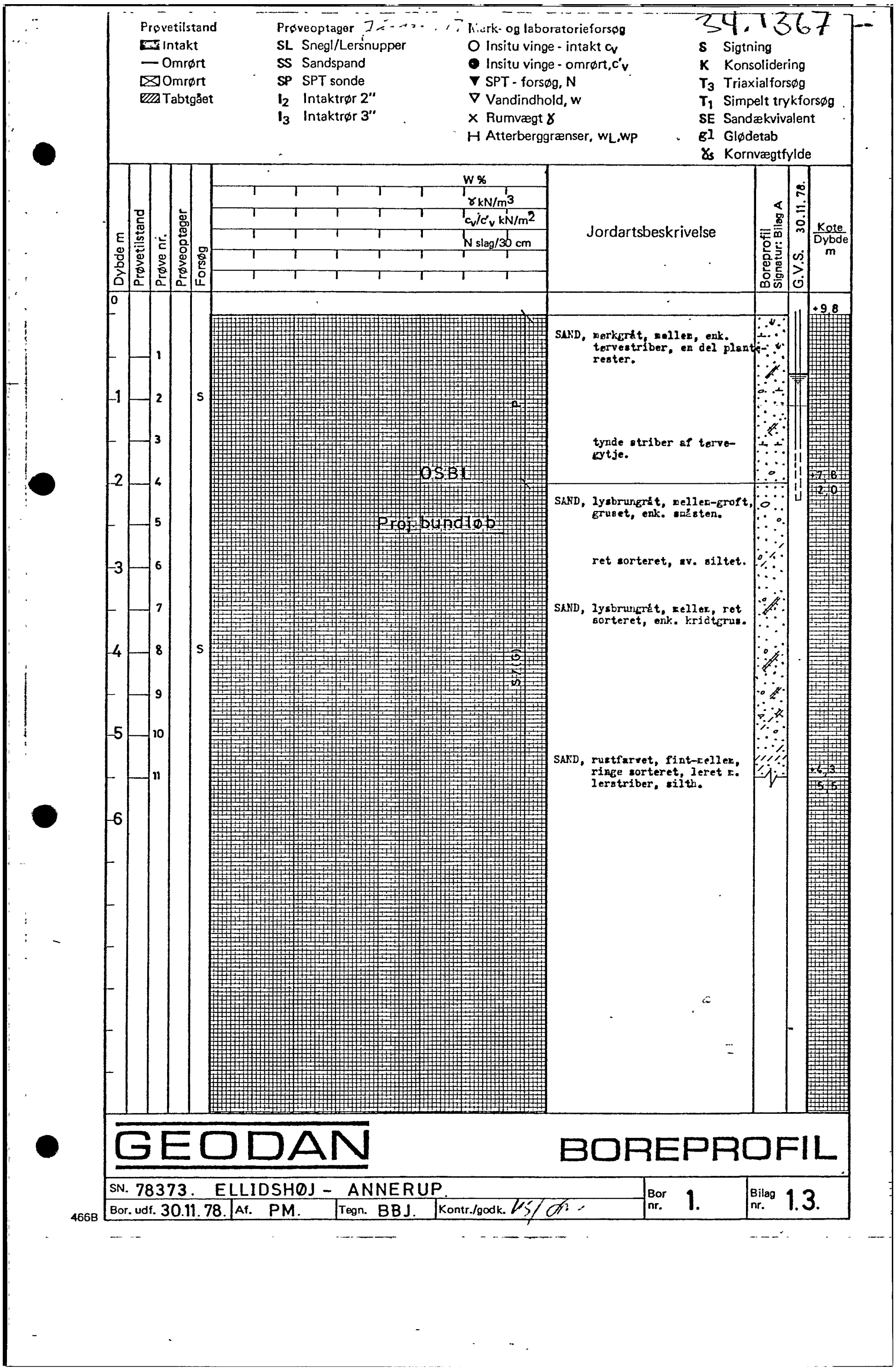

Fig. D.1: Borehole 1

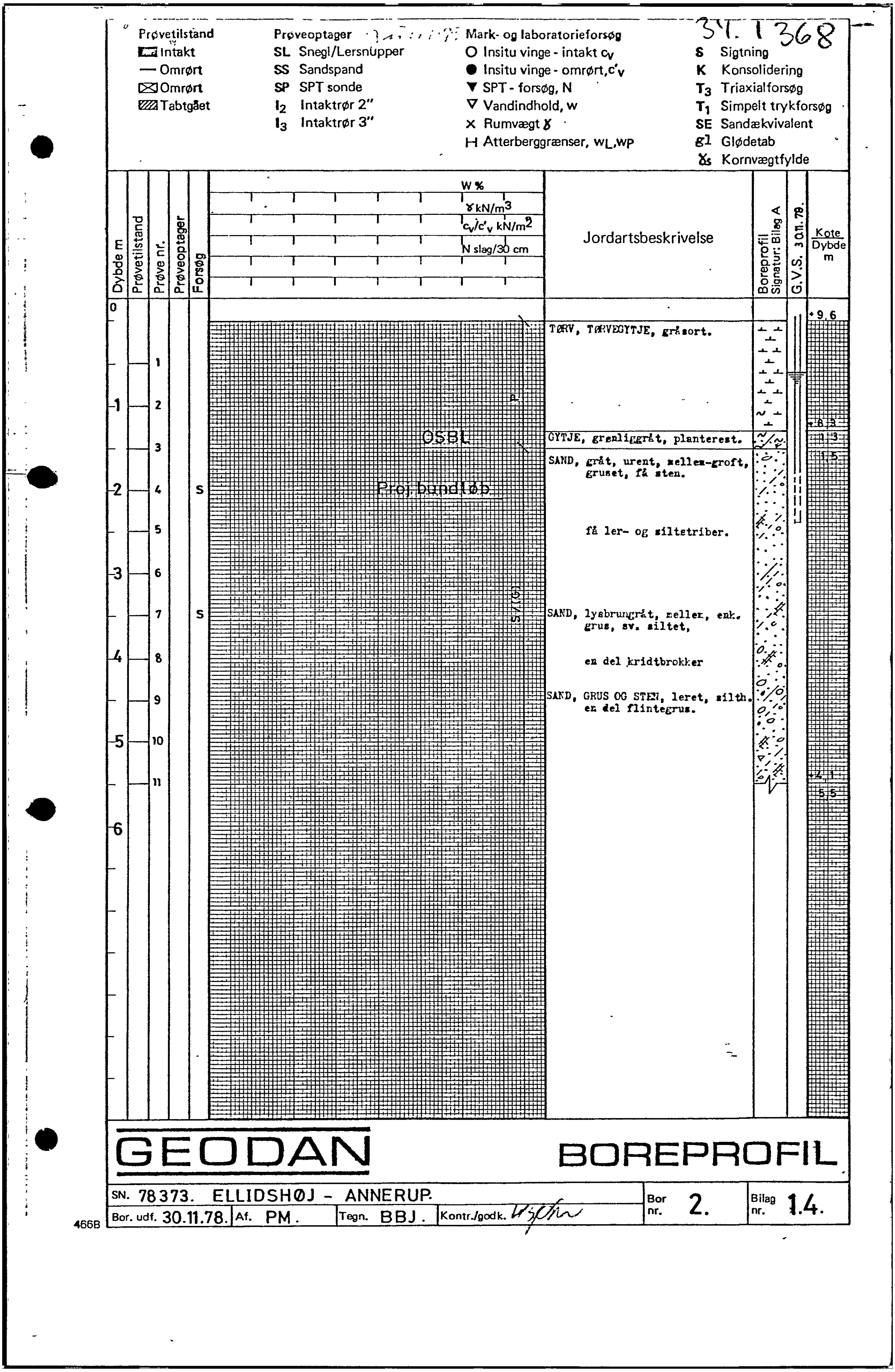

Fig. D.2: Borehole 2

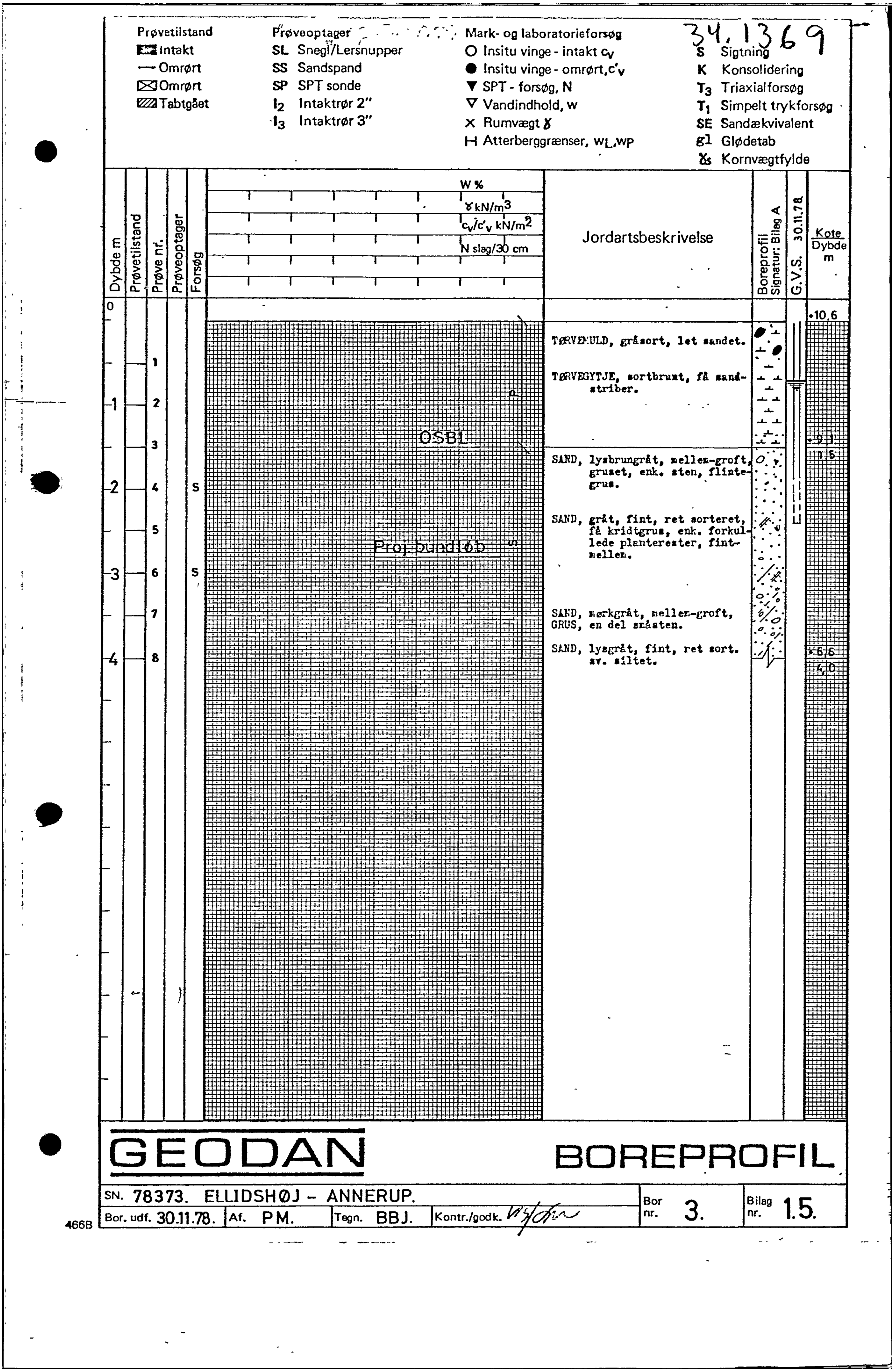
34.1369

Prøvetilstand
Intakt
— Omrørt
Omrørt
Tabtgået

Prøveoptager
SL Snegl/Lersnupper
SS Sandspand
SP SPT sonde
I_2 Intaktrør 2"
I_3 Intaktrør 3"

Mark- og laboratorieforsøg
O Insitu vinge - intakt c_v
● Insitu vinge - omrørt, c'_v
▼ SPT - forsøg, N
∇ Vandindhold, w
× Rumvægt γ
H Atterberggrænser, w_L, w_P

S Sigtning
K Konsolidering
T_3 Triaxialforsøg
T_1 Simpelt trykforsøg
SE Sandækvivalent
gl Glødetab
γ_s Kornvægtfylde

Dybde m	Prøvetilstand	Prøve nr.	Prøveoptager	Forsøg	W % / γ kN/m³ / c_v/c'_v kN/m² / N slag/30 cm	Jordartsbeskrivelse	Boreprofil Signatur: Bilag A	G.V.S. 30.11.78	Kote / Dybde m
0									+10,6
		1			OSBL	TØRVEMULD, gråsort, let sandet.			
1		2				TØRVEGYTJE, sortbrunt, få sandstriber.			
		3							+9,1 / 1,5
2		4		S		SAND, lysbrungråt, mellem-groft, gruset, enk. sten, flintegrus.			
		5			Proj. bundløb	SAND, gråt, fint, ret sorteret, få kridtgrus, enk. forkullede planterester, fintmellem.			
3		6		S					
		7				SAND, mørkgråt, mellem-groft, GRUS, en del småsten.			
4		8				SAND, lysgråt, fint, ret sort. sv. siltet.			+6,6 / 4,0

GEODAN BOREPROFIL

SN. 78373. ELLIDSHØJ – ANNERUP.				Bor nr. 3.	Bilag nr. 1.5.
Bor. udf. 30.11.78.	Af. PM.	Tegn. BBJ.	Kontr./godk.		

466B

Fig. D.3: Borehole 3

COWI Rådgivende Ingeniører AS	Borefirma: COWI	Metode: SNEGL	Sagsnavn: ELLIDSHØJVEJ 63 ELLIDSHØJ		Borings nr.: B2
Terrænkote: m.o.h. . / Pejlerør: m.o.h. . Ø . m.o.t. .	Diameter: 6"	Foringsrør: Ja: ☐ Nej: ☒	Sagsnr.: 32388	Tilsyn: SFH	Bore dato: 21 JAN 1998

Prøve nr.	Dybde	Lag-grænser	Prøvebeskrivelse: Felt: ☒ Lab: ☐	Boreprofil: Symbol	Boreprofil: Signatur	Boreprofil: Indretning	Boreprofil: GVS & Dato	PID span 2	Lugtindtryk: Neutral	Lugtindtryk: Spor	Lugtindtryk: Kraftig	Type	Kemisk analyse
P 1	0.1	0.10	FYLD, muld. FYLD, aske, sort.	O O				1	X				X
P 2	0.6							<1	X				X
	1.0								X				
	1.5					Fy/Rc			X				
	2.0								X				
	2.5								X				
	3.0	3.10							X				
	3.5		MULD.	M		Oj/Rc			X				

kote 12,5

552777, 6309642

1216 I SØ
7
X 114

24 NOV. 1998

34.2320

P:\32388\DRWG\851-1018\AEL_BOR1.DGN

Fig. D.4: Borehole 4

E | Soil Modelling

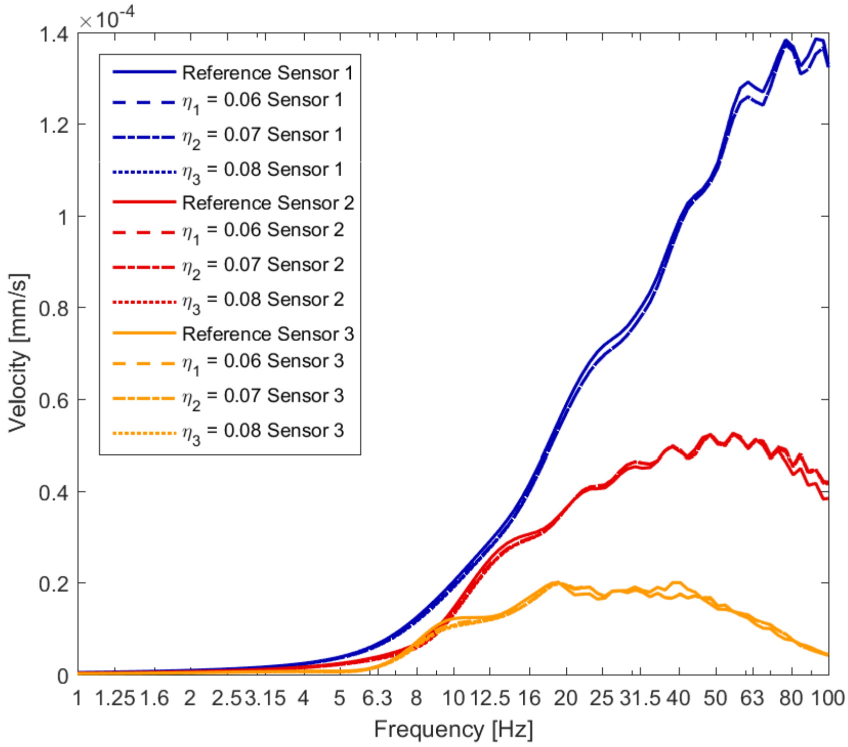

Fig. E.1: FRF for change of damping ratio for bottommost layer.